Electromagnetic Inspection Techniques for Glass Production

A thesis submitted to The University of Manchester for the degree of

Doctor of Philosophy

in the Faculty of Engineering and Physical Science

2013

Yee Mei Tan

School of Electrical and Electronic Engineering

List of Content

Word Count: 40203

List of Figures

List of Tables

Abstract

This thesis considers the feasibility of using the electromagnetic techniques to monitor the wear of the refractory base of a glass-making furnace. The research focuses in building a system that is able to provide measurements of the distance to the molten glass in this demanding high temperature application. The main challenge in this project is to eliminate the effect of the refractory supporting steel structure and still be able to detect and exploit a much smaller signal from the molten glass. In order to differentiate between the molten glass and the steel supports, a multi-coil, multi-frequency technique was proposed, studied and implemented in this research.

The electromagnetic measurement system consisted of an array containing 16 coils, which was built on a double sided PCB board with 8 transmitting and 8 receiving coils on each side of the board. The control circuitry was designed and the component circuits were built next to their respective coils. Detailed analysis of the refinement of the system to increase its portability including the housing, sensing equipments and circuitry was performed.

The thesis contains researches on the sensitivity to the influences of a variety of parameters which may affect the measurement. These included the effect of the position of the supporting steel structures, the conductivity of the glass and the electromagnetic properties of the steel response at multi-frequency. A flexible modelling algorithm which uses the layering method was proposed. Simulations and experiments were performed to verify the capability of the sensor system.

For experiments in the laboratory and test rig, the system has shown its ability in monitoring lift-off changes by matching the experiment results with the finite element modelled predictions. The instrument is able to provide measurements with average accuracy of 3.47%. This encouraging error rate has led to the hot end trial for the system. The system was able to withstand the temperature of approximately 420 $^{\circ}$C. However, as the furnace wall for the experiment was barely worn, the signal from the molten glass was too weak to be detected by the sensor. The analysis of the experiment was unsuccessful in inversing the accurate thickness of the refractory wall. Therefore, subsequent work is required in order for signals from the target at further distances to be tested on the refractory that are barely worn and have thicker walls.

Declaration

No portion of the work referred to in this dissertation has been submitted in support of an application for another degree or qualification of this University or any other institution of learning

Copyright Statement

(1) Copyright in text of this dissertation rests with the author. Copies (by any process) either in full, or of extracts, may be made only in accordance with instructions given by the author. Details may be obtained from the appropriate Graduate Office. This page must from part of any such copies made. Further copies (by any process) of copies made in accordance with such instructions may not be made without the permission (in writing) of the author.

(2) The ownership of any intellectual property rights which may be described in this dissertation is vested in the University of Manchester, subject to any prior agreement to the contrary, and may not be made available for use by third parties without the written permission of the University, which will prescribe the terms and conditions of any such agreement. Any such agreement exists with Pilkington Group Limited.

(3) Further information on the conditions under which disclosures and exploitation may take place is available from the Head of the School of Electrical and Electronic Engineering.

Abbreviation

NDT	non-destructive testing
2D	2 - dimensional
3D	3 - dimensional
CVD	chemical vapour deposition
UV	ultraviolet
FM-CW	frequency modulated continuous-wave radar
AU-E	acousto ultrasonic-echo
IR	infrared
EM	electromagnetic
NDE	non-destructive evaluation
MIT	magnetic induction tomography
FEM	finite element method
CMMR	common-mode rejection ratio
PCB	printed circuit board
FR4	flame-retardant 4
GUI	graphical user interface
DAQ	data acquisition
NI	National Instruments
rms	root mean square
LED	light-emitting diode
USB	universal serial bus
SNR	signal-to-noise ratio
AZS	alumina zirconia silica

Acknowledgement

First of all, I would like to express my highest gratitude to my supervisor, Professor Anthony Peyton for guiding me throughout my research, for showing me his academic expertise which has guided the path for me to gain the skill and knowledge required.

I would like to thank my sponsor company, Pilkington Group Limited (NSG Group) for funding this project. To Richard Denno, Doug Thow and Keith Hyland, thank you for being helpful in the experiments and providing useful information from the start to the end of the project.

To my current and previous colleagues, Wuliang Yin, Christos Ktistis, Liam Marsh, Xin Li, Grzegorz Zysko, Wenqian Zhu, Sriram Dorai, thank you for helping me in all aspects, from providing helpful technical tips to being my company when I am working till late in the lab.

And to the most important people in my life,

Pa & Ma,

Thanks for always having trust and faith in me. Thanks for being there for me all the time to listen to me, showing care and giving me warmth even though we are 6000 miles away.

Jie ,

Thanks for showing your silliness and crack random not-so-funny jokes all the time. It does cheer me up at times thinking of how not funny it is.

Kor,

Thanks for convincing Ma to let me to study abroad at the very first place.

Thank you for being supportive all along. I love and miss all of you so much!

Chapter 1 Introduction

1.1   Motivation

This research will apply the methodology of electromagnetic inspection for non-destructive testing (NDT) by aiming to explore, develop and improve the current technology and existing equipment to monitor the on-line float furnace for glass production. It is a follow up research work of the contribution of [1].

During the process of glass making and particularly the conversion of raw material into the molten glass, the high temperature molten glass is prone to be corrosive towards the furnace walls and floor. Hence, it would be beneficial if there is a method with the ability to measure the furnace thickness directly. Clearly the glass manufacturers desire to stretch the operational life of the furnace as long as possible, at the same time, preventing the risk of having a break out of molten glass from the base of the furnace. A break-out of molten glass from the furnace bottom may put the life of the operating staff in danger. Typically the furnace operational life is approximately 15 to 20 years. When it is near the end of the lifespan of the furnace, the furnace often requires more monitoring and fixing.

The high demand in high transparency clear glass has also induced the quicker wear of the furnace. The temperature is sometimes higher than the usual furnace which produces the standard clear glass, by approximately 100 ^{o}C. As a result, the increase in temperature would lead to quicker furnace wear. Depending on the situation of the wear, a partial or total rebuild of the furnace may then be carried out. This has brought many glass-making companies to consider using NDT methods to monitor the internal condition of the furnace and lead to more research on current and new NDT technologies for this application.

The examples of the current monitoring methods include using the infrared thermography, radioactive tracers, microwave and etc. Compared to these techniques, the electromagnetic inspection method has several advantages. It is non intrusive, able to provide quick response, and it is also generally low in production cost.

1.2   Aims

The primary target of the project is to develop an instrument that is able to produce a non-destructive measurement for the furnace base thickness. The instrument has to be able to measure the low conductivity target. This would be able to help in monitoring the molten glass in the furnace.

There are currently no established methods that operate with multi-frequency electromagnetic technique for monitoring the glass refractory. On the development of the electromagnetic system, the aim was to create a system that is immune to the steel structures of the furnace. The multi-frequency sensing system is immune to the steel effect at higher frequencies and any changes to the signal will be the contribution of the molten glass. The multi-frequency operation also allows obtaining more spatial data for inversion.

By measuring the base of the furnace, the instrument will have to be able to withstand the high temperature and still be able to provide reliable results. The external wall of the furnace base is approximately 400 to 500 ^{o}C. A previous project has developed a bird table-like experimental system, which has shown a convincing result for its measurement. However, the system is cumbersome and difficult to use. Therefore, further research work is carried out for developing a more portable sensing system.

As the system will be used in a demanding high-temperature environment, the electronics components have to be carefully chosen. The sensing system is intended to take measurements quickly; hence, it is designed to operate for the receiving channels to conduct measurement at the same time, avoiding the need of a scanning mechanism for the receiving channels.

1.3   Organisation of Thesis

This thesis consists of 8 chapters. The organisation of the thesis is discussed as follows.

Chapter 2 provides the literature reviews into glass manufacture and an introduction to the furnace structures. Then, the float glass-making process is also presented. The relationship between the temperatures with the conductivity is shown, this relationship is important for the reference in obtaining the conductivity of the glass for the simulations. The current technique used commercially to measure the melt and the refractory is described.

Chapter 3 is a background introduction for the NDT technique of this current project, which is an electromagnetic inspection technique. The current technique has been widely used in low conductivity inspections and examples are shown. Hence, this has led to the interest for this technique to be applied to this project. The basics of the electromagnetic principles are described. Different analytical methods are discussed as well as the limitation of the analytical methods which lead to the use of the numerical technique that is introduced in the following chapter.

Chapter 4 presents the modelling techniques by using the finite element method (FEM) in 2-dimensional (2D) and 3-dimensional (3D) modelling software. At the beginning of the work, 2D and 3D electromagnetic models were constructed in order to analyse the accuracy of measurement in the layering method in the model. The region around the molten glass/ refractory lining interface was represented in layers. This allowed the lining thickness to be changed in the simulation by just assigning the material to be vacuum or glass without having to create a different model each time. The influence of the steel structure which supports the furnace is a very crucial problem within this research; therefore, different positions of the steel sections were carried out in the simulation. This research helped to determine the effect on the measured signals of either the steel geometries measurement error or the different steel geometries for different furnace structures. The models have also considered the steel with an impedance boundary in the simulation instead of assuming the steel to be a perfect electrical conductor in order to give more practical simulations.

Chapter 5 discusses the data acquisition system. When choosing the electronics components, the ability of the components to withstand temperature changes is important. This chapter starts with the introduction of the sensing system with sensor, coils, shielding. Then it proceeds to the individual electronics test for the amplifiers, reference pick up coil, and resistors. Several problems and modifications are pointed out on the electronics sensor. A more compact acquisition unit was constructed. The chapter leads to the discussion on the improvement of the sensing hardware and equipments, which included the modification and replacement of the hardware unit to reduce the weight of the overall system.

To control the data acquisition system, a program in LabVIEW was designed and shown in Chapter 6. This chapter introduces the software design and measurement strategies, which eases the understanding of the function of the program for its general controls and outputs functions.

Chapter 7 considers the hardware experiments. The hardware was tested in three different locations – on a laboratory tank at the University, on a model test rig and on the furnace itself. Several sensitivity tests including the effect of steel, the conductivities stability of the system, the lift-off and spatial responses, the frequency response of the system and the effectiveness of applying current technique on the grillage installed furnace were analysed. The successful cold temperature measurement has led to the system being tested in hot end testing, which was discussed later in this chapter.

The overall conclusion for the work in this thesis is discussed in Chapter 8. The future work was discussed to improve the current system in this project.

1.4   Publication

Y.M Tan, W. Yin, and A.J. Peyton. *Non-contact measurement of water surface level from phase values of inductive measurements*. in *Instrumentation and Measurement Technology Conference (I2MTC), 2012 IEEE International*. 2012.

Chapter 2 Background

2.1   Glass

Glass is a hard, brittle and transparent material that is widely used in automobile, residential and commercial settings, for instance, doors, shower screens, furniture, wall panelling, windscreens and many other applications. In the progress of glass making, quality control is a crucial issue. Manufacturers are constantly searching for methods to produce high quality glasses and one of the main challenges to achieve this aim is to exclude defects caused by the presence of bubbles, un-melted 'stones' and defects in the glass that can lead to degradation of the finished glass products [2, 3] .

The production of some specialty and industrial glass with higher levels of transparency and clarity has exposed the refractory lining to harsher furnace condition than previous encountered such as higher temperature in the float line process, which has resulted in higher corrosive properties of the melt and hence increased erosion of the furnace refractory lining. The rate of regression of the refractory lining depends on several factors including; the lining material, the raw material for melting, the stirring method, the temperature, influence of various convection flows in the glass melt, the attack of alkali vapour and several unknown reasons has causes the corrosion of the refractory lining [4-8]. This corrosive action of the furnace has also adversely affected the glass quality as some of the materials that break away from the furnace form small stones in the glass and introduces contaminant to the glass which would then degrade the glass.

Thus, it has drawn the concern of the glass manufacturers to monitor the thickness of the refractory lining as it is a key issue for the operational life of the furnace, which directly affects the cost of investments and the safety of the working environment. It is desirable to have the inspections while the furnace is in operation in order to avoid losses associated with furnace downtime, such as production loss, disruption of supply time taken to remove the glasses in the furnace, and the waste of manpower. With the hostile environment in the furnace, it is important to have instruments to determine the condition of the refractory materials in glass furnaces without the need to access the interior. This would enable the

manufacturers to monitor the furnace condition and only carry out the repair when it is necessary. This would help in extending the operating lifespan of the furnace without risking the safety of the nearby employees.

2.2   Glass Furnace Structure

A glass furnace is a chemical reactor where the raw materials are fed into the chamber and where the change of physical state reactions take place at high temperature, typically 1100-1500 ^{0}C, converted into glass. In the glass process line, the melt depth varies from 0.5 m to 5 m in the float line. The variation depends on the type of glass, type of production furnace and glass colour to be produced.

The glass furnace is often a stationary tank, consisting of a crown, the vessel walls for the side and the bottom, the steel structures for bottom support, charging and discharging doors. However, sometimes a rotating furnace can be found to increase the ability to distribute heat, to reduce forming of bubbles in the glass, reduce overheating for the furnace or to produce unique lenses and primary lens of optical telescopes [9-11]. This thesis largely concerns the stationary float furnace which is focused in flat glass production.

Furnaces are heated using a variety of fuels. Flames of flue gases from the fuel directly contact the molten glass surface, so the type of the fuel chosen is important. Solid phase fuels may disturb the molten glass; therefore, most of the furnaces use liquid fuel, gaseous fuel or sometimes electricity for energy supply. Figure 1 shows the typical design of a float glass furnace with side fired walls.
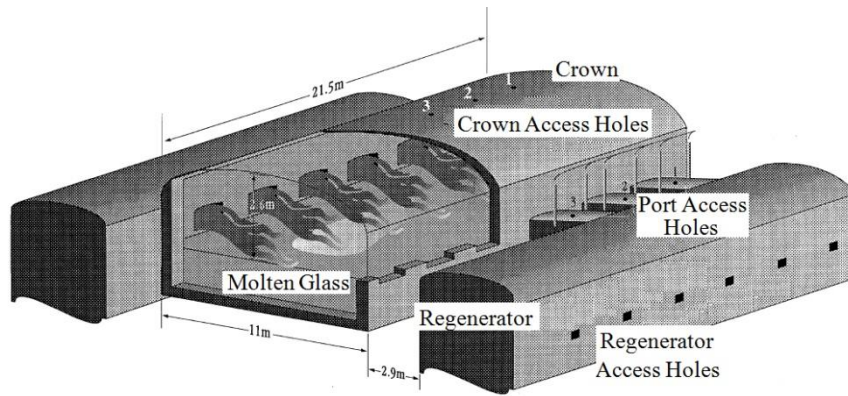
Figure 1 Schematic of float glass furnace [12]

The melter is the initial place where the batch of raw material is melted and refined and along each side of the melter, several ports are located above the glass melt level that contains the fuel and combustion air. These ports fired alternately in approximately 20-30 minutes intervals to ensure more even heating of the melt. When the fire takes place at one side, the exhaust gases exit through the adjacent row of ports in the melter and pass through heat regenerators. Normally, these gasses will be used in the regenerator to preheat the combustion air [13]. However, these exhaust gasses are sometimes used to generate steam for process use or space heating, electricity generation, or to preheat raw materials before feeding into the melter [14, 15].

Figure 2 An empty new float glass furnace with ports at side walls

Figure 2 is a new float glass furnace that shows the melting area. The distance from the floor to the springing line of the crown is approximately 2.4 m and the width is approximately 2.5 m. As 80-85% of the fossil fuel heat are transmitted on the upper region of the batch, electrodes that are arranged at the furnace bottom creates the ability of producing internal and supplementary heat source in the melt [16], consequently enhancing melt circulation. With the electrode booster, the burden of the combustion of the side walls can be lowered, which also reduces erosion to the refractory blocks at the side. The additional heat flux helps improve the quality and the quantity of the production [17]. As electric heating is twice as efficient as the flame heating, it is very attractive to manufacturers, however, the energy required for constant usage costs more than fuel for the flame heating system. Apart from that, cautious usage of this extra heating system is required as overheating the furnace would reduce the operating lifespan of the process.

A furnace must be built with materials that are able to withstand high temperature and Figure 3 demonstrates one of the supporting structures of the furnace, which contains transverse U and I section steel beams.
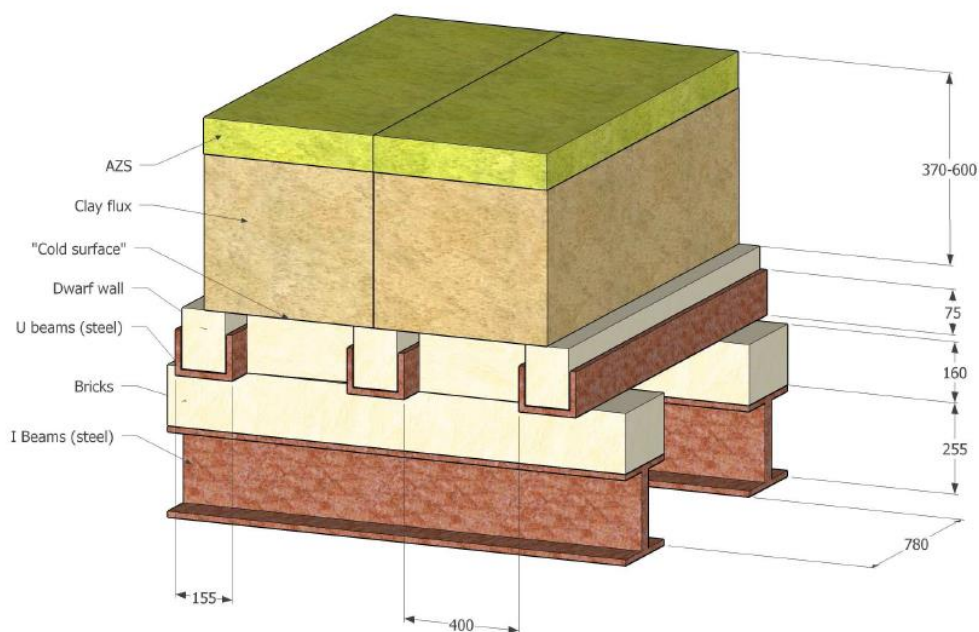
Figure 3 Geometry of the furnace dimensions in mm [1]

Figure 4 follows from the previous geometry and illustrates the materials and the typical thicknesses that are used in for the furnace bottom.
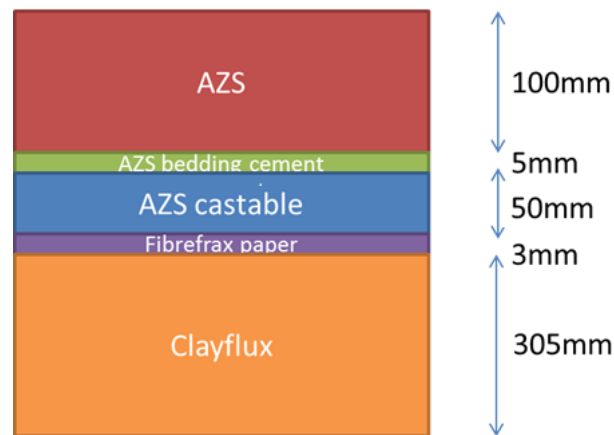
Figure 4 Dimensions of furnace floor thickness
(Information courtesy of NSG European Technical Centre)
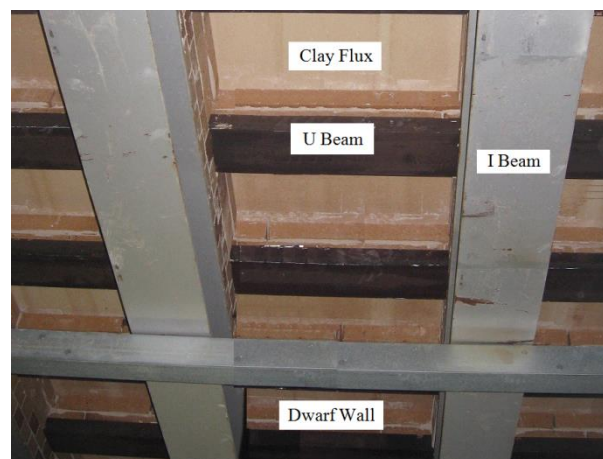
Figure 5 Supporting steel structures of furnace at the bottom of furnace

The furnace is supported on steel 'U' and 'I' beams as shown in Figure 5. The furnace design and dimensions varies greatly from one furnace to the other. At times, some older furnaces have been designed with an additional steel grill mesh support that fully covers the bottom of the furnace and consequently restricts access to the underside of the clay flux bricks.

2.3   Float Process

The term "float" derived from the production method that was invented by Sir Alastair Pilkington in 1950's and later was patented on November 1959. This is the method that is currently most use in the glass industry for producing flat glass.

The float glass manufacturing process is carried out in six integrated stages in a float line that is approximately half a kilometre long. Figure 6 shows the basic float line process, consisting of six main production stages. The furnace may operate non-stop over 15 to 20 years. The typical thickness of glass produced is between 0.4 mm to 25 mm and the width of the glass is around 3 m.
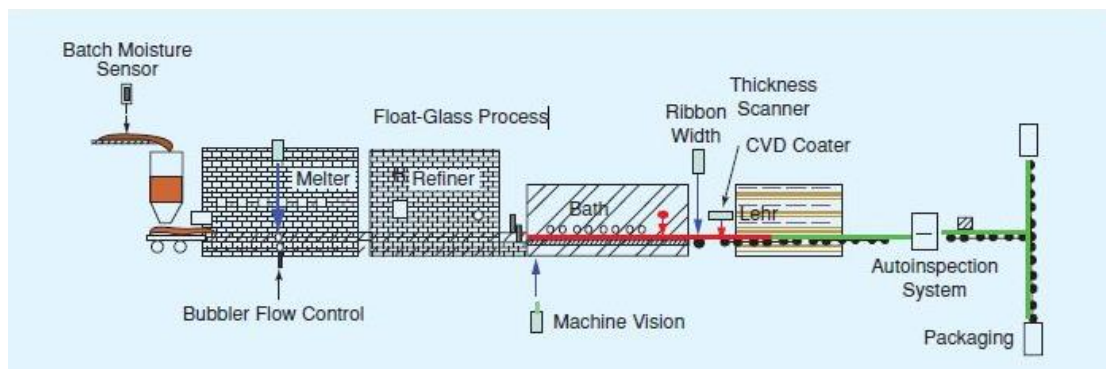
Figure 6 Process diagram for the float-glass process [18]

2.3.1   Melting and Refining

Raw materials such as sand, soda ash, limestone, dolomite, alumina and others are mixed to make a batch. This batch of ingredients is fed into the melter as a blanket on to molten glass that is with approximately 1500 ^{o}C. To eliminate any bubbles and produce a smooth and continuous melt to the float bath, the melting process takes up to 50 hours and is heated approximately 1100 ^{o}C. The initial melting and refining process is crucial as it determines the quality of the final product.

2.3.2 Tin Bath

The molten glass flows gently in a freefall motion on to the molten tin bath. The tin bath, which is typically between 25 mm to 300 mm in depth and about 20 m long, is used as a platform for the formation of perfectly smooth and even thickness surface for the flat glass. Then, the glass will be left to cool from 1100 $^{\circ}$C to 600 $^{\circ}$C. This temperature is where the glass' viscosity is high enough (10 GNsm^{-2}) for the ribbon to be removed from the float bath mechanically without leaving marks on the surface or damage [19, 20].

2.3.3 Coating

The glass is coated at the area between the tin bath and the annealing lehr in the float line [21]. With the technology of on-line chemical vapour deposition (CVD), the optical properties of the cooling ribbon of glass can be changed. This process is where reactive precursors are vaporised into a gas stream carrier, which is directed to the cooling surface of the glass, which is approximately 600 $^{\circ}$C, forming a thin layer film on the glass. Usually the coating is less than a micron thick. There are several common coating materials in use as such as silicon, titanium, nitride and the oxides of silicon, aluminium, tin, zinc and transition metals. This process has enhanced the functions of the glass by introducing antiglare, anti-reflexion or anti-static layers, changing the dielectric or transmission properties, strengthening the glass substrate, improve temperature resistance and also protecting the glass from moisture [22-25].

2.3.4 Annealing Lehr

After the glass exits the float area, the glass is cooled at the lehr. There are considerable high stresses built up in the ribbon during the formation of glass in the float. The annealing process helps the ribbon to relieve the stresses. During this process, the temperature profile across the glass is critical. It is possible to cut the glass when the glass is cooled properly in the lehr. Appropriate annealing also avoids residual stresses which can made glasses fragile and also avoid the breakage beneath the cutter.

2.3.5   Inspection

Flaws can be caused by any contamination of the batch mixture, incomplete melt of raw materials, and the existence of bubbles during the refining process and ripples in the tin bath due to vibration. These defects are unavoidable and will depress the glass grade dramatically [26]. Technologies based on reflections such as laser systems and cameras are useful in float glass inspection to inspect the glass contamination and topographical defects [27, 28]. Inspections are carried out as fast as 100 million measurements per second across the ribbon. Often the inspection cameras are prefixed at the top and bottom of the inspection rollers. Contamination in glass will stop light from the source passing through the glass to the vision system. For the glass surface defects, light will be refracted at a different angle away from the receiver. By having inspection in glass-making process enables the computer to guide the cutter around the defects to reduce wastage and also improving the quality of product to customers.

2.3.6   Cutting

The float glass is sold in cut sizes. In the manufacturing plant, cutting the glass is the final process before the product is sold to the customers. It is a process to cut off the ribbon to the size required and to trim off any defect marks at both side edges caused by the traction rollers. Optimum cutting parameters are monitored closely during this stage to prevent the cutting edge having chips and pits and also reducing the strength of the glass.

2.4   Clear Float Glass and Low Iron Glass

Conventional clear float glass contains a certain degree of inherent green cast. The green tint becomes more visible as it is thickened or when multiple sheets are stacked together, especially at the glass edges. This is due to the existence of iron in the glass, which is one of the raw materials used in glass manufacture to aid the melting process. As trends in architecture and design have moved to greater transparency, this in turn has increased the demand for better optical clarity in glass. The benefit of photovoltaic modules in its ability in generating consistent power at low cost has also contributed to the demand in the low iron glass.

Low-iron glass, sometimes known as extra-clear glass is a new improved specialty glass that is able to provide a higher degree of light transmittance than the clear float glass. As the glass is near colourless and the percentage of light that passes through the low iron glass is greater, it is ideal for the usage where the edges of the pane are visible or where the perfect visual effect of natural colour is desired.

Glass Thickness	Light Transmittance (%)	
	Clear Float Glass	Low Iron Glass
2 mm	90	92
3 mm	90	92
4 mm	89	92
5 mm	89	91
6 mm	88	91
8 mm	88	91
10 mm	87	91
12 mm	85	91
15 mm	84	90
19 mm	82	90

Table 1 Performance comparison for clear float glass and low iron glass
(Information courtesy of Pilkington Optifloat and Optiwhite datasheet.)

Table 1 lists the light transmission rate of the clear float glass and low iron glass, the higher the percentage, the more daylight will be able to pass through the glass. As the difference in light transmission level becomes bigger as the glass becomes thicker, hence, the clarity is higher for the low iron glass after comparing with the clear float glass with similar thickness.

Raw Material	SiO$_2$ Silica	Na$_2$O Soda	CaO Calcium Oxide	MgO Magnesium Oxide	Al$_2$O$_3$ Alumina	K$_2$O Potassium Oxide	SO$_3$	Fe$_2$O$_3$ Iron Oxide
Mixture Proportions	72.6%	13.9%	8.4%	3.9%	1.1%	0.6%	0.2%	0.11%

Table 2 Chemical Analysis of Typical Clear Float Glass
(Information courtesy of NSG-Group Technical Information ATS-129)

For achieving this optimum clarity in glass, the iron content is reduced to 0.01-0.03% [29]. As iron oxide is an absorber of infrared energy in glass; the iron oxide significantly reduces the absorption of visible and solar radiant energy in the melt [30]. There are methods in increasing the absorption of UV such as by adding UV absorbing additives, e.g. CeO$_2$ and TiO$_2$. However, the additives are expensive and also adversely affect the visible transmittance of the glass. Therefore, a balance of a suitable modification on raw materials to maintain appropriate degree of increase of glass melt temperature is required.

As the temperature of the low-iron glass at the furnace bottom is higher, furnace erosion will be accelerated more than for clear float glass production in a float line that uses a conventional composition. As a result, this will caused a much shorter operating lifespan of the furnace.

2.5   Flow and Heat Transfer

The study of heat transfer is fundamental to the understandings of glass production. By proper heat distribution in the furnace, the melt flow can be controlled. This is important as it helps to ensure that the glass melting process is carried out in the correct sequence, provide modelling information for environmental emissions, make certain that the right amount of fuel is used to prevent wastage and overheating the batch or affect the production time and glass quality by providing too little heat [31-33]. By understanding the glass temperature and flow profiles, information on the dead space volume (the zone where the melt residence time is long) can be obtained. An incorrect temperature distribution is one of the causes of asymmetrical flow patterns and the attendant problems described in this paragraph.
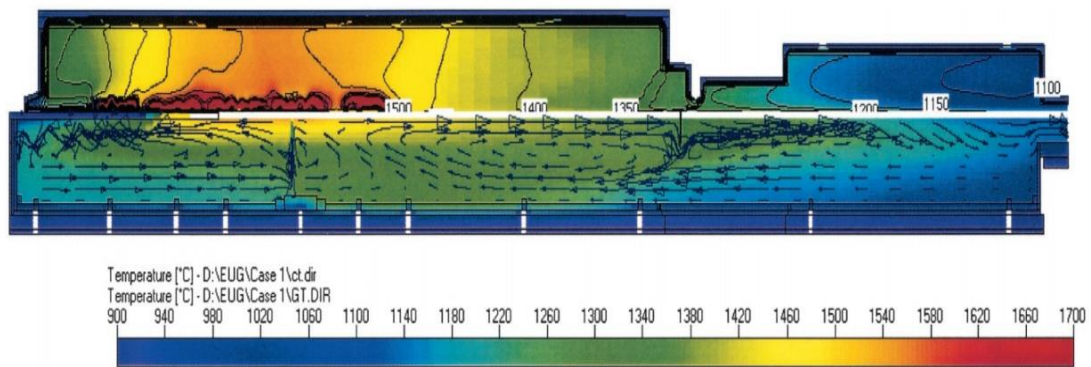
Figure 7 A typical temperature distribution in vertical longitudinal cut for the melting batch [34]

Figure 7 shows the temperature profile throughout the melt, with the highest temperature up to approximately 1500 ^{0}C. As the glass in the furnace is in a molten state, ion mobility in the melt allows the electrical current to be transported; therefore the molten glass is electrically conductive. Furthermore, the electrical conductivity of glass melt is a function of temperature as shown in Figure 8.
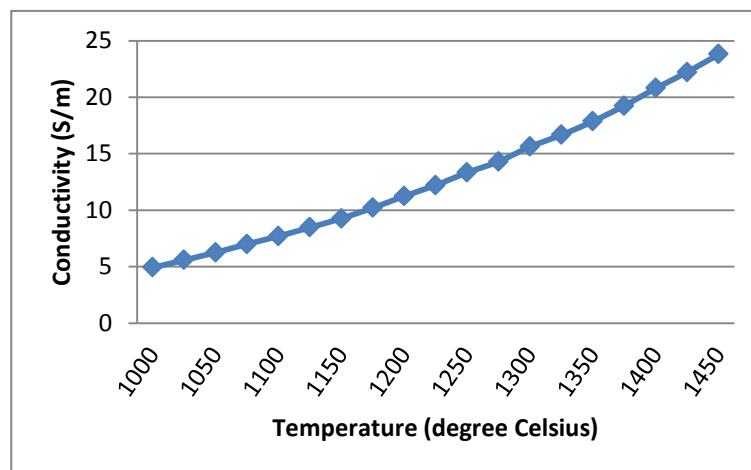
Figure 8 Conductivity of glass melt with the heating temperature in furnace
(Information courtesy of NSG European Technical Centre)

The study of the heat flow in the furnace is crucial to provide a better understanding of the lining profile of the furnace. The wear of the furnace wall is not uniform throughout the furnace and it is usually more prominent in these areas

    i.   The floor lining that is constantly in contact with the melt.

   ii.   The hearth lining above the dwarf walls. As the dwarf walls act as an insulator for the heat flux from the bottom of the furnace, temperature is higher in this area.

  iii.   The region near the electrical heating electrodes, which are used for boosting the temperature in the melt, inducing a high temperature region around it.

  iv.   The side walls where the boundary between the melt and the air is. The temperature step between the two phases is huge, causing higher corrosion and penetration through the side walls for the area covered by the melt.

Break-out of molten glass from a furnace can occur and can have severe consequences to the safety of the plant operators and of course the financial loss to the glass production company. Figure 9 shows a photograph emphasising the consequences of failure of the furnace lining. In this case, the operators only just managed to avoid a more serious disaster by spraying cooling water on the escaping molten glass causing it to cool and solidify.

Figure 9 Glass leakage (Photo courtesy of NSG European Technical Centre)

2.6   Techniques Employed for Inspection of the Furnace Lining

As discussed previously, temperature plays an important role in all stages in the glass production, from the melting to the annealing stage. Temperature values are often determined by the numerical simulation or with the conventional method of taking physical measurements from the process.

2.6.1   Monitoring the Melt Flow and Temperature

2.6.1.1 Thermocouples

One of the general ways of determining the temperature in the furnace includes mounting probes, primarily thermocouples in the furnace lining. It is required to have a prefixed thermocouple installed during the construction of the furnace lining or it will require holes to be drilled through the refractory, which can have the unwanted effect of speeding up the wear of the furnace at the drilled area. Since the glass furnace is an extremely large vessel, it is often takes 10 or more hours for the furnace to change significantly in temperature with a large spatial distribution. Consequently a small number of thermocouples can only give a rough estimation of the temperature [35]. In addition, a thermocouple is not able to operate for a very long period (e.g. > 10 years) at very high temperatures and will require frequent maintenance and recalibration. In [36], the thermocouple was protected with a layer of Allundum cement on the surface. This step has reduced the sensitivity of the sensor as the sensitivity is inversely proportional with the thickness covered. An additional problem caused by the thermocouple is the interference introduced to the glass quality as it may cause cords in the glass and the melted thermocouple may contaminate the production. Hence, there is a compromise between the cost and speed of response for the frequency of services and the sensitivity of the measurements.

2.6.1.2 Radio-Isotopes

The use of radio-isotopes to observe the flow of melt within a furnace has been used in the 1970's and 80's [37, 38]. This technique enables the time duration of the melt within the

furnace to be calculated by measuring the intensity of radiation emitted. However, this method has some disadvantages as the radioactive isotope may disturb the mixing action within the furnace which may affect the quality of glass, for example, the isotope may form lumps if improper mixing occurs. Before the raw materials are fed into the melter, the batch was assumed to have a uniform mixture. Improper mixing of raw materials with the isotope will introduce error to the results as the radioactive results are determined by the chemical analysis of the radioactive tracer and the concentration of radiation at different location in the production line.

2.6.1.3 Infrared Thermometry

Thermal radiation thermometry is a non intrusive method compared to the previous two sensing methods. This method utilises the radiant emission through the surface of the glass to study the surface temperature. It can be used to evaluate the thermal gradient in different depth of the glass melt [39], by solving an inverse heat flow problem, but often with large errors because of incomplete data and assumptions in the underlying thermal model. The readings obtained with this approach are often affected as the energy received by the sensor is not only from the surface, but possibly from the interior of the glass and attenuated from the surrounding combustion. In [12], two instruments were proposed to measure the heat flux for the crown. These instruments were required to be placed at the crown access holes, which can be dangerous to the operators due to the high temperatures and the risk of collapse of the crown.

2.6.1.4 Direct Flow Measurement

Another intrusive method was introduced by [40] by inserting a pendulum through the crown of the furnace, with the mass of the pendulum in contact with the surface of the molten glass and dragged along by the flow. This method only allows the observation of the flow at a particular point by measuring the angle of the pendulum. It does not provide multi location data on the flow or more pendulums have to be inserted which will have more disturbances on the melt. Moreover, this technique only can only observe the x-y directions of the melt flow and not the flow in the z direction.

2.6.1.5 Fluorescence Emission Detection

The production of glass often includes Fe_2O_3. The detection of fluorescence emission from Fe_2O_3 provides a non-contacting method, which is able to provide measurement in real time. The emission of the fluorescence depends on the temperature. Workers in [41] have proposed a method for measuring the fluorescence lifetime in order to calculate the spatial temperature data. The technique produced has mainly been used for automotive glass production and it does not provide accurate temperature as it is difficult to obtain the final lifetime measurement. The application of using better laser sources was suggested to improve the technique, but this signifies a much higher cost needed for the instrumentation.

2.6.1.6 Lorentz Force Velocimetry

As discussed in Section 2.5, glass melt has low conductivity when it is in molten state. The Lorentz Force Velocimetry (LFV) technique is a non-contacting method which based on measuring the drag force on magnetic system when it is exposed to the flow of an electrically conducting molten glass. A pendulum and a rotary flowmeter were presented in [42, 43] and the equipment was placed near a conducting melt or laboratory fluid. The method uses the deflection angle of the pendulum and the angular velocity of the rotary flowmeter to determine the flow rate of the melt. There are many complications in this method which affects its sensitivity. The rod that acts as pendulum in [42] is difficult to stay in shape without bending while moving through the magnetic field. There are fluctuations in temperature in the melt which results in the change in conductivity. The stray magnetic fields around the experiment environment contribute to the error of the measurement too. Apart from these, this technique only allows a single region's melt velocity, assuming that melt at all depth moves with the same velocity.

2.6.2   Monitoring the Refractory Wall Thickness

Several methods and instruments have been used to evaluate the corrosion rate of the furnace over the past decades. Monitoring the furnace lining profiles is crucial in ensuring the operating lifespan of the furnace as well as the safety of surrounding workers.

2.6.2.1 Radioactive Tracers

As discussed in the previous section, radioactive tracing is a method of using radioactive tracers was investigated by [44, 45]. This method counts the radiation that passes through the refractory and the higher the radiation count rate, the thinner the refractory is. This method is of limited applicability as the refractory has to have the pre-constructed equipment which increases the investment in each individual furnace; the radioactive material may be highly toxic such as beryllium which may cause health hazards to the operating staff.

2.6.2.2 Infrared (IR) Thermography

Often when a structure is dense and well-bonded, the heat flow in the structure will be continuous. Applications of infrared (IR) thermography monitor the heat transfer rate according to the geometry and thermal properties in the material to obtain the refractory lining operating condition. A thermal imaging camera indicates the temperature of the object on a colour scale; the darker the colour is, the colder the area and vice-versa. The temperatures recorded on the image depend on the surface emissivity. The measurements of temperature will be inaccurate if the furnace has metals for its building structure support as the oxidation of these metals can affect the surface emissivity and hence the measurements [46]. Besides that, cracks and disbonds can only be observed if the changes of the interface thermal resistance is obvious and detectable. Spurious thermal reflection from neighbouring objects is another problem [47]. Although many solutions have been suggested such as shielding and temporary shutdown of nearby heat sources, these may not be practical as it is not cost effective to halt production. Consequently infrared thermography can only provide rough estimations and the thermal image has to be monitored over a period in order to calibrate the sequence of thermal images. Despite these limitations, the method is widely used.

2.6.2.3 Microwave

Frequency Modulated Continuous-Wave Radar (FM-CW) method uses a 'time of flight' approach which uses a triangular waveform to modulate the frequency of an oscillator. The signal is transmitted through the refractory and gets reflected back from the glass. The

reflected signal is a time delayed version of the transmitted signal and can be mixed with the transmitted signal to produce a beat signal [4]. Then the signal is analysed by a spectrum analyzer. This approach is difficult to predict the accuracy as some of the bricks contain dark glass that once melted under high temperature that may attenuate the microwave signal significantly.

2.6.2.4 Acousto Ultrasonic-Echo (AU-E)

The technique of Acousto Ultrasonic-Echo (AU-E) is a patented technology and developed in the 1990's for refractory thickness inspection. It uses the propagation of stress waves of acoustic and ultrasonic energy and determines the reflections or echoes from the changes of interface such as solid/fluid or solid/gas [48, 49]. This methodology needs a consistent material property of the furnace lining in order to analyse the reflection time based on surface displacements. Also, the elastic properties of the refractory vary with the change of temperature, the calculations of the wave velocity scaling factor will be complicated if the elasticity is not directly proportional to the change of temperature.

2.7   Conclusion

With the review of challenges in glass production and the techniques used for monitoring the glass furnace, temperature influences on sensing and data measurements is one of the key issues that this research work will address.

The technique that will be implied is a non-invasive, non-intrusive technique. It requires a realistic usage in monitoring the interior wall of refractory without having to break the glass production operation. To achieve the requirement of the above, an electromagnetic inspection method is proposed to be used for the sensor. This method benefits from its flexibility, feasible, efficiency as well as low in cost.

Chapter 3 Electromagnetic Inspection Techniques

3.1   Introduction

Electromagnetic (EM) inspection, which is also referred as eddy current inspection, is a method of non-destructive evaluation (NDE) that may be used for detecting the electrical and magnetic characteristics of a conductive object. A typical EM inspection system has one or an array of coils to transmit and receive signals through an air gap to the object.

The simplicity and versatility of deployment and the nature of non-direct contact with the target object has made this technique widely used in areas where conductive parts have to be routinely tested in industrial process monitoring. One of the key uses of electrical magnetic inspection is to find defects and to make measurements. For deflects such as cracks, the circulation of eddy currents induced in a conductor by an alternating magnetic field, are affected by the crack, which presents an obstacle to the current path. The eddy currents must flow around the insulating defect, causing a change in the magnetic field generated by the eddy currents, allowing the defect to be detected and analysed. Typically, the defects should be surface breaking as the induced eddy currents principally flow near the surface of the object facing the transmitter coil. The technique is employed, for example, to detect relatively fine and small cracks and discontinuities on materials, for example in the multi-layered aluminium structure for aircraft. The detection and characterisation of hidden cracks around fastener sites and joints in multi-layered structures is a major challenge in the aviation industry, hence, there is a significant amount of research focusing on using eddy current to detect such cracks and flaws [50-52]. With sinusoidal modulated electromagnetic field generated by an eddy current coil, it is able to provide measurements by penetrating a material over a finite skin depth, which is controllable by selecting the frequencies of operation. Therefore, multi-frequency operation, for example by pulsed eddy current testing, was developed to investigate the characteristic of substrate material properties of multilayer structures [53].

The electromagnetic inspection technique is also used in large structures such as nuclear power plant which requires consistent monitoring of pipelines. The stream of coolant flowing

inside the pipe has a thinning effect towards the pipe walls. The external of the pipes are often protected and covered with thick layers of thermal insulator to prevent thermal loss [54]. With an electromagnetic inspection technique, it is possible to detect and evaluate the wall thinning and defects of pipes without removing the external insulation. The same principle is also applicable for sheet stock to measure the thickness of material and for control of metallic coating thickness during or before the coating operation [55-58].

As eddy currents are affected by the passive electrical properties of the object material, i.e. the electrical conductivity and magnetic permeability, electromagnetic inspection method can evaluate and sort materials by assessing these properties. This is because both conductivity and permeability may be affected by the material's compositions, microstructure, residual stress or thermal treatment.

3.1.1 Low Conductivity Applications

As metals are good conductors, the eddy current inspection approach has become an attractive and well-established technique in the metal processing industry for monitoring the quality of the product. However, over the recent years, the eddy current approach has been of interest in low conductivity applications. The motivation for extending the investigation with this method is due to the freedom to make electrical measurements without applying electrodes or measuring plates directly in contact with the measurement samples, which sometimes occurs in electrical impedance applications. The electromagnetic method avoids the difficulties of applying electrodes, which may leave a deposit on the sample requiring further clean-up tasks on the sample for the manufacturers [59].

Some of the early low conductivity proposals for electromagnetic induction were in the medical field, with studies focused on non-imaging medical applications [60-62]. In [61], an inductively coupled conductivity meter was used to measure the equivalent homogeneous resistivity of the human chest and its fluctuation as a result of the pumping of the heart and respiration. The conductivity in the lung changes according to the amount of air in the lung. By monitoring the change in conductivity in human tissues, it has found that it is possible to detect brain edema, which is often induced by trauma to the skull, causing edema to propagate from the point of the trauma [62]. By using the interior low conductivity

distribution of the biological tissue, the potential applications of imaging in medical applications were researched [63-66]. The distribution of other electromagnetic parameters for example the permeability has also been investigated [67]. These multi-channel inductive measurement methods for imaging are often termed magnetic induction tomography (MIT).

Apart from the study of the eddy current technique in the medical field, the inspection method is also been considered in food industry applications. The applications included in process monitoring, quality assessment of meats, fruits and vegetables and processed foods [68-71]. As the conductance of lean muscle tissue is 20-30 times greater than fat, by measuring the electrical conductance of meat samples, the lean meat percentage of carcasses (duck, swine, beef, sheep, etc) may be determined. This helps in classification in the meat industry to ensure the consistency of quality. In a food process line, the existence of a metal fragment or contaminant in the environment is may occur occasionally, such as with food packaging or deposits from the faulty machines. With the difference in conductivity of the metal contaminant and the food (often below 5 Sm^{-1}), the foreign body is able to be detected to make sure safety of consumption.

With the capability of detecting the conductivity as well as the distance from the test coils to the sample (known as lift-off) [72] this method is suitable to be deployed in harsh industrial environments such as in the measurement of wall thickness of a glass furnace as in this research. This is because the glass melt has a low but significant conductivity as discussed in Chapter 2, which depends on its temperature. With this, by measuring the distance of the sensor with the glass melt will indirectly show the furnace wall surface distance.

3.2   Principle of Operation of Eddy Current

Eddy currents are created through a process called electromagnetic induction. When an alternating current is passed through an excitation coil, an alternating magnetic field is produced in and around the coil. By placing a test specimen, which is electrically conductive, in close proximity to this excitation coil, the magnetic field $B(x, y, z)$ that was generated interacts with the test specimen and generates currents in the specimen, which are called eddy

currents. Eddy currents flow in closed loops with the specimen and a receiving coil can be used to monitor their phase and amplitude.

Variations in the electrical conductivity $\sigma(x, y, z)$ and permeability $\mu(x, y, z)$ or a flaw in the test object will change the distribution of the eddy currents within the sample. This will correspondingly change the phase and amplitude of the measured field in the receiving coil. As an example, an arrangement consisting of a single pair of excitation coil and receiving coil with the induced eddy current flow is shown in Figure 10.
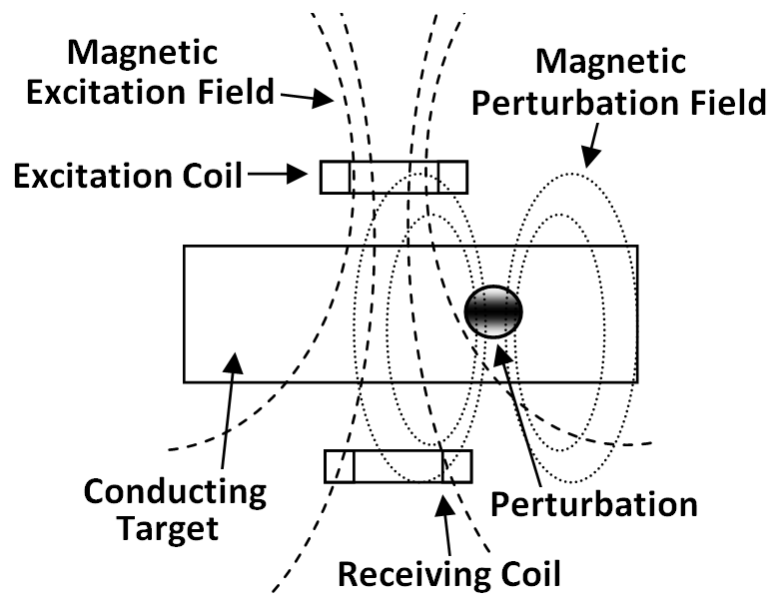
Figure 10 The eddy currents flow in closed loops tending to follow the axis of the coils, increasing in current density from the axis toward a maximum, the location of which depends on the particular geometry [73]

By making the following assumptions, the magnetic field within the measured space is presented in Equation 1 and Equation 2 [74]

     1. Assuming three dimensional case

     2. Neglecting free charges

     3. Material are assumed to have linear and isotropic electrical and magnetic properties

     4. Displacement current effects are ignored

$$\nabla \times \left\{ (\sigma(x,y,z) + j\omega\varepsilon_0\varepsilon_r)^{-1} [\nabla \times [\mu(x,y,z)^{-1}\boldsymbol{B}(x,y,z)]] \right\} = -j\omega\boldsymbol{B}(x,y,z) \qquad \textbf{Equation 1}$$

$$\nabla \cdot \boldsymbol{B}(x,y,z) = 0 \qquad \textbf{Equation 2}$$

Frequencies used for mutual inductance imaging are generally low; hence the wavelengths are considerably larger than the dimensions of the object space in order for the entire sensor to be operating within the electromagnetic near zone i.e.

$$\omega \ll \frac{2\pi c}{1} \qquad \textbf{Equation 3}$$

where 1 is the maximum width of the object space. At these frequencies, the induced displacement currents within the insulating regions of the object space are small and can be ignored. Consequently the $j\omega\varepsilon_o\varepsilon_r$ in Equation 1 can be neglected and the equation can be rewritten as below.

$$\nabla \times \left\{ (\sigma(x,y,z))^{-1} [\nabla \times [\mu(x,y,z)^{-1}\boldsymbol{B}(x,y,z)]] \right\} = -j\omega\boldsymbol{B}(x,y,z) \qquad \textbf{Equation 4}$$

In electromagnetic induction, an eddy current is created in the sample with the response to the applied field. From Lenz's law, the induced eddy currents produce a magnetic flux that opposes the applied field penetration into the sample, consequently a reduction of the total flux in the sample. The depth of penetration of the electromagnetic field into the a sample in the object space is determined by the skin depth, δ with the equation of

$$\delta = \sqrt{\frac{2}{\omega\sigma\mu_0\mu_r}} \qquad \textbf{Equation 5}$$

where

ω: Angular frequency of current

σ: Conductivity of sample

μ_o: Permeability of free space ($4.\pi \times 10^{-7}$ H/m)

μ_r: Relative permeability

The skin depth gives the information on the values of detectable conductivity relative to the applied frequency. The skin depth of the sample at the frequency of interest must be comparable to the diameter of the sensor. This is to ensure that the attenuation or the change in the applied field will be significant enough to be detected. With different applications, frequencies used vary from a few hertz to Megahertz. For low conductivity bio-medical applications, the operating frequencies are generally higher, which are above 1 MHz [75-78]. The process industry for metallic and ferromagnetic has been extensively using the eddy current inspection method, which typically operates up to 500 kHz [79, 80].

3.2.1   Electromagnetic Effects

The magnetic field change, $\Delta\boldsymbol{B}$, produced by a target object, will generally have real and imaginary components as an effect of the existence of the permeability, permittivity and conductivity of the target, which contributes to the phase change. The phase change can be represented as the following phase diagram [81].
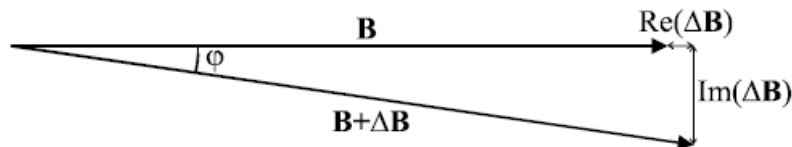
Figure 11 Phasor diagram representing the primary (B) and secondary (ΔB) magnetic fields detected and the total detected field (B + ΔB) with φ angle of lagging the primary field

By exciting the object space with a magnetic field created by one or more excitation coils, the eddy current field resulting from the introduction of an object can be measured by the detection coils around the outside of the object space. Depending on the material's electromagnetic properties, it changes both the magnitude and direction of the interrogating field. The material of the object can be either ferro / ferri magnetic ($\mu_r > 1$) and/ or has a high electrical conductivity. The visual impressions of the electromagnetic effects for these materials are represented in Figure 12.

Target
(40 mm dia.)
insulator
ferrite
aluminium

Object does not
affect the lines of
magnetic flux

Flux lines are drawn
into the target

The magnetic field
cannot penetrate the
target due to eddy
current effects

(a) Model   (b) Air Target   (c)Ferrite Target   (d) Aluminium
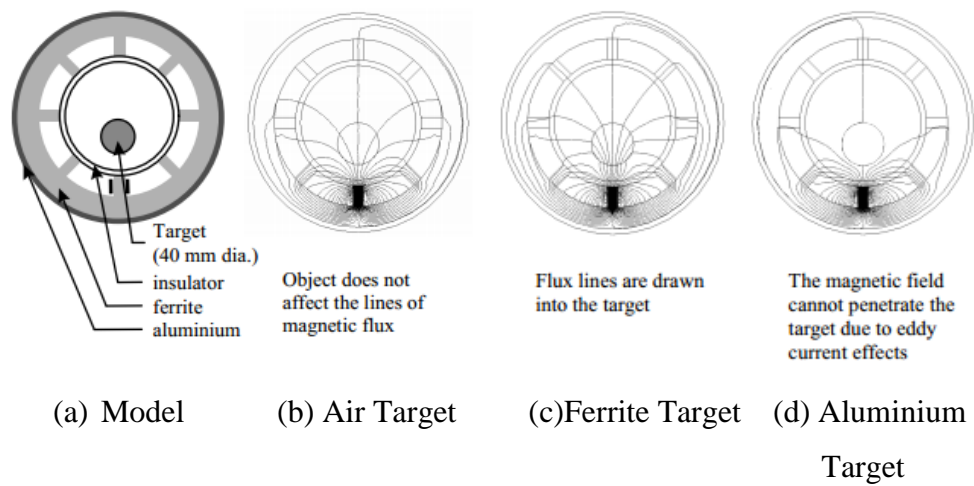
Target

Figure 12 Electromagnetic effects for different materials [82]

a)   Background signal

b)   Effect of magnetic material

c)   Effect of conducting material

d)   Effect of low-conductivity material

Magnified
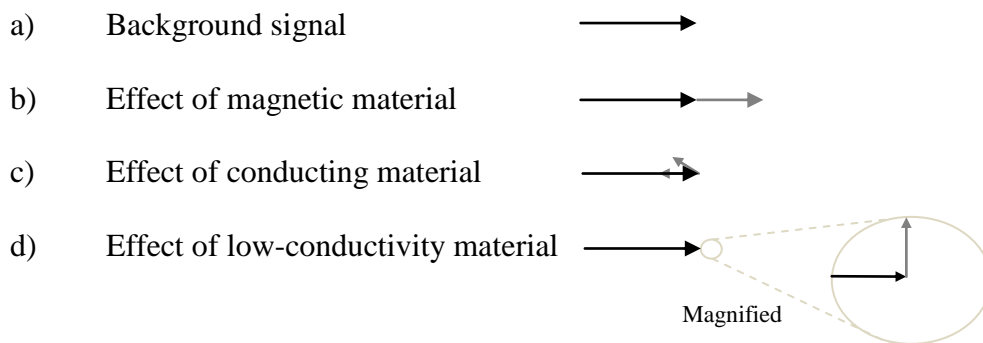
Figure 13 Phasor diagram for electromagnetic effects of different materials [83]

Figure 12(a) shows the schematic of the setting when a target with a 40 mm diameter is placed in an 8 poles electromagnetic induction tomography sensor with the object space of 200 mm. Figure 12(b) illustrated the undistorted distribution of magnetic field when air target is introduced.

In the event when a magnetic and non-conducting object is introduced, e.g. ferrite target in Figure 12(c), it attracts and concentrated the magnet flux flow through the object. As a result, it increases the mutual coupling between coils. This tends to increase the detected signals.

The detected signals coupled to the receiver coils are in phase with the transmitting primary field. The phasor diagram of this phenomenon is indicated as Figure 13(b).

When a highly conducting and non magnetic material ($\mu_r \approx 1$), e.g. aluminium or copper is placed in the sensing space, as shown in Figure 12(d), the development of eddy currents in the object target tends to limit the penetration of the magnetic field as it generates a secondary magnetic field opposing the applied field. The depth of the limitation of penetration of the applied field is known as skin depth, which was discussed in the previous section. Low conductivity non-magnetic targets have conductivities that are much lower in magnitude than in metals and the permeability are similar to free space. In the application of this research, the eddy current induced in the glass melt is measured. As illustrated in Figure 13, the imaginary component will be dominant; hence, the phase shift would be perpendicular to the primary magnetic field.

3.3   Analytical solutions

To solve the eddy current problem, an analytical solution has been presented by Dodd and Deeds in [84]. The solution provides several electromagnetic field quantities and the impedance of the coil which gives acceptable approximations to a wide range of practical cases. Demands for increases in sensitivity of detection, precision in characterisation and better flexibility have led to the development and application of more sophisticated approaches [85-87].

3.3.1   Single Layered Conductor

In [84], Dodd and Deeds proposed that there will be coil inductance changed for circular air cored coil when placed above a conductive plate. For the application to be valid, the conductive plate has to be larger than the axially symmetric coil. The solution is valid for a single turn coil consisting of a non ferromagnetic conductor. The conductive plate is assumed to cover an infinite half space and consist of two layers. One is the base conductor that has been clad / coated, another is a conducting material. The geometry of the coil above the conductors is represented as Figure 14.
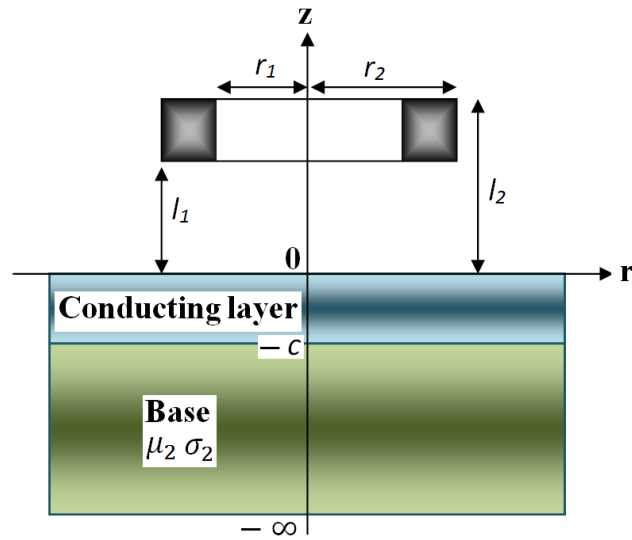
Figure 14 Rectangular cross-section coil above a two-conductor plane [84]

The dimensions of the geometry may be summarized as follows. The cladding thickness is c. The lift-off between the coil and the cladding surface is l_1 and the thickness of the coil is l_2-l_1. The inner radius of the coil is r_1 and r_2 is the outer radius.

To assume that the material is a single layer, the base conducting material can be treated as air, or $\sigma = 0$. With this assumption, the schematic can be represented as single layer as the following figure.
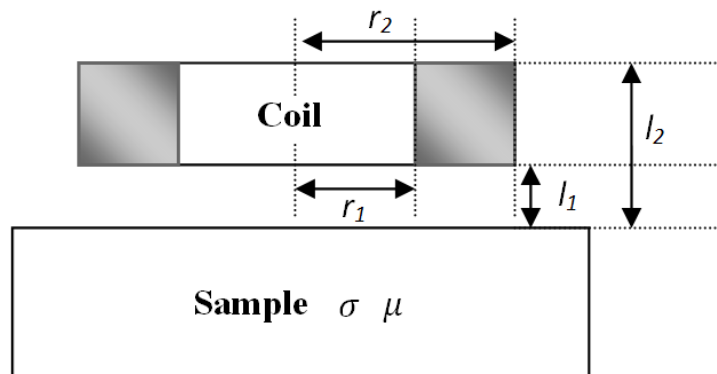
Figure 15 Simplified schematic diagram of coil

The presence of the conductive material change the complex inductance can be expressed as

$$\Delta L(\omega) = L(\omega) - L_A(\omega)$$ **Equation 6**

where

$L(\omega)$: Coil inductance over conducting sample

$L_A(\omega)$: Coil inductance in free space

The formulae of Dodd and Deeds for the changes of rectangular coil inductance on a conductor with free space is rearranged by [88] and shown as follows.

$$\Delta L(\omega) = K \int_0^\infty \frac{P^2(\alpha)}{\alpha^6} A(\alpha)\emptyset(\alpha)d\alpha$$ **Equation 7**

where

$$\emptyset(\alpha) = \frac{(\alpha_1 + \alpha)(\alpha_1 - \alpha_2) - (\alpha_1 + \alpha_2)(\alpha_1 - \alpha)e^{2\alpha_1 c}}{-(\alpha - \alpha_1)(\alpha_1 - \alpha_2) + (\alpha_1 + \alpha)(\alpha_1 + \alpha_2)e^{2\alpha_1 c}}$$ **Equation 8**

$$\alpha_i = \sqrt{\alpha^2 + j\omega\sigma_i\mu_i}$$ **Equation 9**

$$K = \frac{\pi N^2}{(l_2 - l_1)^2(r_2 - r_1)^2}$$ **Equation 10**

$$P(\alpha) = \int_{\infty_1}^{\infty_2} xJ_1(x)dx$$ **Equation 11**

$$A(\alpha) = (e^{-\alpha l_1} - e^{-\alpha l_2})^2$$ **Equation 12**

where

α : Integration variable;

ω : Angular frequency of excitation current;

μ : Permeability of the conducting plate;

μ_0 : Permeability of free space;

σ   : Conductivity of the conducting plate;

$J_1(x)$: First-order Bessel function

The model is assumed to be a linear, isotropic and homogenous medium, with magnetic permeability constant. Apart from that, the conductivity is assumed to be higher than the product of the permittivity and angular velocity of the driving current.

3.3.2   *Multi Layer Conductor*

Continuous conductivity profile determination is important in many applications. Some of these included coating, surface treatment and for quality inspection. As the proposed method by Dodd and Deeds is limited to single or two layered conductor, it is hence limited to applications with just a single step change in conductivity. For continuous conductivity variations, the problem can be treated in the method presented by Cheng in [89] if a piecewise approximation is made to the represent the conductivity profile. The solution placed a cylindrical air-cored coil above a finite number of layers, which are subdivided into a number of parallel homogeneous layers for the approximation of a varying conductivity profile. Each layer is given a constant conductivity and permeability. In the work of [86, 90, 91], smoothly varying and continuous conductivity profile was measured according to a piecewise approximation and proved to meet to the real solution.

In order to reduce the measurement errors, Yin [92] has improved the system from Cheng. The approach is expressed to have a measurement of coil inductance for the layered conductor, compared with the reference conductor with known conductivity. The equation expressing the inductance changed of the coil will be presented as follows in a different form that included the case with the reference conductor.
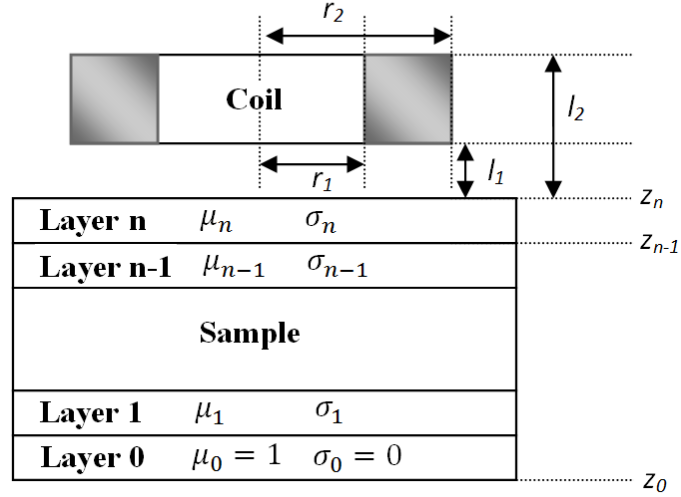
Figure 16 Schematic diagram of the layered conductor model

The geometry considered is shown in Figure 16. A circular coil of rectangular cross section is located above a layered non-magnetic and conductive material. The impedance of the single turn coil is determined by solving the corresponding differential equations. The impedance is then calculated by assuming that the current density is uniform over the cross-section of the coil.

$$\Delta L = K \int_0^\infty \frac{P^2(\alpha)}{\alpha^6} A(\alpha) \left(\frac{W_{12}}{W_{22}} - \frac{U_{12}}{U_{22}} \right) d\alpha \qquad \text{Equation 13}$$

where

$$U = H_n \cdot H_{n-1} \cdot H_{n-2} \cdot \ldots H_0 \qquad \text{Equation 14}$$

$$W = H_r \cdot H_0 \qquad \text{Equation 15}$$

$$H_k = \frac{1}{2} \begin{bmatrix} \left(1 + \frac{\mu_{k+1}\alpha_k}{\mu_k\alpha_{k+1}} \right) e^{(\alpha_{k+1}-\alpha_k)\cdot z_k} & \left(1 - \frac{\mu_{k+1}\alpha_k}{\mu_k\alpha_{k+1}} \right) e^{(\alpha_{k+1}+\alpha_k)\cdot z_k} \\ \left(1 - \frac{\mu_{k+1}\alpha_k}{\mu_k\alpha_{k+1}} \right) e^{(-\alpha_{k+1}-\alpha_k)\cdot z_k} & \left(1 + \frac{\mu_{k+1}\alpha_k}{\mu_k\alpha_{k+1}} \right) e^{(\alpha_k-\alpha_{k+1})\cdot z_k} \end{bmatrix} \qquad \text{Equation 16}$$

$$A(\alpha) = (e^{-\alpha l_1} - e^{-\alpha l_2})^2 \qquad \text{Equation 17}$$

$$P(\alpha) = \int_{\alpha r_1}^{\alpha r_2} x J_1(x) dx \qquad \text{Equation 18}$$

$$K = \frac{\pi \mu_o N^2}{(l_1 - l_2)^2 (r_1 - r_2)^2}$$

<div align="right">**Equation 19**</div>

$$\alpha_k = \sqrt{\alpha^2 + j\omega\mu_k\sigma_k}$$

<div align="right">**Equation 20**</div>

where

α	: Spatial frequency variable
U, H, W	: Transfer matrices
K	: Prefactor
$J_1(x)$	: First factor of Bessel function
σ_k	: Conductivity of layer k
μ_k	: Permeability of layer k

The interface between layers *k* and *k+1* occurs at a depth z_k. The base layer for the conducting layers starts at the base of the material which is numbered as layer 0. The total number of layers is n+1. When the model has a smoothly varying and continuous conductivity profile, the changes in conductivity and permeability of its different layers are substitutable by the value of the conductivity and permeability of the middle layer of the conductor in the solution.

3.3.3 Simplified Models

Research into analytical solution has been established as shown in [93] as a further simplified development of the solution from Dodd and Deeds. This approach enables the calculation to be carried out by cancelling the conductivity and frequency terms, which the change in the reactance of the coil is nearly independent to these parameters compared to the change in the lift-off. This method enables a fast computational time for lift-off analysis.

The model in this work is described as a conductor with one layer, constant permeability and conductivity as proposed by Dodd. The material at the base is classed as air, with $\sigma = 0$. Consequently, for Equation 16, the conductivity for the base material σ_2 is replaced with zero giving the following equation.

$$\alpha_2 = \sqrt{\alpha^2 + j\omega\mu_0\sigma_2} = \alpha \qquad \textbf{Equation 21}$$

Substituting Equation 21 into Equation 8

$$\emptyset(\alpha) = \frac{j\omega\sigma\mu_0(1 - e^{2\alpha_1 c})}{(\alpha - \alpha_1)^2 + (\alpha + \alpha_1)^2 e^{2\alpha_1 c}} \qquad \textbf{Equation 22}$$

This first approximation for this analytical solution is that for Equation 22, the $\emptyset(\alpha)$ varies slowly with α compared to the rest of the integrand. The equation reaches its maximum at a characteristic spatial frequency α_0. α_0 is defined to be one over the smallest dimension of the coil. To evaluate $\emptyset(\alpha)$ at α_0, α_0 is taken as a constant and taken outside of the integral from Equation 7.

$$\Delta L(\omega) = \emptyset(\alpha_0)\Delta L_0 \qquad \textbf{Equation 23}$$

where

$$\Delta L_0 = K \int_0^\infty \frac{P^2(\alpha)}{\alpha^6} A(\alpha) d\alpha \qquad \textbf{Equation 24}$$

The second approximation originates from the coil dimension and has to satisfy $j\omega\sigma\mu_0 \ll \alpha_0^2$ which gives the expression as follows

$$\Delta L(\omega) = \Delta L_0 \frac{j\omega\sigma_1\mu_0(1 - e^{2\alpha_0 c})}{4\alpha_0^2 e^{2\alpha_0 c}} = j\frac{\Delta L_0\mu_0}{4\alpha_0^2} \cdot \omega\sigma_1(e^{-2\alpha_0 c} - 1) \qquad \textbf{Equation 25}$$

From Equation 25, the imaginary component is dominant and the real part for the inductance is negligible. Hence, the imaginary part is proportional to the conductivity and the angular frequency change.

The phase of inductance data can be derived and expressed as

$$\theta = tan^{-1}\left[\frac{\frac{\Delta L_0 \omega \sigma \mu_0}{4\alpha_0{}^2} \cdot \omega \sigma_1 (e^{-2\alpha_0 c} - 1)}{L_0}\right] = tan^{-1}(\omega \sigma \mu_0 \cdot const)$$

Equation 26

When the above equation is applied to the current research project, the parameter ΔL_0 is a constant that is affected by the target (i.e. glass melt / water) surface level. L_0 is the reference measurement, which is taken from the background's inductance (i.e. inductance without the presence of target). With multiple coil pair measurements, the phase measurements are able to calculate the lift-off level of the target, eliminating the influence of the conductivity and excitation frequency.

At a small phase angles, Equation 26 can be approximated as

$$\theta = tan^{-1}(\omega \sigma \mu_0 \cdot const) \approx \omega \sigma \mu_0 \cdot const$$

Equation 27

For different pair of coil measurements,

$$\theta_1 \approx \omega \sigma \mu_0 \cdot const_{01} \cdot \Delta L_{01}$$

Equation 28

$$\theta_2 \approx \omega \sigma \mu_0 \cdot const_{02} \cdot \Delta L_{02}$$

Equation 29

The conductivity and frequency terms may be cancelled when Equation 28 is divided by Equation 29, giving the following ratio [93].

$$\theta = \frac{\theta_2}{\theta_1} = const \cdot \frac{\Delta L_{02}}{\Delta L_{01}}$$

Equation 30

From the equation, θ is solely related to the target surface level.

3.3.4   Limitations of Analytical Solution

3.3.4.1 Steel Structure

Although there are many successful cases of the application of the solutions by Dodd and Deeds, most of the applications are mainly measuring the change of impedance from the simple setup with a test specimen next to the coils. The simplified analytical method is a complimentary technique used in this research. The approach is able to provide solutions for lift-off level measurements with a symmetrical geometry, however, it does not describe cases when steel beams exist, which is the realistic case in the furnace environment. Due to the fact that steel is the main exterior cladding and support of the furnace, it is essential to take into consideration the effect of the steel in the measurement data. The signal induced by the steel will be much greater than the signals from the glass melt. Also, the geometry of the steel structure is not constant in every furnace; which introduces a difficulty in selecting the appropriate measurement method for general use.

Following the effort in online monitoring steel transformation in [94], it was found that by using a spectra frequency, the phase change that is influenced by the steel is less significant at high frequencies. In order to verify this, a simulation following the Dodd and Deeds method and setting as shown in Figure 15 was carried out, with the formulas encoded with MatLab software. The coil used in the simulation is an air cored coil with single turn and 200 mm diameter. It measures the inductance from 1 Hz to 10 MHz for both samples with distance of 200 mm between coil and sample. The comparison output of the simulation in terms of inductance versus frequency is shown in Figure 17 for glass melt and steel samples, with sample thickness of 400 mm and 5 mm respectively used in the simulation. The chosen parameters, i.e. samples thickness, coil diameter, lift-off level are an approximated scale-down value from the experiments in this research.
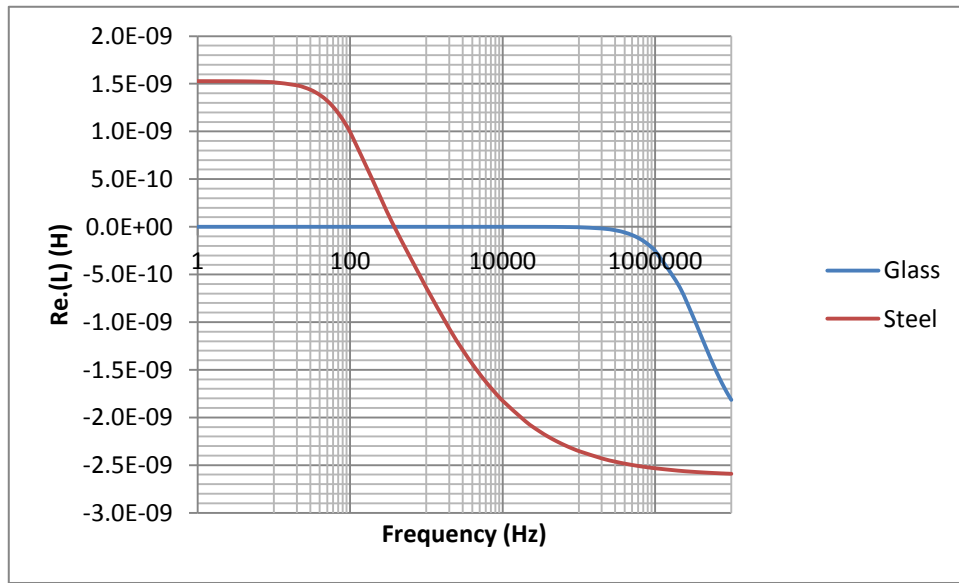
(a)
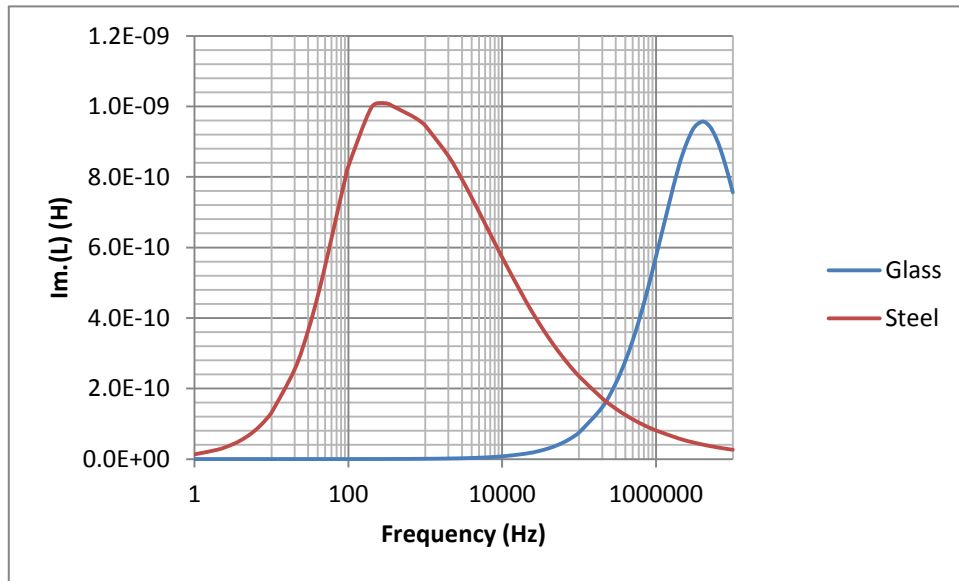
(b)

Figure 17 Frequency spectra of the mutual inductance for molten glass and steel samples

(a) real part (b) imaginary part

Steel is a ferromagnetic target; it has a conductivity here of 1.1 MSm^{-1} and a relative permeability of 100. The multi-frequency sensor acts on the steel sample in two ways. At low frequency, it tends to magnetise the metal, hence, increasing the inductance [95]. Observing the real part of the inductance, as the magnetisation is dominant at low frequencies, the inductance changed due to the target is positive. As the frequencies increase, the alternating current magnetic field induces the eddy current in the target. This induces the opposing effect of the eddy current with the driving current, as a result, the reduction in coil's inductance. The decrease in the inductance change leads the value to the negative value. When both of the effects are in balance, the inductance change due to the target is zero, which zero cross at the effective frequency. In the imaginary part, it has a maximum value, where the frequency is defined as the characteristic frequency of the measurement. This characteristic frequency varies according to the conductivity change in the sample.

The conductivity of the molten glass is 10 Sm^{-1} and the permeability of the glass is assumed to be as vacuum, i.e. $\mu = \mu_0$. Along with the increase of the excitation frequency, the real part in the mutual inductance starts to decrease at higher frequencies for the molten glass. This is related to the skin depth effect as discussed previously with formula shown in Equation 5. As the skin depth equation shows, in order to have a negligible effect of a certain material in the measurement, appropriate frequencies must be chosen according to the conductivity of the material. By observing the peak value of the maximum in imaginary inductance, the appropriate excitation frequency can be selected by different conductivity ranges. In practical applications, the selection of appropriate frequencies is able to obtain the optimal imaginary measurement sensitivity.

Aiming at the difference in inductance response with frequencies spectra for two samples, at relatively low frequencies, the steel inductance varies significantly compared to the molten glass. The variation of the mutual inductance for molten glass is more susceptive at higher frequencies. Hence, to avoid the effects introduce by the steel, the higher range of frequencies is chosen in this project in order to obtain the changes in inductance that is dominated by the effects of the glass and the changed due to the steel are relatively constant with frequency.

3.3.4.2 Spatial Analysis

In order to obtain data in the region of interest from measurements of inductance, often coils are made to surround the material region [75, 96, 97]. The analytical solutions from Dodd and Deeds discussed in Section 3.3.1 only focus on circular air cored coils with a rectangular conductor cross-section. Coils with different shapes and cross-sections, cannot be solved with these solutions. The orientation of the coils introduces different characteristics to the measurements; it has lead to the interest in researches in determining the optimum measurement sensitivity for different coil arrangements.

There are two contributions to the signal at the sensing coil; the primary signal that is induced by the field from the excitation coil and the secondary signal that is created by the eddy currents induced by the sample that produces the magnetic field. Comparatively, the primary signal is much larger than the secondary signal. A comparison of axial gradiometers and directional sensors termed Bx sensors was made by Watson et al [98]. An axial gradiometer may have two sensor coils that are placed equal distances on either side of the axis of symmetry of the excitation coil. The sensor coils are connected in series opposition such that there is a subtraction of the signals from the pair [99]. In [100], a planar gradiometer was designed and this follows the same principle as the axial gradiometer, but with the two sensor coils positioned symmetrically in the same plane as the excitation coil. In the comparison by Watson for low conductivity magnetic induction coils for biomedical applications, [101] the Bx sensors showed a better sensitivity than the gradiometer to the depth of saline. In order to reduce the primary field, Watson [101] has proposed a Bx sensor with an orientation of coils with a secondary coil placed at 90 degrees to the axis of the excitation coil.

From the preceding discussion, it can be seen that the gradiometer can be a very sensitive configuration, but the arrangement is also sensitive to the distance between the two sensing coils and the excitation coil. Two of the sensing coils have to be magnetically equidistance with the excitation coil for the primary field to induce equal signals in both measurement coils for it to be cancelled by subtraction during calibration [102]. Unfortunately, the gradiometer arrangement is also very sensitive towards temperature [73] due to thermal expansion. It was shown that the gradiometer provides inaccurate measurements when the temperature of both detecting coils is different. This is obviously not an ideal situation for a sensor which is to be used in the environment under the furnace as it is hard to maintain the

operational temperature at a constant valve. Both of the receiving coils' separation from the excitation coil must to be stable and equal distance, which is often difficult to be achieved due to manufacturing tolerances and matching the thermal expansion of materials. Although by comparison the Bx sensor appears to be more beneficial, it has shown its imperfection as it has to be soldered on the PCB board and this will introduce problems on its stability of temperature.

An alternative way of allocating the exciting and detecting coils has been proposed in [72]. Both of the coaxial symmetrical coils have been successfully used to measure both water level and the conductivity of saline simultaneously with low error rate of typically 1%. It has introduced a method that is suitable for online measurements as a small portable instrument. However, this orientation will limit the range of obtaining the measurements as it does not provide enough of independent spatial data for measuring the distance to the glass, whilst also rejecting the signal caused by the supporting steel framework.

A planar system that uses coil positions which are different from the conventional way was obtained by [103]. The coils are arranged by having all of the axes of the coils parallel to the plate under inspection. The traditional way is often arranging the coils' axes parallel to the object of interest. This novel idea proves that it is more sensitive in measuring the zone of interest. The coil array in [1] has taken the advantage of this coil orientation. In this example, there are 8 sets of coil arrays printed on a circuit board with their axes perpendicular to the measuring object. Each set of the coils (one transmitting coil and one receiving coil) is positioned on either side of the printed circuit board. This design shows higher sensitivity for its measurement with higher separation between the exciting and the receiving coil.
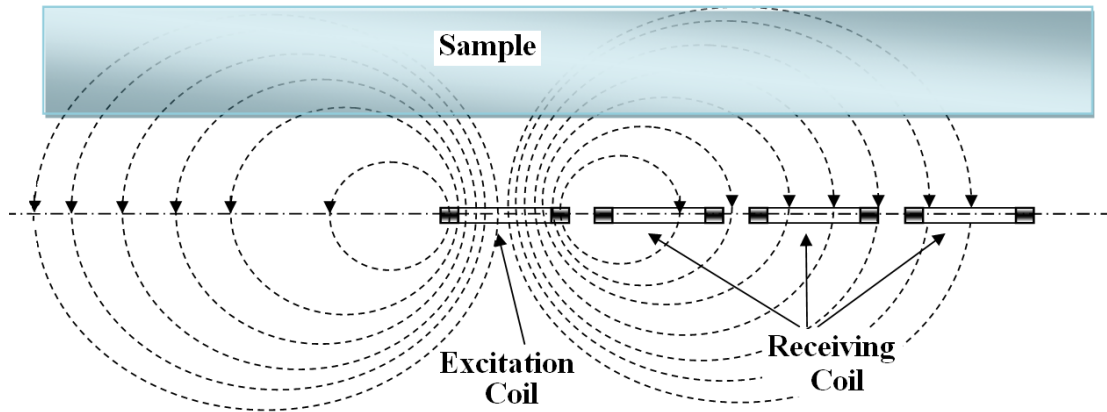
Figure 18 Planar coils array (one excitation coil and three receiving coils) alignment with excitation field

The distance of sensing range between sets of coils can be illustrated from the flux lines as shown in Figure 18. To localise or detect the change in the conductivity of the target, the effect of the distance between the exciting and receiving coils can be exploited to enable a wider range of view on the lift-off distance of sample from the target. The magnitude of the sensitivity of the sensor coil to the eddy currents is a function of their relative positions and orientations to the excitation coil.

As an example of the discussion in the previous paragraph, Figure 20 shows the phase change values for different distances of coil pairs from a plane saline target obtained by simulation. As shown in Figure 19, the simulation is based on a planar coil arrays system with the distance to the target of 300 mm. The saline depth is 100 mm. The coils are square, with dimensions of 70 mm x 70 mm x 1 mm. The simulated results were obtained with Ansoft Maxwell software, with the excitation coil operating at 1 MHz. The target object is saline with conductivity of 9 Sm^{-1}. 1 transmitting coil and 7 receiving coil were used in this simulation. The simulation setup is shown in Figure 19. The distances between the coil centre for the transmitting and receiving coils are 78 mm, 156 mm, 234 mm, 312 mm, 390 mm, 468 mm, and 546 mm.
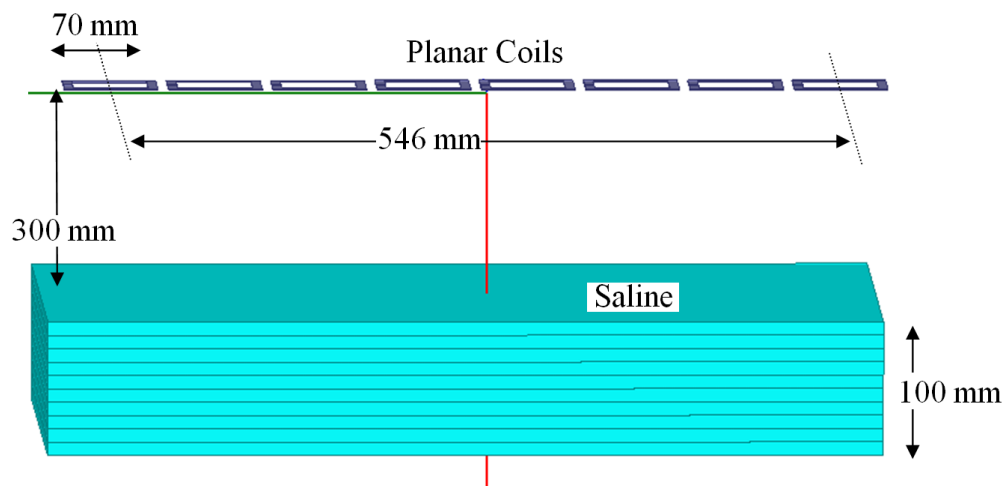
Figure 19 Simulation setup for planar coils with different distances
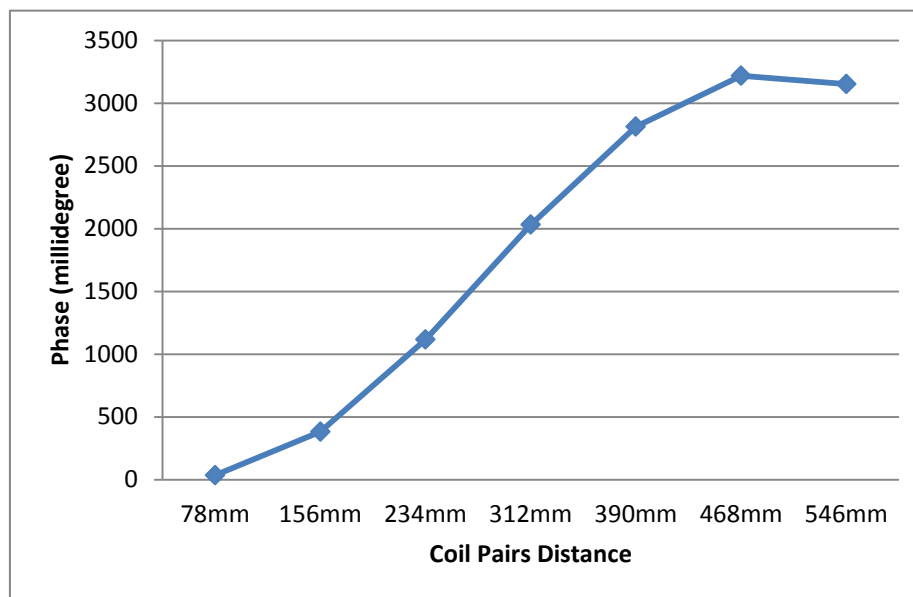
Figure 20 Effect of coils pair centres distances to the phase change

As the distances of coil centres between the transmitting and receiving coils is moved further apart, higher phase changes are produced. However, as the separation increases, the signal amplitude reduces and consequently if the coils are too far apart, the noise of measurement increases which affects the results. With multiple excitations with different coils, a sequence of measurements of perturbation can be obtained from the detection coils in the form of induced voltages or mutual impedances. Also, multiple coils at different separation will benefit the user without having to physically move the coil to obtain multiple projections for better accuracy of estimations. Hence, as the geometry of the furnace in this project offers limited the freedom of choice for the coil shapes and arrangements options, the coil array in this project was designed as a planar multiple coils array.

3.4   Conclusions

The discussions in this chapter indicate that the eddy current inspection technique has been previously investigated for a range of medical applications and also used in food industry. The biological and food samples generally have a low electrical conductivity (e.g. below 10 Sm^{-1}) when compared to metals. Reports in the literature suggest that modest signal quality can be obtained in these cases. This background research has encouraged the application of eddy current inspection in this glass furnace application due to the similarity in low conductivity of the molten glass (typically around 5 to 15 Sm^{-1}) with those of biological tissues.

To solve the eddy current problem, analytical solutions based on the work of Dodd and Deeds have proposed the solution for the inductance measurements. However, these solutions assume a simple symmetrical geometry and therefore are not generally applicable in this research because the furnace surrounding contains large amount of structural steel. Therefore FEM simulation techniques were used to study the problem. According to the simulated values shown, the conductivity of the materials affects the frequency range that gives the highest signal sensitivity for the measurement. For molten glass, this frequency range is much higher than that of steel. Therefore, in this research, the range of frequencies for the measurement of molten glass was chosen to be from 500 kHz to 10 MHz.

It was found that increasing the distance between the exciting and receiving coils will also increase the range of view on the distance of the target. In simple terms, exciting and receiving coils which are close together have a short detection, or lift-off, range, whereas coil pairs which are further apart, may have a longer range of detection. There is a limit however, as the noise and the stability of the measurements decrease as the coil separation is increased. To obtain more measurement pairs values, multiple coils pairs with different distances will be used in the system reported in this thesis for a better accuracy in estimation of the properties of the target.

Chapter 4 Modelling Technique and Simulations

4.1   Introduction

For eddy current inspection, the solution to the forward problem is one of the fundamental computational challenges in order to predict the measurements according to the physical properties of the material in the sensing region, such as the conductivities of materials. The data obtained can be used in the inverse solution to recover the information of interest from the experiments results. However, these forward mathematical approaches are often restricted to simple geometries with simple conductivity distributions, whereas in most practical cases, geometries are often complicated and sometimes surrounded by different materials which would introduce complications in the mutual coupling measurements. Hence, a reliable and accurate calculating method is required, especially in this project, where the structure of the furnace and the steel support beams is irregular. Therefore this problem is too complex to be approached using calculations based on purely analytical solutions.

In order to provide a more flexible approach to address this complicated and 3-dimension case, the of finite element method (FEM) was adopted. Maxwell$^{®}$ v15 software, developed by Ansoft Corporation, was used, which exploits FEM to solve Maxwell's partial differential equations for electromagnetic fields. For this simulator, all the geometries are divided into many small tetrahedra elements and this is often referred to as the finite element mesh. The mesh creation can be done either manually, with the mesh being refined according to the percentage error settings by user or automatically by the software. The percentage errors are fed back each time to give an improved mesh distribution and this is repeated until the error rate falls below the defined threshold of tolerance. In order to have more precise calculations, more mesh can be set at a particular space and there are options of meshing according to length based or skin depth based which controls the size of each tetrahedra. In short, accuracy of the simulation depends to the size and number of tetrahedra. This method is benefit from the capability of fitting the mesh easily into the irregular shapes.

One of the advantages of the FEM method is that it enables fields to be plotted with ease to aid the understanding of field strength. It also allows new material properties to be set for the

geometries without being limited with the default materials only. However, the FEM simulations often have to compromise between the accuracy of solution and the significant simulation time, computing power and memory. In [1], the numerical method was used to obtain the response of the molten glass in the presence of the steel components. The results of the comparison between the simulated values and the measured value are very persuasive, which gives some confidence in the use of future simulations. However, one of the drawbacks of this method is that it is difficult to have the accurate measurements of the position of the steel for inclusion in the model.

4.2   Model Verification

The models used to determine the response of the sensor must contain an accurate description of the geometry of the sensor / furnace configuration. As the distance between the sensor and the glass in practical situations varies depending on the initial construction and the wear of the furnace during its life, the technique to model this is by representing the glass tank in horizontal layers and also assuming that the bottom of the furnace wall is in a flat condition, even though it is often not the case. If the bottom of the furnace wall is thick, the glass will be at a higher position from the sensor and this can be achieved in the model by setting the bottom layers as an electrical insulator such as vacuum, which equivalent to the refractory structure that has low conductivity. This method of horizontally layering the model geometry enhances the flexibility by having adjustable lift-off levels depending on the required thickness.

To verify the accuracy of the results of the horizontally layering method, a comparison of 2D and 3D modelling was carried out. A non-layered structure of 2D modelling was performed by using the software of Maxwell SV$^{®}$ (Ansoft Corporation) with an axi-symmetrical model. Consequently, the shape of the furnace in the verification test is compromised and assumed to be in a simple cylindrical shape. This is the same for the coil, which also must be cylindrical in shape and only a single coil is used in this model.

(a)

250mm (Radius of glass tank)

300mm
(Thickness of glass)

80mm
(Distance of glass and coil)

20mm
(Thickness of coil)

(b)
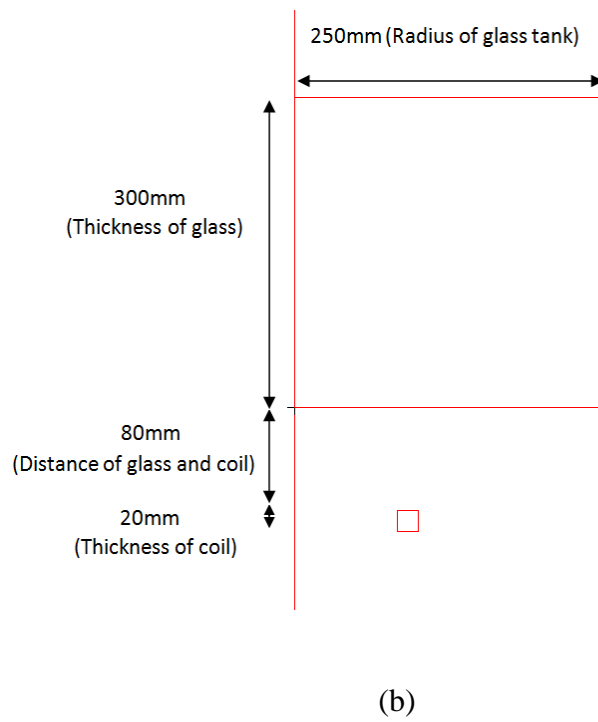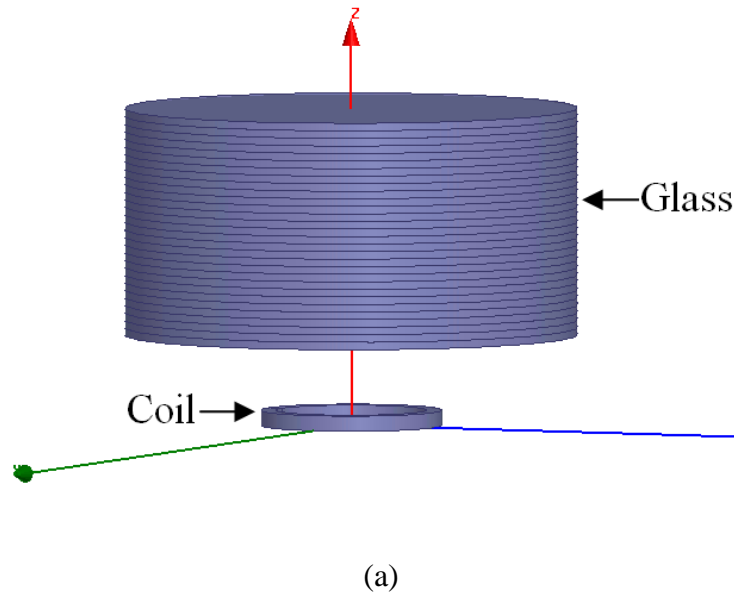
Figure 21 Geometry of the glass tank and coil in simulation for
(a) 3D in Maxwell® V15 (b) 2D in Maxwell® SV

To evaluate the reliability of layered modelling method across different frequencies, the models were simulated with values of 1 kHz, 10 kHz, 1 MHz and 10 MHz. Table 3 presents the comparison of impedances for both models.

Frequencies(Hz)	2D Maxwell® SV R (Ohm)	3D Maxwell® v15 R(Ohm)	Difference %
10 kHz	3.4930E-05	3.4725E-05	5.90E-13
100 kHz	5.4044E-04	5.3872E-04	3.19E-03
1 MHz	3.3772E-02	3.3708E-02	1.90E-03
10 MHz	3.5877E-01	3.5428E-01	1.27E-02

(a)

Frequencies(Hz)	2D Maxwell® SV L (H)	3D Maxwell® v15 L(H)	Difference %
10 kHz	3.5862E-07	3.5898E-07	1.00E-03
100 kHz	3.5857E-07	3.5922E-07	1.81E-03
1 MHz	3.5521E-07	3.5588E-07	1.88E-03
10 MHz	3.4442E-07	3.4482E-07	1.16E-03

(b)

Table 3 Impedance values of 2D and 3D simulations (a) Resistance (b) Inductance

The simulation results show that when comparing the layered 3D model with the non-layered 2D model, the impedance values obtained with the different frequencies generally agree to 99.99 %. However, the differences in values for the resistance become higher as the frequency increases. The differences in the values may be introduced by the difference in mesh settings in the simulations. For the 2D model, the calculation error rate and mesh sizes are not as flexible and adjustable as the 3D model. It is solely depend on the computer built-in settings and is not readily changeable by user. However, the differences of the impedance values obtained with different frequencies are very minimal; hence, this may be considered to be negligible.

This simulation comparison showed that the method of assigning different material, i.e. vacuum or glass using different layers is able to be used in the FEM modelling to represents the distance of coil from the molten glass in the future simulations. One of the additional benefits by layering the model is that the space in that particular layered area is limited for meshing, therefore, forcing a smaller mesh produced in each layer.

4.3 Modelling Convergence Test

In order to reduce the error rate and computational noise levels, the models for each analysis used the same mesh file, with same number of tetrahedra for all of the simulations with the same setups. The mesh process is carried out before calculating the mutual impedances between coils. The mesh is then imported into the simulations where the impedances due to the coupling of coils are calculated. In order to account for the main physical details of the system and also to accurately evaluate the eddy current effect, three models – the laboratory tank, the test rig and glass furnace were simulated separately. The former two of these models are shown in the following figure.
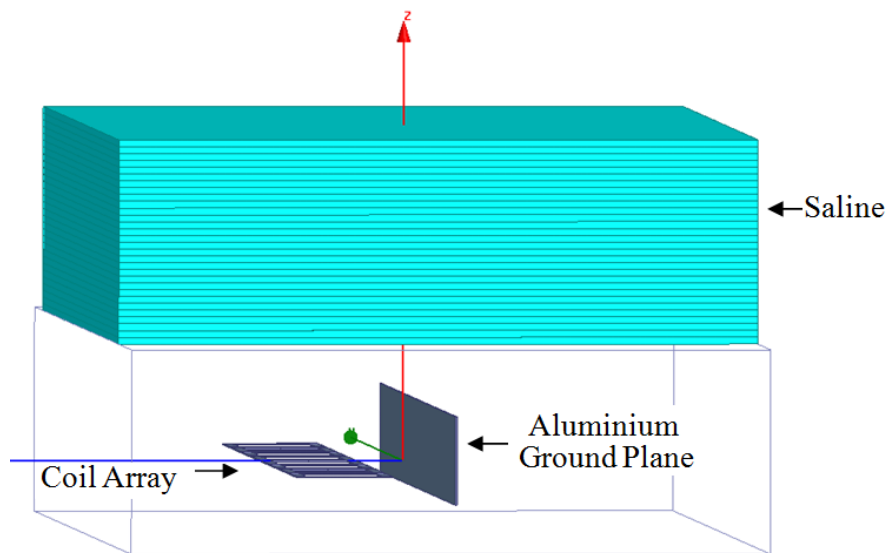
(a)
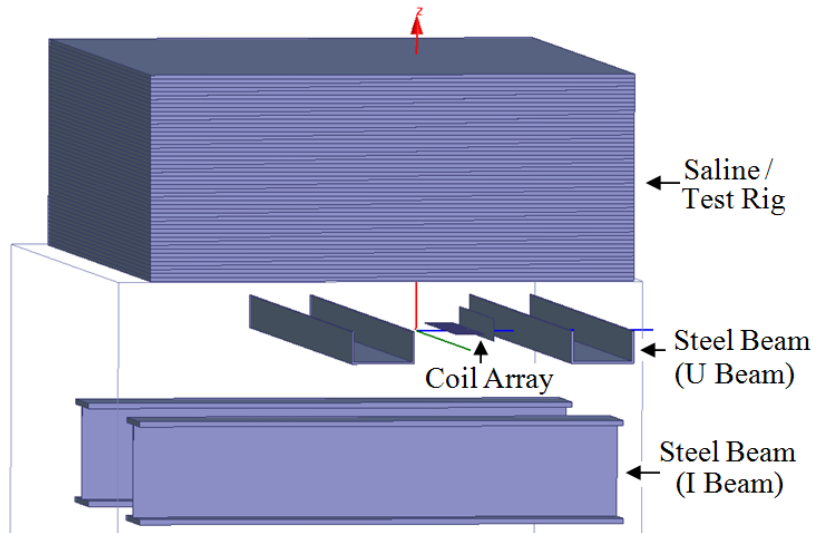
(b)

Figure 22 Simulation model of a) the laboratory experiment b) the test rig with steel structures

Figure 22(a) shows that the laboratory tank, which has no steel around it. This set up is used for the initial experiments to measure the effect of lift-off levels with saline prior proceeding to the setups where signals might be affected with the surrounding structures or materials that are conducting. Figure 22(b), is a more representative model of the furnace, which has included the steel beams contained in the supporting base. The models are layered for ease in setting of different lift-off levels.

To solve the eddy current problem in the Maxwell software, a collection of finite element tetrahedral meshes were created, which represented the shaped of all the components in the models. The accuracy of the modelling is determined by the number of tetrahedral in each mesh; in general the more tetrahedra, then the more accurate are the model. By using the same mesh arrangement for all of the simulations with just sufficient tetrahedral then the computational time can be reduced because the number of calculations is minimised.
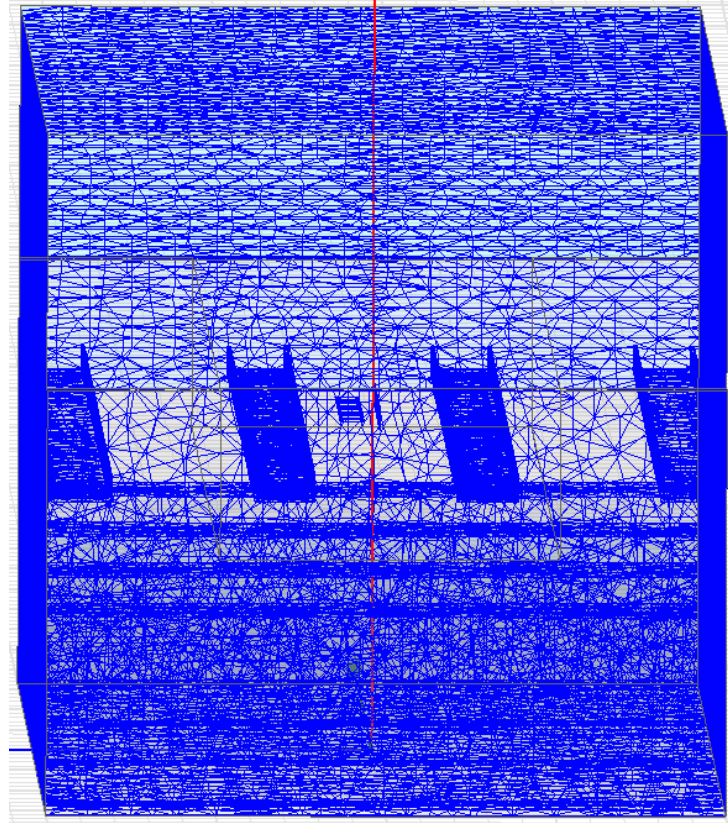
Figure 23 Mesh plotting of furnace model

Figure 23 shows an example of the type of mesh used to model the furnace structure. For areas where the width of material is thinner, as drawn in the model, a finer mesh is used with smaller tetrahedra. A finer mesh is also allocated at areas where the electromagnetic fields are changing more rapidly, such as around the conducting coils. This will consequently increase the mesh size, i.e. the total number of tetrahedral elements in the model. The choice of mesh size is crucial in the simulation as it affects the precision of the impedance calculations. However, a large mesh will significantly increase the computing time and computer memory required and therefore a convergence test was carried out in order to assess the most suitable simulation mesh settings.
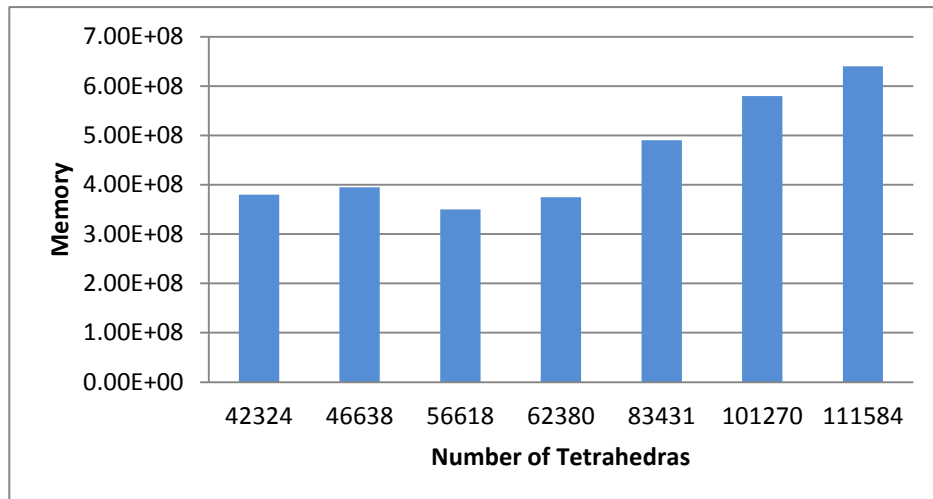
(a)
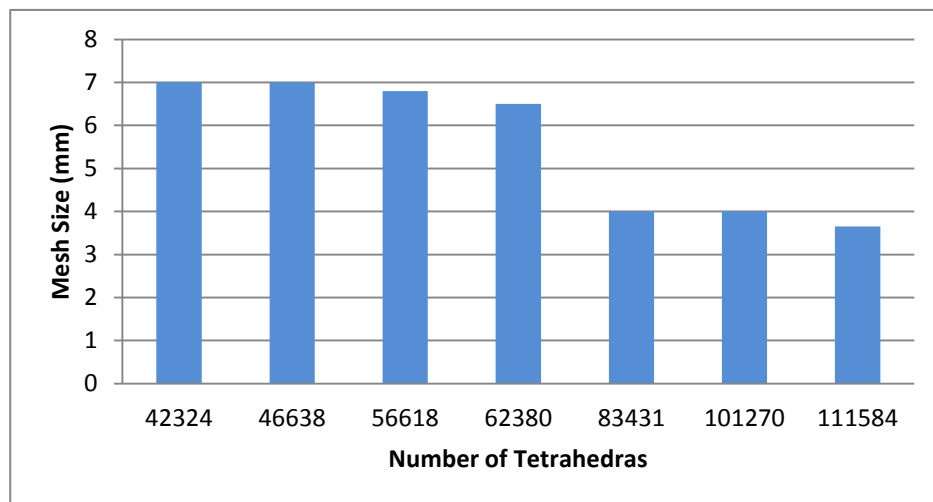
(b)
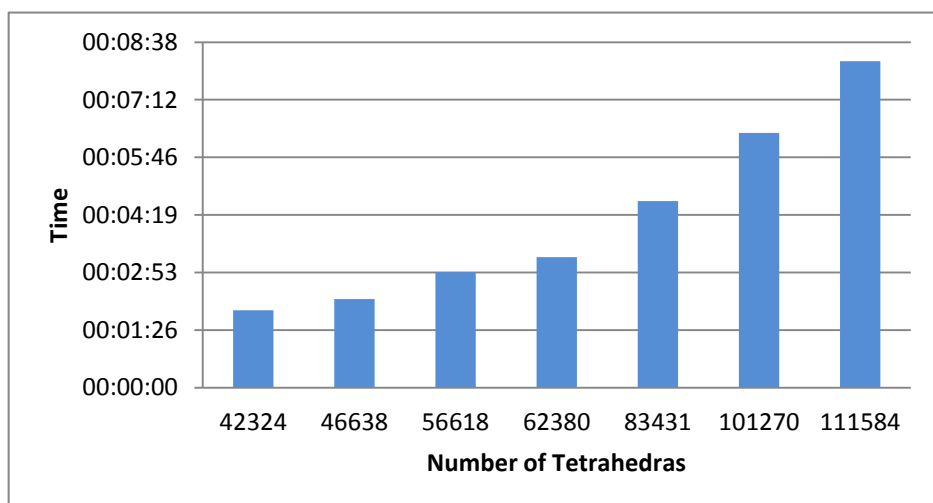
(c)
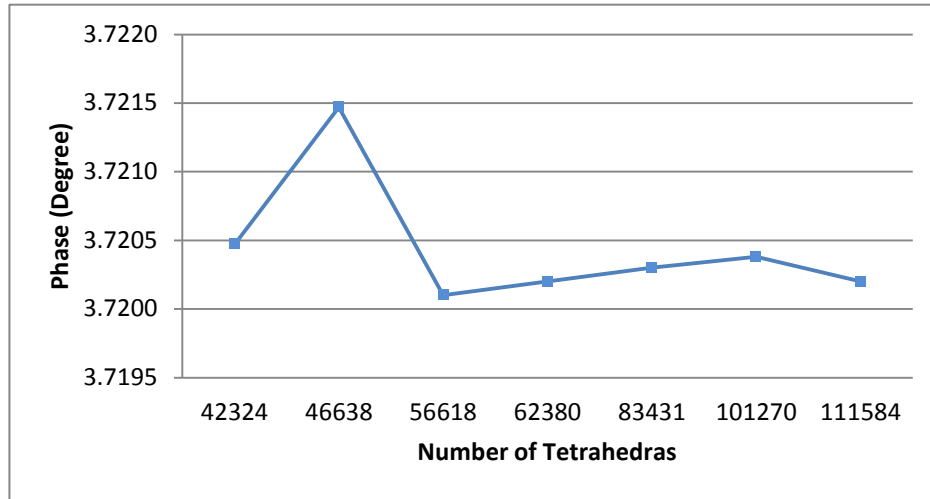
(d)

Figure 24 Example of a convergence test (a) Computing memory (b) Mesh size
(c) Computing time (d) Phase change measurements

Figure 24 shows the results of a convergence test on the model of the laboratory tank setup. The factors concerned are the computing time, mesh size, computer memory required, and the accuracy of the measurements. The size of the mesh is set to be increasing for every pass until target preset accuracy is achieved. With the increase in mesh size, the accuracy of the results improves, but at the cost of more computing memory and time.

The impedance calculations are observed with the effect of mesh increment. A laboratory tank setup with 50 mm depth of saline with conductivity of 11 Sm^{-1} is modelled. The saline conductivity is similar to the conductivity of the molten glass in the furnace. The distance between the coil and saline is 102 mm and the distance between the coil centre of the transmitting and receiving coil pair is 468 mm. Figure 24(d) shows that with the increase in mesh size, the change in the results in phase for 101279 tetrahedra and 111584 tetrahedra is not significant. The error rate set for 101279 is 2 % and the 111584 is 0.5 %. However, the laboratory tank mesh is chosen to be meshed into approximately 100,000 elements as the lower number mesh will require the compromise of having a higher error rate in its calculations and the higher number of mesh will require more computing time and memory usage.

The same convergence test was also carried out for the test rig and the furnace model to choose the optimal number of tetrahedra prior more simulations. The test rig was chosen to be meshed into approximately 300,000 elements and the furnace was meshed into approximately 500,000 elements, achieving the nominal accuracy of 2% in error rate for.

4.4   Frequency and Lift-off Response

Simulations can be used to study the frequency response of the sensor system to the different components in the model, for example the signals show the most responsive frequency for the sensor design towards the low conductive saline. Hence, by analysing the spectra of the signal it is possible to choose the best operating frequency range. Therefore, the frequency chosen for this analysis of frequency response is in the range from 100 kHz to 10 MHz because the induction spectra show the greatest changes as shown in Figure 26.

Five lift-off levels, which are 200 mm, 220 mm, 240 mm, 260 mm, and 280 mm, were simulated in the test rig model. The conductivity of the saline was 13 Sm^{-1}. In the simulations, the model used a coil array that consists of 8 coils which is shown in Figure 25. The signals of the coupling of two coil pairs were analysed. The simulated readings were also normalised against their empty space values and plotted in Figure 26.
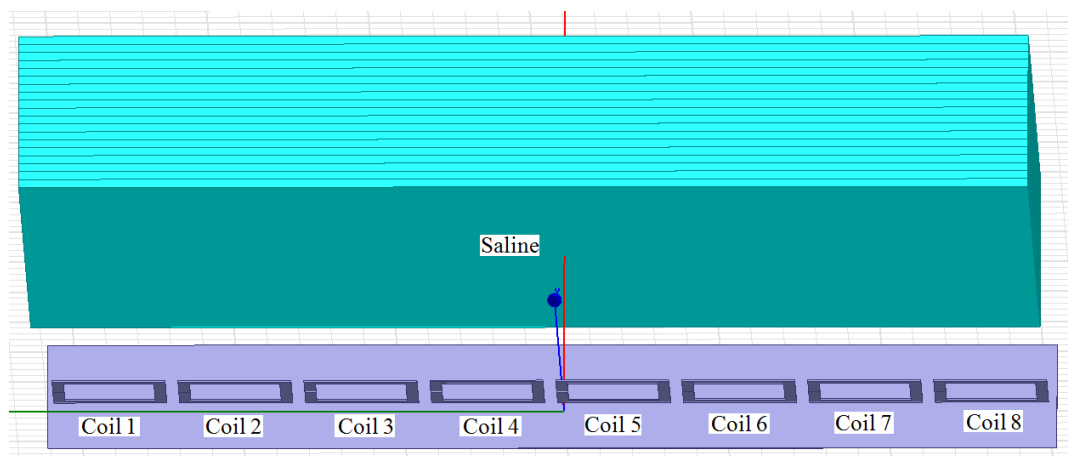
Figure 25 Planar coil array setup in simulation

(a)
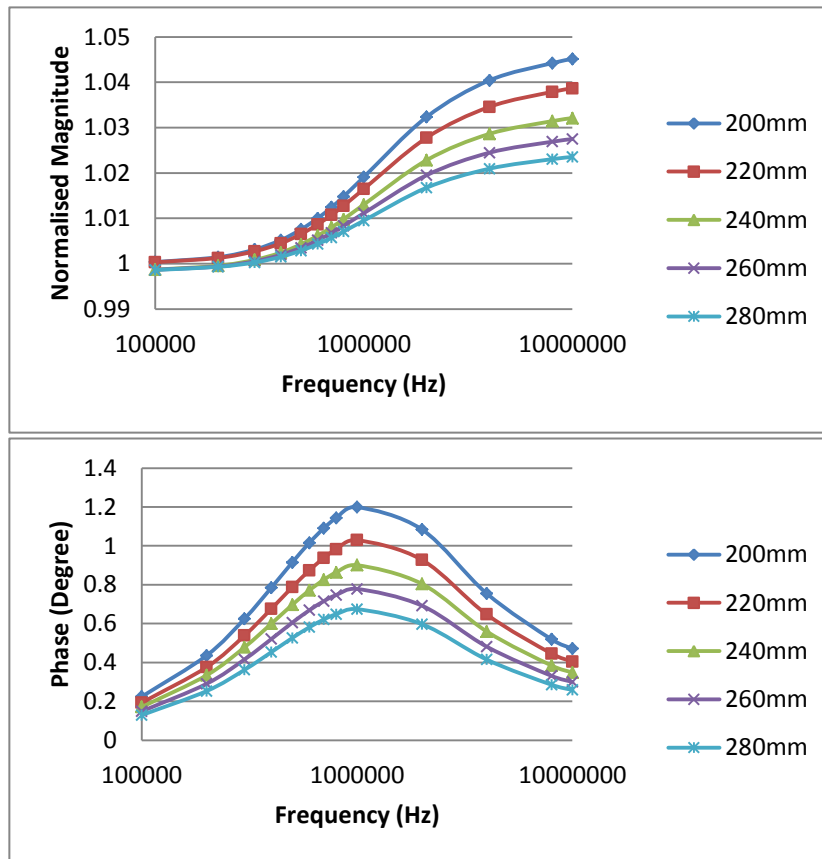
(b)
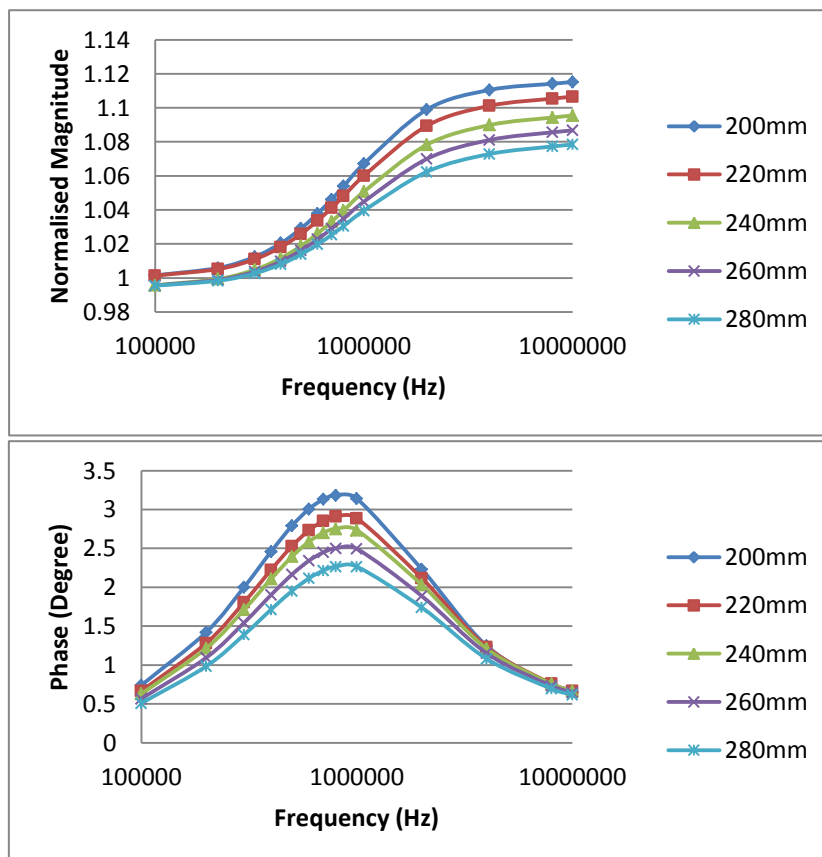
Figure 26 Normalised magnitude and phase changes with respect to frequencies for lift-off levels of 200 mm, 220 mm, 240 mm, 260 mm and 280 mm (a) coil-14 (b) coil-17

On the graphs in Figure 26, coil 1 is the transmitter and coil 4 and 7 are the receivers. In order for a simpler indication of coil pairs in the future, abbreviation will be used. The shortened form will be coil-"tx""rx", where "tx" represents the transmitting coil and "rx" represents the receiving coil. Hence, the two coil pairs in this analysis used will be coil-14 and coil-17. The distances from the coil centre for these two coil pairs are 234 mm and 468 mm respectively.

By observing the trend of the phase signals for the five lift-off setups across frequencies, the phase signals have a peak value at a frequency of approximately 1 MHz. Then, as the frequency increases, the phase signals decrease slowly. This indicates that the saline setup has the most sensitive response around a frequency of 1 MHz. However, as higher frequencies are approached, in this case, 10 MHz, the phase detected by coil-17 overlaps with each other for five of the lift-off setups. Similar trends are also shown in coil-14 plots. Therefore, a single frequency method is not ideal as the reading obtained will sometimes be confusing, providing the wrong lift-off levels by just depending on a single normalised magnitude reading.

4.5   Conductivity Sensitivity

The behaviour of the system towards the change of conductivity is studied in this section. This study is important because the temperature of the molten glass changes as the melt moves along the furnace. The temperature directly affects the conductivity of the molten glass, which is the key conducting material concerned in this research. As shown in the Figure 7 in Chapter 2, the temperature of the melt changes according to its depth, hence, it is a challenge to verify the exact conductivity of the melt above the sensor since different level of depth of the molten glass has different conductivities.
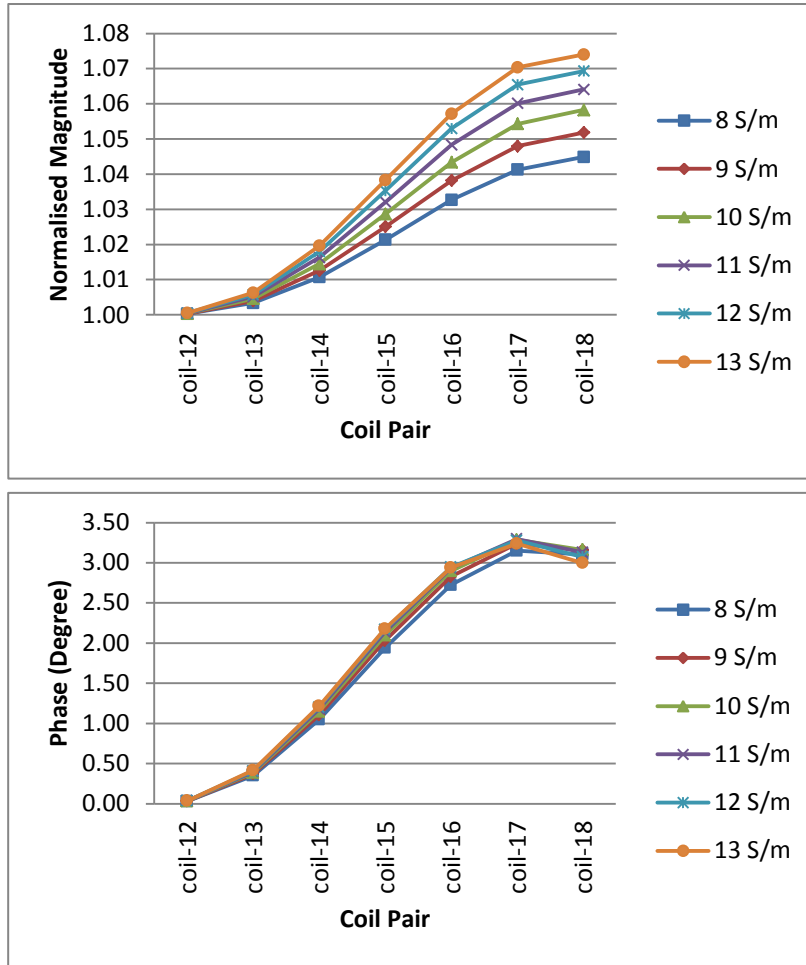
Figure 27 Effect of conductivities variation in magnitude and phase at 1 MHz

To simulate the effect of the electrical conductivity of the saline / molten glass, the conductivity of the saline in the test rig model was modelled with values of 8 to 13 Sm^{-1}, in 1 Sm^{-1} steps. In Figure 27, the normalised magnitude and phase are plotted separately with respect to the increase in distance of the coil pairs with coil 1 as the transmitting coil. The coil centre distance of transmitting coil to receiver coil has a 78 mm increment subsequently from coil-12 to coil-18. The lift-off between the sensor and the saline in this setup is 324 mm.

As shown in the magnitude and phase graphs, the coil pair with the nearest distance; i.e. coil-12 gives a very small signal for all the conductivities, with normalised magnitudes of almost 1.00 and a phase angle of almost 0. Therefore, the nearest distance coil pair measurements (i.e. coil-12, coil-23, coil-34 etc) will be ignored in all future simulations and experimental results in this thesis.

The normalised magnitude graph clearly indicates that by increasing the conductivity, the magnitude is also increased too. However, the effect of the conductivities change is not significant with phase angle, which has the advantage of being almost insensitive to the saline conductivity over this range.

4.6   Effects of Steel Beams Position

Steel beams are used as the supporting base of the furnace structure and therefore, their position is required in the FEM models. However, it is sometimes difficult to measure the exact dimensions of the steel beams as the distances between beams vary for each location under the same furnace. Measurement of the exact geometry of the steel requires the exposure of the technical staff to heat for a long period. Hence, it is important to evaluate the effects of steels distances on the signals in order to determine the required accuracy for these dimensions.

4.6.1   U Beams

The U beams are the nearest supporting members to the bottom of the furnace and consequently these are also harder to obtain the exact dimensions due to the hot environment. Hence, the chances of having errors in these measurements are higher. Simulations were carried out by moving one of the U beams to the left with increments of 10 mm each time to a maximum of 30 mm, which increases the distances of the original beams distance from 390 mm to 420 mm. The same setup was carried out moving the beams to the right, decreasing the distances of two beams from 390 mm to 360 mm in 10 mm steps. The test rig geometry is used in this simulation. An arrow indicating the movement of the U beam is shown below.

Figure 28 Position and the directions of movements of the U Beams
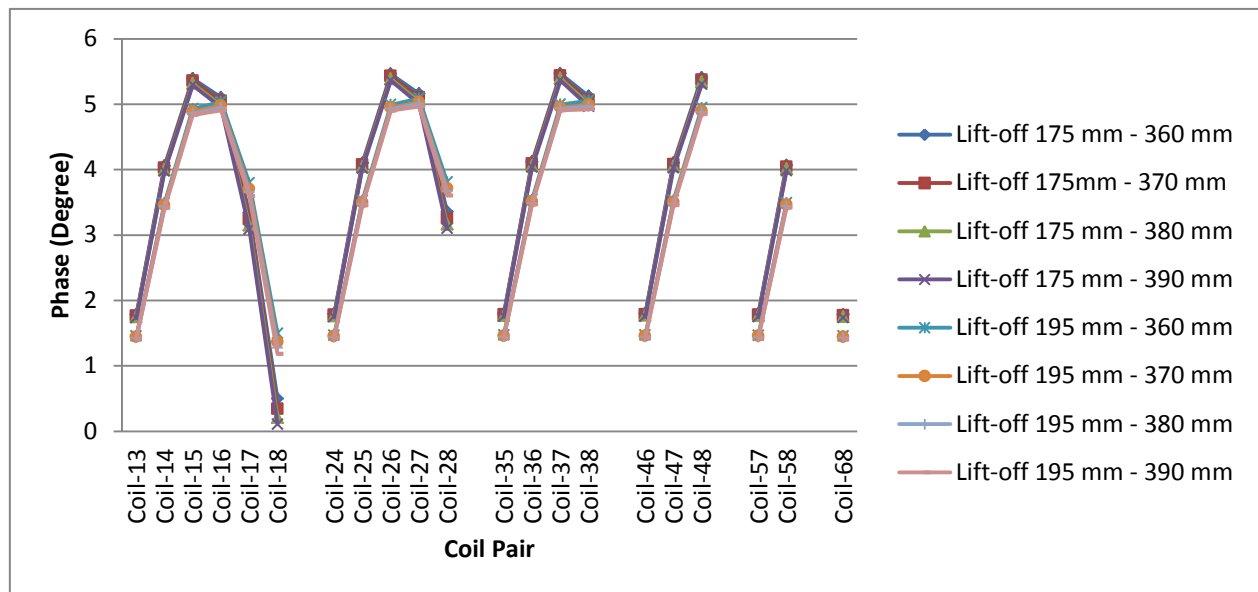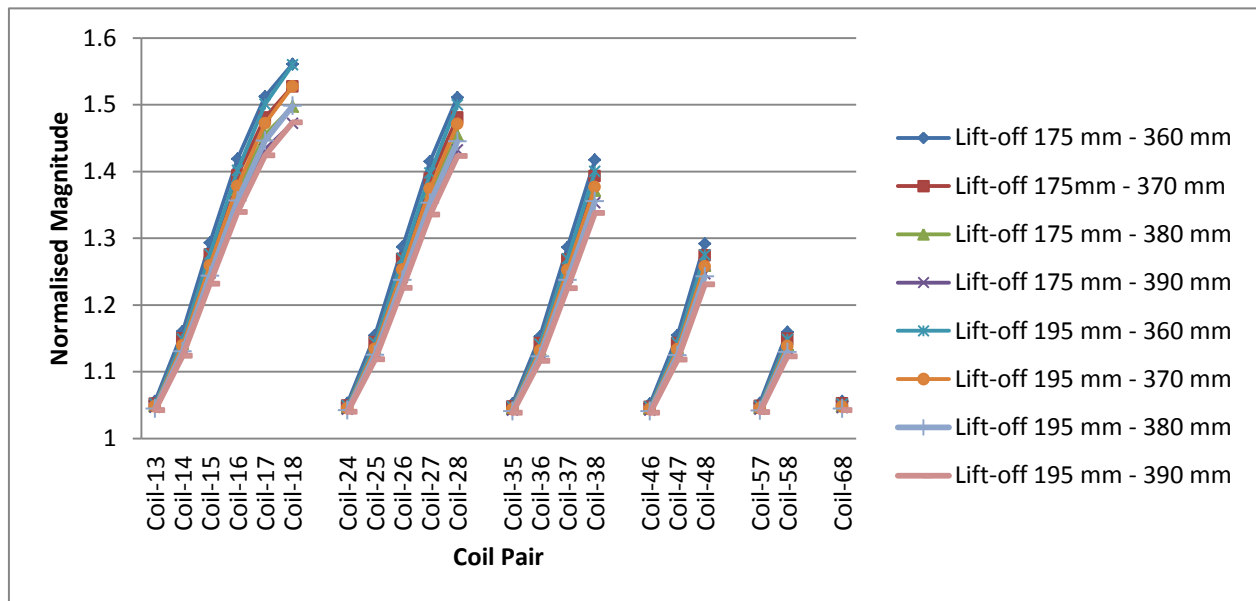
Figure 29 Effects of decreasing the distance between U beams in normalised magnitude and phase from the original distance of 390 mm with lift-off 175 mm and 195 mm
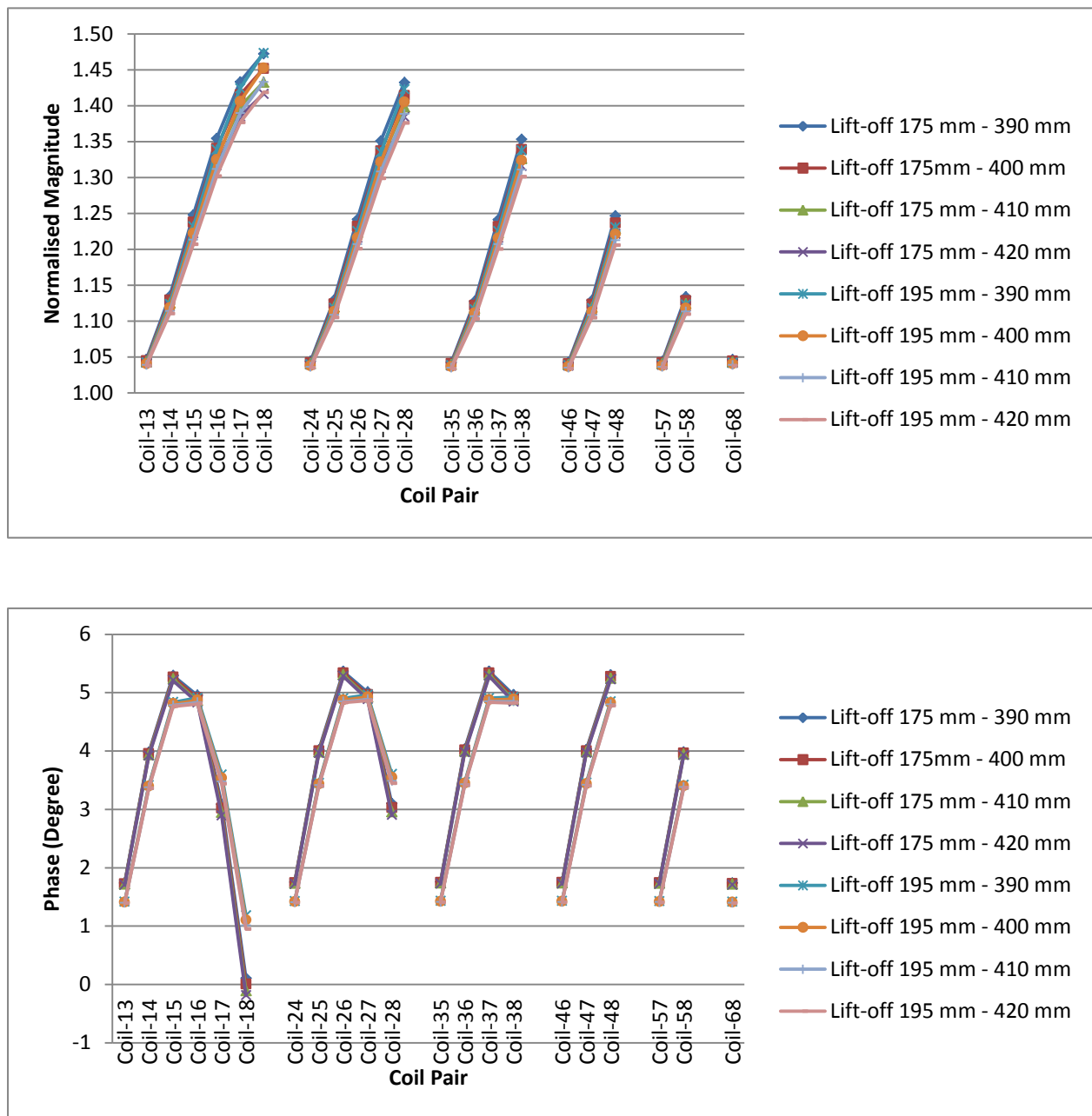
Figure 30 Effects of increasing the distance between U beams in normalised magnitude and phase from the original distance of 390 mm with lift-off 175 mm and 195 mm

Normalised magnitude and phase graphs are plotted in Figure 29 and Figure 30 for the decrease and increase of U beams distances for test rig model. The effect is observed for the signals across all coil pairs in the system apart from the neighbouring coil pairs. The conductivity in the test rig saline was set to be 14 Sm^{-1} and the frequency was 1 MHz.

The normalised magnitude plots show that the changes in the positions of the steel U beams do significantly affect the signal obtained. As the distance of the beams is increased, the normalised magnitude values decrease. To compare the relative sensitivity of the U beam distances to the signals obtain by varying the lift-off levels, two further sets of simulation were also carried out with lift-offs of 175 mm and 195 mm. As shown in both Figure 29 and Figure 30, varying the lift-off levels by 20 mm do not cause a noticeable change in the normalised magnitude signals; the curves almost overlap each other. It is noticeable that the normalised magnitude is affected much more by the variation in the beam distances and less by changes in the lift-off levels.

In contrast to the previous discussion, the phase angle response is seen to be affected less by positional variation in the steel beams and much more by changes in lift-off to the saline, which is evidenced by a constant phase angle response with steel beam distance, but a clear results for the 20 mm lift-off change.

4.6.2   I Beams

The steel I beams provide a supporting foundation for complete the furnace and as such are positioned underneath the U beams considered in the previous section. Consequently, the I beams are further away from the glass. A similar process was used to study the effects of the I beams as followed previously for the U beams. Simulations were carried out by moving the steel beams from the original position of 785 mm between two beams by decreasing the distance gradually to 755 mm and increasing the distance gradually from 785 to 815mm in steps of 10 mm. Figure 31 illustrates this process and an arrow shows the location of the I beams and the direction of the movement of the beam in the simulations.

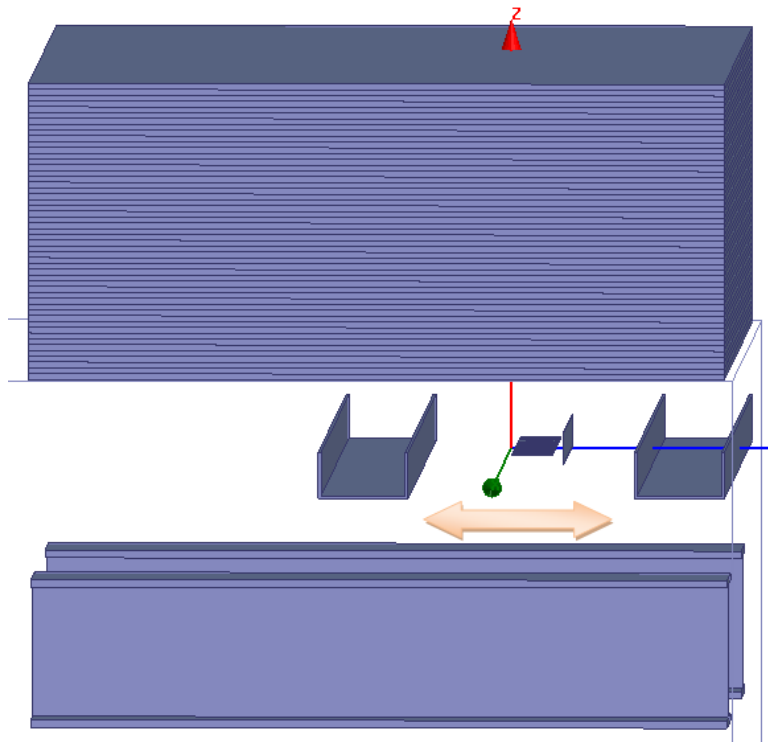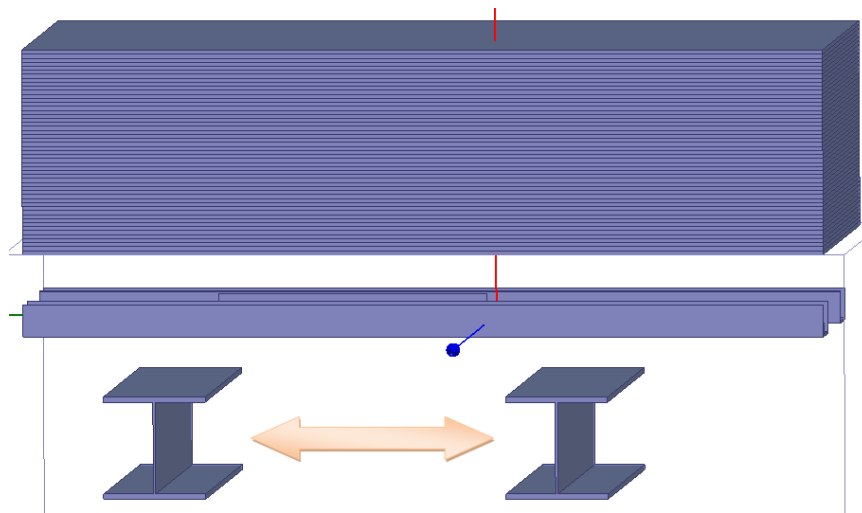**Figure 31 Position and the directions of movements of the I Beams**
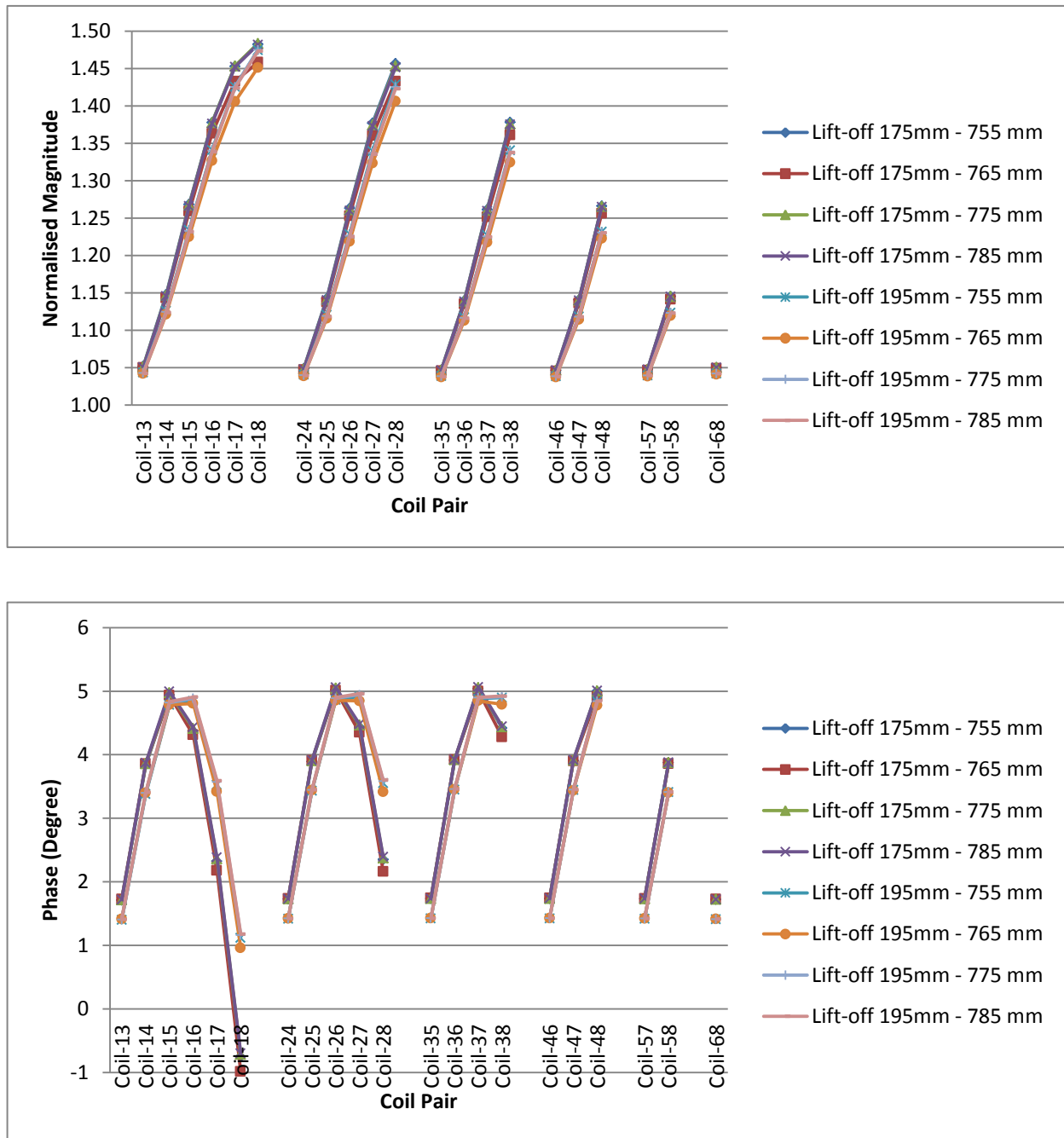
Figure 32 Effects of decreasing the distance between I beam from the original distance of 785 mm in normalised magnitude and phase with lift-off 175 mm and 195 mm
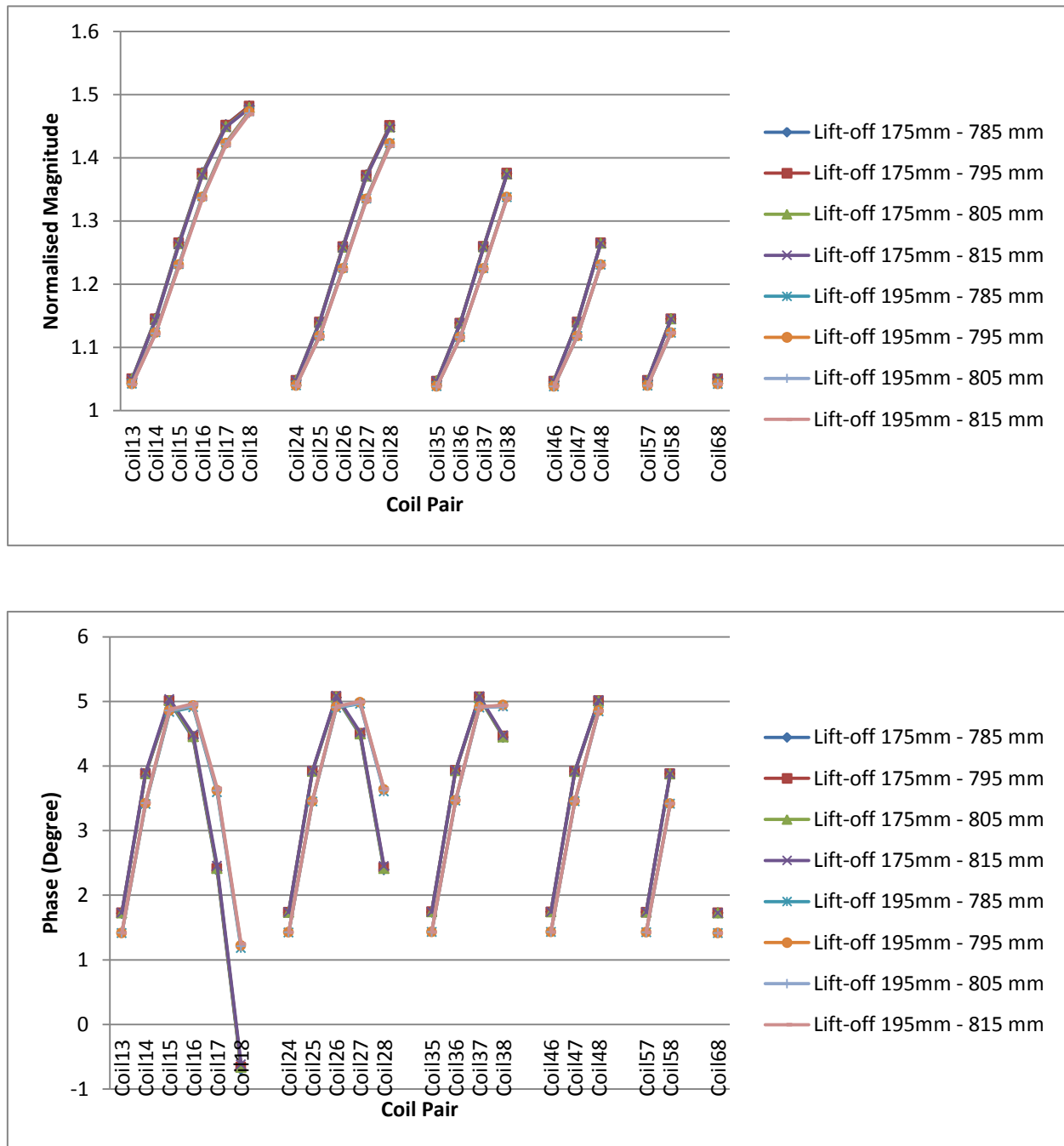
Figure 33 Effects of increasing the distance between I beam from the original distance of 785 mm in normalised magnitude and phase with lift-off 175 mm and 195 mm

Figure 32 and Figure 33 plot the effects of the coupling against the position of the steel I beam, showing both the normalised magnitude and phase change. Comparing both of the magnitude graphs for the decreasing and increasing distances between the I beams, as the distance becomes closer for the I beams, the change in magnitude signal becomes more apparent. When the I beams are moved further apart, the effect on the responses are much less. This is shown in Figure 33, the magnitude signals almost overlap with each other regardless of the distances of the I beams, and it is affected more by the lift-off change, giving a distinct signal trends for two lift-offs. This effect indicates that as the steels are closer, the influence of the steel towards the magnitude signal of the saline is more significant as it deforms the field of the magnetic coupling between the coils.

Similar effects to those seen previously also apply to the phase angle. The change in phase as the results of the steel distance variation is barely noticeable at coil-16 when the distance of the I beams are moved closer together from 785 mm to 755 mm. As the I beams are further apart, clean overlapped signals for the steel distance variations is shown in Figure 33, showing a clear signal trend for two lift-off levels.

By changing the lift-off from 175 mm to 195 mm, with distance between beams of 785mm, the difference in signal between two lift-off levels for coil-17 from is more than 1 degree. Comparing with the same lift-off of 195 mm, by varying the distances between the beams from 755mm to 815mm, the difference in the change in phase signal is only about 0.1 degree. The results are reasonable as the further the steel is from the glass, the lesser the influence on the signal. From the simulations, it can be concluded that the steel positions does influence the signals. However, for the I beams positions, it is consider less important because the effects on the signals are smaller.

4.7   Steel with Boundary Impedance

When analyzing the electromagnetic phenomena on the glass furnace, steel beams were included; however, the high frequency causes difficulties in the analysis due to the strong skin effect. With high frequency, the skin depth, δ, tends to be near zero and the eddy current flow is virtually confined to the surface of the conductor. In the limit case, the eddy currents

flow in an infinitely thin surface layer which serves as a screen towards the magnetic field penetration into the interior body of the material [104]. In [1], the measurement of glass furnace has been modelled, but the steel structure was assumed to be a perfect electrical conductor (infinite electrical conductivity) which is an approximation of the practical case. To observe the influence of the steel with real properties which include the permeability and conductivity, an impedance boundary was used for the represent of all the steel beams. This enables a more practical case to be simulated and analysed. The same simulation as moving the U beam distances as Section 4.6.1 was carried out in order to analyse the influence of the material chosen for steel.

The impedance boundary offers an efficient method of simulation because the body of the steel is not included in the solution and therefore does not need to be meshed. Various numerical and analytical solutions to use the impedance boundary conditions for solving eddy current problems were contributed. The classical expression for impedance boundary conditions can be found in [105]. This uses an infinite conducting half plane to obtain the expression for the linear and nonlinear problems. When the magnitude of penetration depth of penetration is limited, the equation of the 3D diffusion of the electromagnetic field into the object will be substituted with 1-D equation. This method gives a solution for a one dimensional system, which has the infinite extent in the y- and z-directions. However, it does not provide a solution for the surface of the conductor that has sharp corner and edges. This proposed technique is not realistic as it has an assumption that the conductor has to be a smooth surface and it is not possible for use with complicated geometries. An overview of the problems of the classical method in solving eddy current problems with impedance boundaries is discussed in [106] and the solutions on the edges and the corners of the geometry were proposed by the same author in [107] . An analytical solution is used for the electric field in [108] and the 2D implementation on the edges was presented. In [109], the author has made a contribution in finding solutions in extending the boundary condition towards the corners, which proposes an expression which relate the tangential electric and magnetic fields, on the surface of conducting media under a.c. excitation, along both 90 degree edges in 3-D conducting media, and at full 90 degree corners. The approach of using the impedance boundary condition is further taken into solving the 3D problem with finite element solution by [110].

Due to the complicated steel structures under the furnace, the numerical software Maxwell$^{®}$ is being used to solve the problem. Assuming that the steel is a low carbon steel with the properties of conductivity, σ = 1.1 x 10^6 Sm^{-1} and permeability, μ_r = 100. The skin depth will be 4.8 μm at a frequency of 1 MHz.

As the magnitude of the system has higher sensitivity of the steel beam's positions and provide insignificant changes towards the glass distance that representing the thickness of the furnace wall, the magnitude of the system is not compared in this analysis. Four U beams distances with the first six coil pairs phase values are shown in Table 4 for comparison. A table is used as the changes in the value between perfect electrical conductors and low carbon steel is too small to be observed in graphs, i.e. the third decimal place in the values. The values of the steel as low carbon steel is smaller compared to the perfect conductor.

(U Beams Distance) Material	Coil13	Coil14	Coil15	Coil16	Coil17	Coil18
(360mm)						
Low Carbon Steel	1.4517862	3.4808962	4.9191387	5.0244088	3.7835279	1.4828637
Superconductor	1.4532804	3.4863461	4.9278424	5.0362244	3.7957838	1.4930111
(380mm)						
Low Carbon Steel	1.4232326	3.4280519	4.8526681	4.9330076	3.6380445	1.2592475
Superconductor	1.4228952	3.4303993	4.8597736	4.9448935	3.6534956	1.2753707
(400mm)						
Low Carbon Steel	1.4033583	3.3916305	4.8079662	4.8694476	3.5333723	1.0965715
Superconductor	1.4034364	3.3918106	4.8082701	4.8699736	3.5349192	1.0990006
(420mm)						
Low Carbon Steel	1.3888279	3.3600909	4.7634831	4.8056347	3.4333515	0.942232
Superconductor	1.3889113	3.3605578	4.7643398	4.8084266	3.4372539	0.9485526

Table 4 Comparison of low carbon steel and superconductor as material in U beam distances effect

Although the differences of values are small for perfect electrical conductors and low carbon steel, it has enabled future simulation to be more realistic by having the actual steel material with an appropriate impedance boundary, avoiding the assumption that the steel is a superconductor.

4.8   Conclusion

In this chapter, finite element electromagnetic models of the furnace were developed in order to assess the effects of the steel support structure on the sensor response. The models created have the flexibility of setting the molten glass in layers, which represents the distance of the molten glass from the sensor. This method will be used in all the future simulations in this research as it allows the same mesh geometry to be used for all the models to reduce simulation errors. However, the down side of this method is that it assumes that the corrosion of the furnace is evenly distributed. One of the solutions for this method to be used is to measure several locations to produce a furnace wall thickness curve around the area.

Several simulations were carried out in this chapter such as the frequency response, the conductivity response, and the effect of using real steel properties in the simulations. This is able to provide a guideline in choosing the frequency for the system to be used in the experiments, understand the influence of the temperature and conductivity towards the measurement, and also able to understand the different accuracy in calculations by using the real steel properties instead of a perfect electrical conductor.

The analysis has shown that for phase and magnitude, the U beam has introduced a stronger influence to both of the signals. However, it is clearly shown that the phase is very stable and much more sensitive towards the lift-off change instead of the beams movement. The magnitude of the signal is affected significantly with the movement of the beams compared to the lift-off changes. Therefore, to utilise the results of the magnitude signal, it would require a very precise dimensions of the supporting structure of the furnace in order for the simulation results to be accurate.

Chapter 5 System Hardware

5.1   Introduction

The sensor system must be able to operate continuously in a stable manner in high ambient temperatures. The system is separated into two parts where one part contains the sensor head that has to be directly in contact with the refractory surfaces with high temperature, which is up to 500 ^{o}C. The second part can be located and operated at approximately 2 - 3 metre under the furnace, where the hot air emitted from the furnace is trapped and the ambient temperature is maintained at about 50-70 ^{o}C. During operation, the system may be subject to temperature variations, which can cause signal drift; hence, it is important that the system is able to produce repeatable signals.

The system is also intended to be a long term measuring tool which may be used at different positions under the furnace. Therefore the system has to be robust to the change of the environmental exposure and movement between locations around the furnace. In order for the ease of relocation, the equipment has to be designed in a size and weight such that it is reasonable portable and easily set up. Also, the system has to be designed in reasonable costs which would be beneficial to the glass making industry.

The typical conductivity of the molten glass is below 15 Sm^{-1}, which is very low compared to the conductivity of the metals. As discussed in the previous chapter, the proposed frequency range from 500 kHz to 10 MHz will be used for the system.

As will be described in this chapter, three different iterations were used to design the sensor system, as follows:

i.   The first sensor was designed to be flexible and contained plug-in electronics boards. The idea of this design was for the ease of modification of the electronics.
ii. The second design of the electronics had a simpler construction and a lighter weight.
iii. The third design was a near commercial prototype which is lightweight and portable, requiring less man power for operation.

5.2   System Description

The sensor system consists of four parts, which are the sensor, the front end electronics, the data acquisition system and the host computer. A schematic of the system is shown in Figure 34. The main components of the system are described in more detail in the following sections.
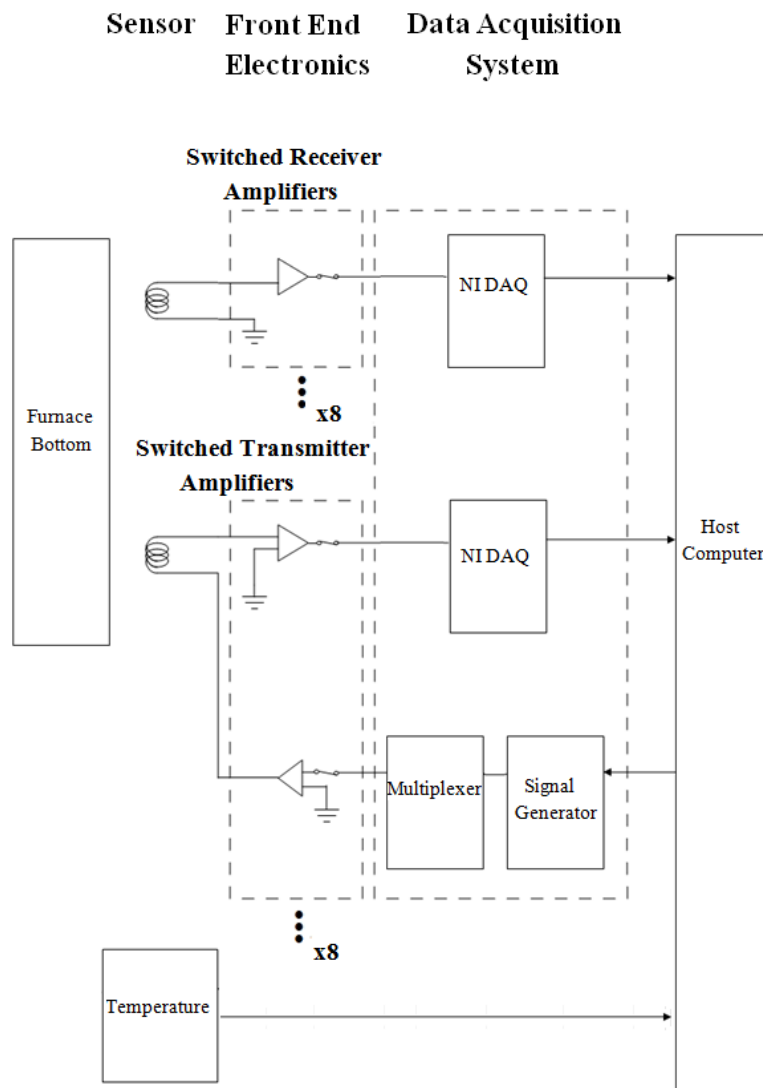
Figure 34 Schematic of the eddy current inspection system

5.2.1 Sensor

There are four elements in the sensor; the sensing space, the excitation coils, the detection coils and the electrostatic shield. The sensing space is the area of interest where the furnace is located. The excitation coils produce the 'primary' magnetic field and the detection coil detects the secondary field produced by the liquid glass in the furnace. The electrostatic shield is used to prevent external interference from capacitance coupling between the sample and the coils.

5.2.2 Coils

In order to obtain sufficient of spatial data, the excitation and receiving coils were separated at different distances; hence, a coil array was employed. Flame retardant 4 (FR4) is a fibreglass reinforced epoxy laminate that is primarily used as the material for printed circuit board (PCB) production. FR4 is flame retardant and its ability to withstand temperatures up to 150 ^{o}C makes it suitable for the use as the coil material. FR4 is also lightweight and easy to etch multiple coils on the board to create a multi-coil array. This is able to increase the inspection coverage area as well as reducing the operation time without having to relocate the coils sensor at different locations for measurement.

Successful implementations were found using planar rectangular spiral coils [111-114]. Identical coils could also be made by duplicating the pattern of the original coil design. In order to utilise the limited space available for measurement, the excitation coils and the receiving coils were constructed on a double sided PCB board. This enabled the exciting coils and receiving coils to be printed on each side of the board. The number of turns was considered based on the compromise between the pick up ability of the receiving coil and the maximum available driving current for the transmitting coil.

To obtain more independent spatial data and supply as high magnetic field as possible, 8 square coil pairs with individual size of 70 mm x 70 mm were used. The separation between the individual coils on the same layer was 8 mm.
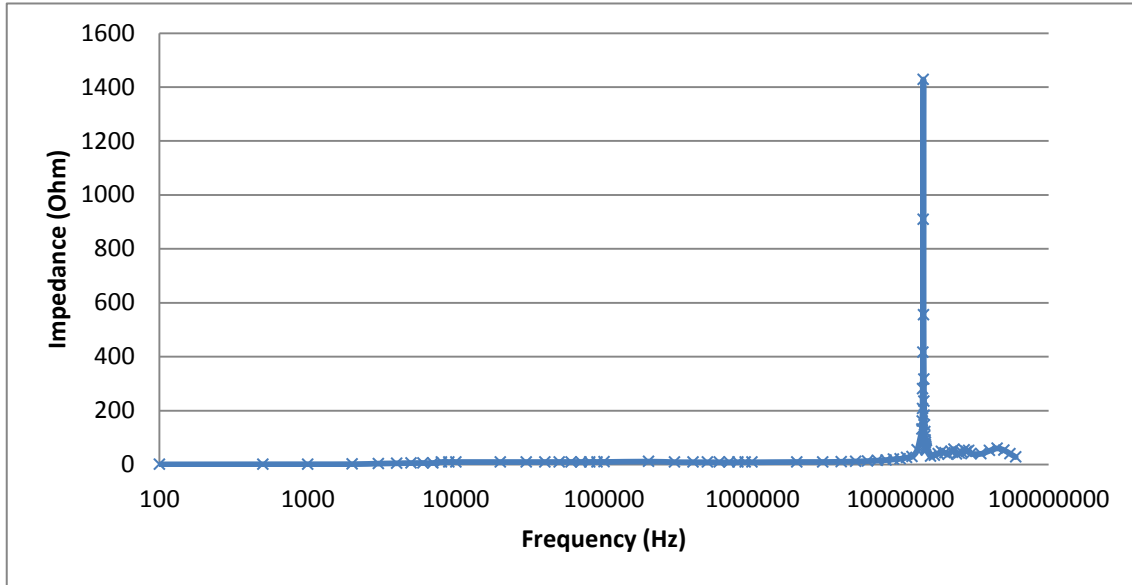
Figure 35 Resonance frequency of an excitation coil

Figure 35 shows the impedance magnitude of the transmitter coil range from 100 Hz to 60 MHz. From the graph, it can be seen that the magnitude stays at similar level from 100 Hz to 12 MHz. Then there is a striking increment and peak at the frequency of 14 MHz. The magnitude drops after the peak value. This indicates that the resonant frequency of the coil is 14 MHz. The current system uses the frequency range 500 kHz to 10 MHz; hence, it does not overlap with the resonant frequency of the coil. Figure 36 shows photographs of the transmitter and receiver coil geometries.
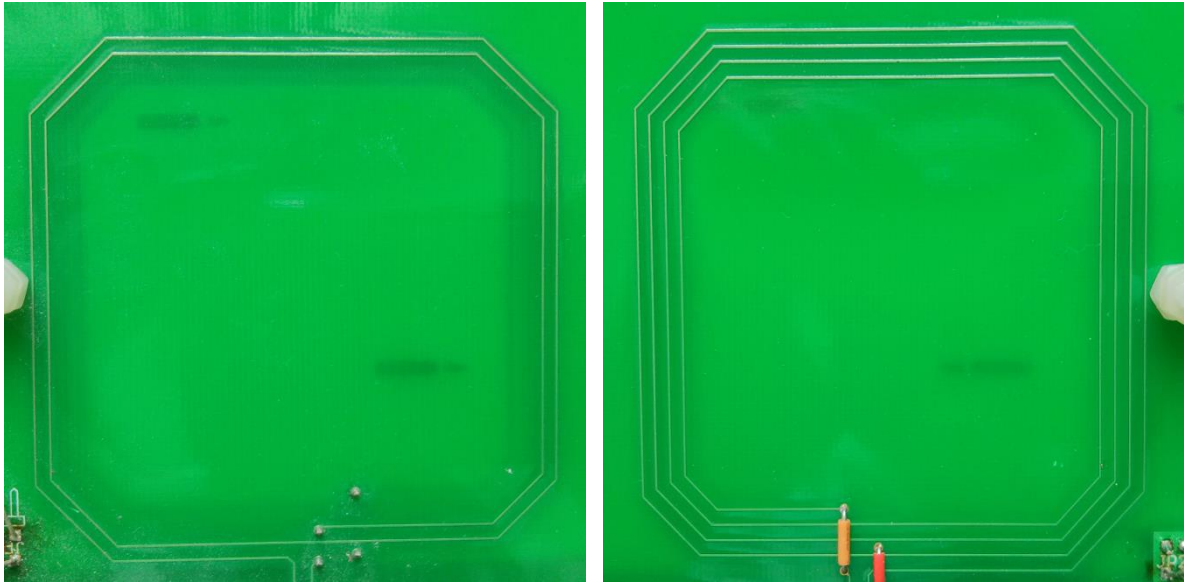
(a)   (b)

Figure 36 PCB coil used as (a) excitation coil and (b) receiver coil

5.2.3   Shielding

Coil shielding, also known as screening, is often used to avoid capacitive coupling between the coils with the sensing object and improves the signal-to-noise ratio of the input circuitry by decreasing the interference from the outer environment. Shielding also helps to keep the external fields outside the sensor array and confines the internal fields inside [115]. Several mechanisms associated with capacitive coupling were discussed in [116]. In the system in [102], a shield with radial PCB lines is used. The printed copper strips shield is connected to a common ground to ensure that no induced eddy current forms in the circular loop, as this may cause disturbance towards the measurements.

For samples that are with low conductivity, the capacitive coupling contributes only a small contamination towards the measurements even with the individual coils unscreened [117]. However, this is only applicable to sample that are below 0.5 Sm^{-1}. Since molten glass is in a higher range of conductivity, a carefully designed shield is required in order to prevent the superimposition of unwanted signals on the true measurement signals.

86

In [102], capacitive coupling for the real and imaginary components were observed for coils with two different types of screen; star and circle shielding. Although the most reliable design of shield is still uncertain, a comb screen design was chosen in this project as it has shown many successful applications. The distance from the coil to the screen is 10 mm. A method to test if the capacitive coupling had a strong effect towards the measurements was to observe the change in signal by placing a non-conducting material, e.g. deionised water (0 Sm^{-1}) in the sensing space. This test was carried out with tap water with the conductivity of 0.012 S/m and the effect of the tap water falls in the noise level was observed, hence, it was negligible.

For the sensor of the system, it contains 3 layers of PCBs with the top and bottom layers as the screens and the coils sandwiched in the centre.
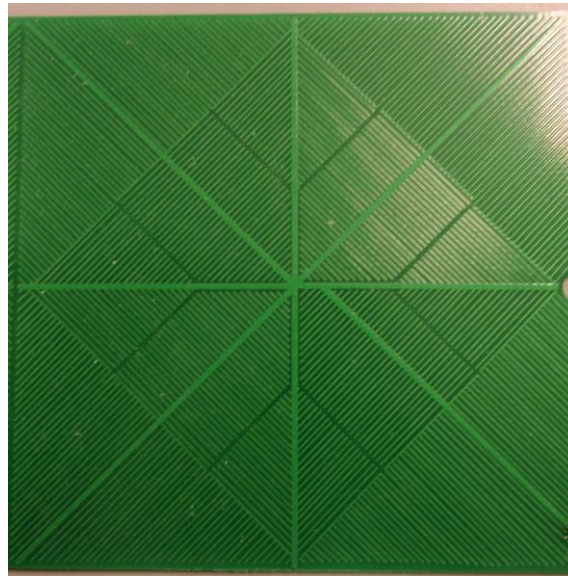
Figure 37 Electrostatic screen for single coil in comb design

5.2.4   Front End Electronics

The front end electronics are responsible for supplying the drive signals to the excitation coils, amplifying the received signals from the receiver coils and multiplexing these signals to the NI Data Acquisition System. Figure 38 shows the equivalent circuit of a source receiver pair of coils with a current driven excitation coil, with current i_1. M_{ij} denotes the mutual inductance between coil i and j. The resistance and capacitance is included in the figure as the equivalent permittivity and capacitive coupling contain in the target object in reality.
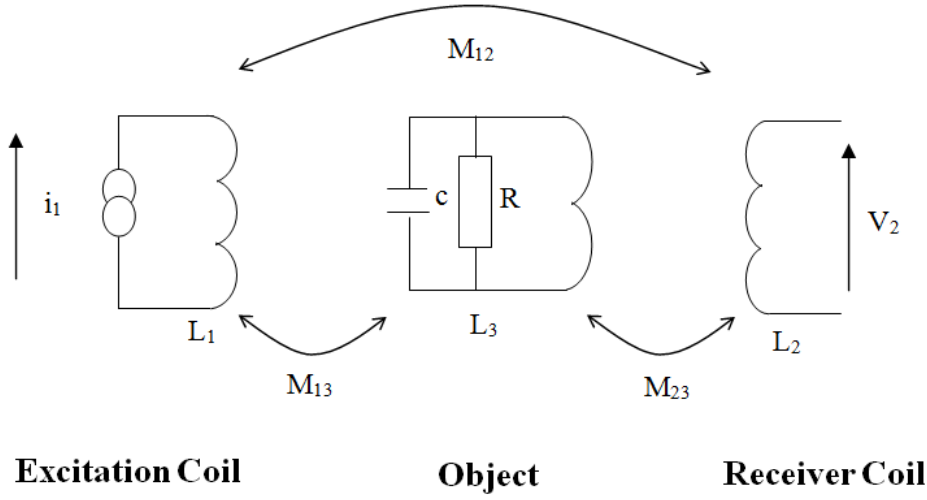
Figure 38 Equivalent schematic diagram for the inductive measuring set-up

In the absence of the object, the voltage induced in the network is

$$v_2 = j\omega M_{12} \cdot i_1$$

<div align="right">**Equation 31**</div>

Rearranging the equation, the mutual inductance between coils is

$$M_{12} = \frac{v_2}{j\omega \cdot i_1}$$

<div align="right">**Equation 32**</div>

With the presence of the target object, the voltage on the receiver coil is express as follow [34]

$$v_2 = \left[\omega M_{13} M_{23}\left(\frac{1}{R} + j\omega c\right) + jM_{12}\right] \cdot \omega \cdot i_1$$

<div align="right">**Equation 33**</div>

By comparing with the mutual inductance coupling system as shown in Figure 38, the equivalent diagram of a single primary and secondary coil pair with the acquisition front-end system is shown in Figure 39.
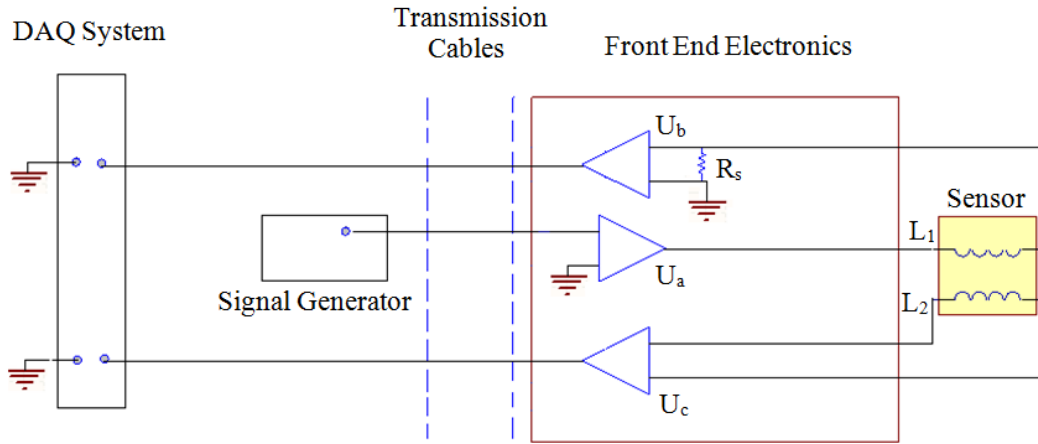
Figure 39 Mutual inductance coupling for a single coil pair [1]

To boost the excitation signal, the signal generator output is connected to an amplifier, U_a which is connected to one end of the coil. For the other end of the coil, it is connected to a current sensing resistor, R_s which provides a reference signal for the current in the excitation coil. This reference signal will be amplified with another amplifier, U_b. For the receiver, the amplifier U_c is connected from the coil to the PXI system in order to give a reading of the coupled signals.

The equation of the system is correlated with Equation 32, hence, the mutual inductance is

$$M = \frac{v_{L_2}}{j\omega \cdot i_{L_1}}$$ **Equation 34**

where v_{L_2} is the voltage across receiver coil and it is expressed as

$$v_{L_2} = \frac{v_2}{G_c(f)}$$ **Equation 35**

and i_{L_1} is the current measured across the current sensing resistor, R_s for the excitation coil

$$i_{L_1} = \frac{v_1}{R_s(f) \cdot G_b(f)}$$ **Equation 36**

where V_2: measured voltages for receiver

V_1: measured voltages for transmitter

$R_S(f)$: resistance of current sensing resistor

$G_b(f)$: transfer functions of amplifier U_b

$G_c(f)$: transfer functions of amplifier U_c

5.2.4.1 Amplifiers

The LT1210 was chosen for the excitation amplifier (U_a); the device has the ability of driving a maximum of 1.1A and has a high bandwidth of 35 MHz. The LT1210 can be operated at junction temperatures up 85 °C and contains a thermal shutdown feature, which makes it as a necessity for the overall electronics to maintain at this temperature or lowers to avoid the thermal shut down of the electronics. Waste heat is produced continuously when the high current is flowing through this amplifier, which is dissipated by attaching heat sink. The amplifier circuit was designed to have a gain of 3. As shown in the schematic diagram in Figure 40, the signal from the function generator is inputted via SMB connector P3 and the excitation coil, U_b is connected at to pin 7 of the power amplifier.
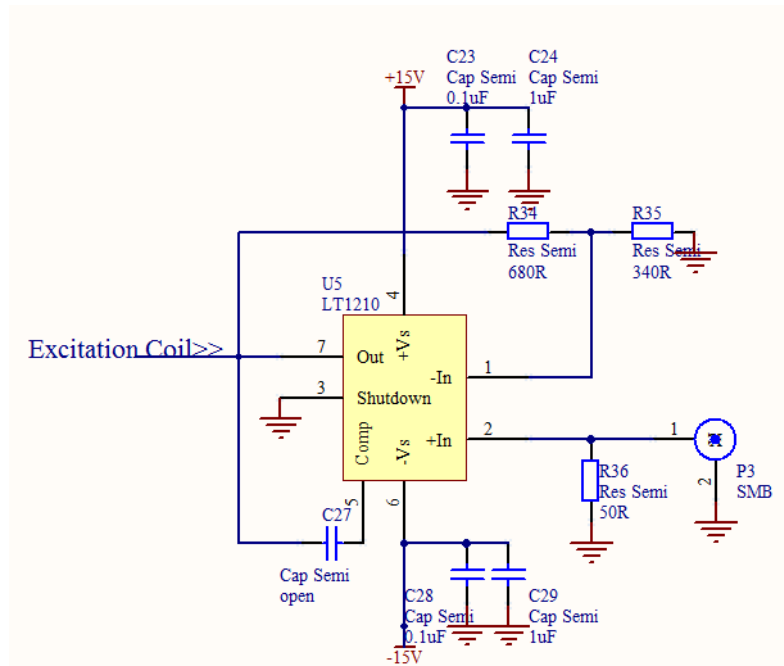
Figure 40 Schematic design of the power amplifier for the excitation signal

For the excitation coil, one end is connected to the output of the power amplifier, and the other end of the coil is connected to the current sensing resistor as shown in Figure 41. In this design, a VCS1625 resistor manufactured by Vishay was used. This low Ohmic resistor is

used to measure the voltage drop across it. The signal will be further monitored by having it passing through amplifying stages. The temperature coefficient of the VCS1625 is 2 ppm/°C with an operation temperature parameter of -55 °C to +125 °C. This resistor is a surface mount device with four terminals and resistance of 0.1 Ohm. The sensing resistor should be a stable component that provides an accurate representation of the current in the transmitting coil. The signal from the current sensing circuit is used to provide a reference to correct for phase and magnitude variations elsewhere in the system. Further discussion will be included for the options of obtaining this reference signal in Section 5.2.4.2.

The current sense signal is then passed to the amplifier, U_b for analysis (see Figure 39). The amplifying stage was designed with two amplifiers connected in series, as shown in Figure 41. The first amplifier requires a high common-mode rejection ratio (CMMR) and it is constructed with an AD8130 from Analog Devices. It has a CMMR of 100 dB at 500 kHz and 70 dB at 10 MHz, which are the upper and lower frequency limit for the current system. The -3 dB bandwidth of the amplifier is at 250 MHz. The gain for the AD8130 stage was set to be 2. The AD8000 was chosen for the second stage of amplification. This is a low noise (e.g. 1.6 nV/√Hz) and high speed device (e.g. 1.5 GHz), which is suitable for driving cables. The AD8000 stage was set to a gain of 10. This is due to the impedance of the 50 Ohm resistor at the output of the circuit together with the 50 Ohm input impedance of the measuring tools have acted as a voltage divider, which halved the gain from 20 to 10. The overall voltage gain for the complete current sensing circuit was also 10.
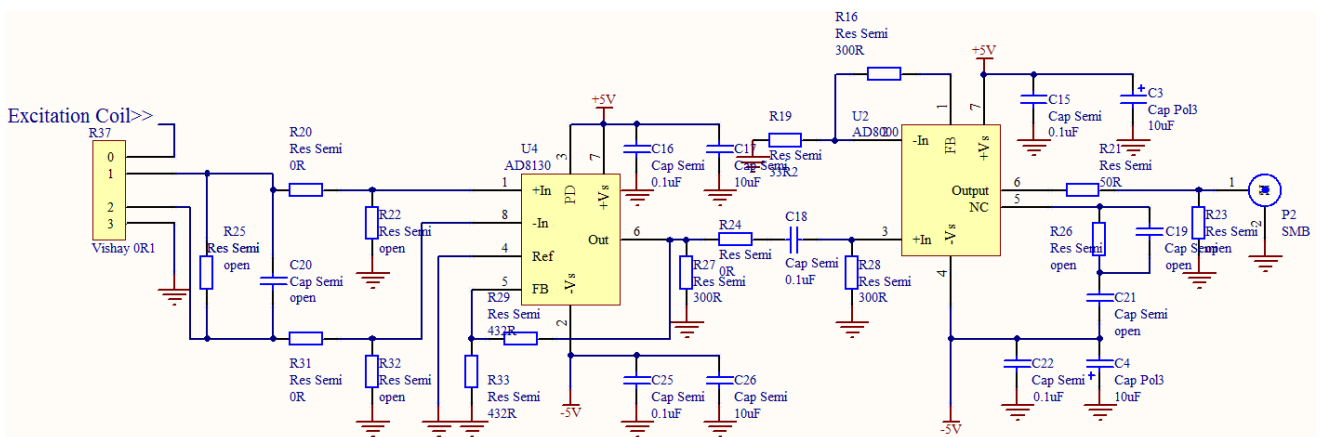
Figure 41 Schematic diagram of current sensing circuit with AD8130 and AD8000 amplifiers

For the signal obtained from the receiving coil (U_c in Figure 39), was passed to an amplifier before outputting to the data acquisition system. The amplifier must be very sensitive to the small signals obtained and have low noise to reduce the measurement error. The requirement for the receiving amplifier is more specific and precise than the transmitter circuitry as the receiving signal is much lower than the transmitting signals. However, in order to obtain the same characteristics for the excitation and receiver circuits two identical circuit will be used. As shown in Figure 42, the only difference for the current sensing circuit with the receiver circuit is the input to the AD8130 amplifier. The signal of the receiver circuit is from the coupled signal from the coil. In Section 5.2.4.1.1, several options of amplifiers and tests are carried out to obtain the suitable electronics for this project.
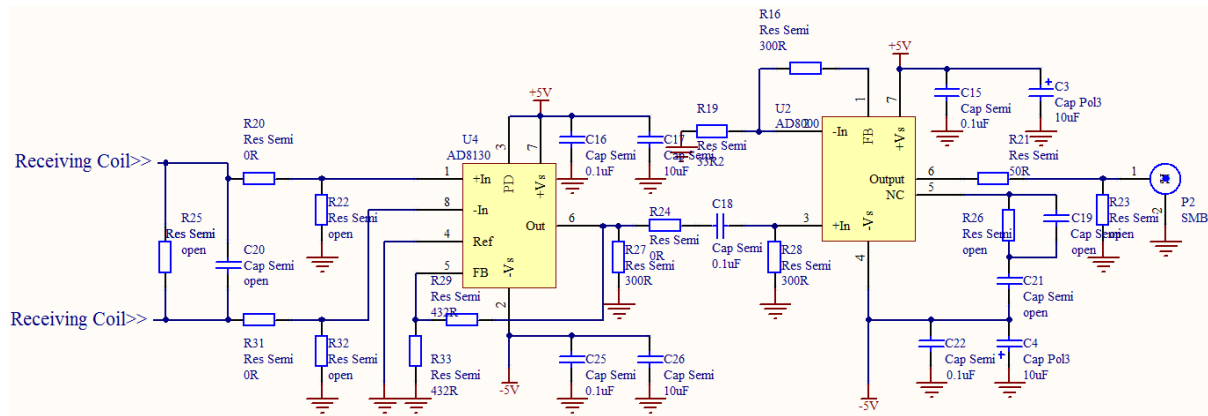
Figure 42 Schematic diagram of receiving circuit with AD8130 and AD8000 amplifiers

Four amplifiers which fulfilled the main criteria were listed into consideration for U_b and U_c. These amplifiers were the AD8129, AD8130, OPA3691 and EL5167. The suitability of these amplifiers including noise performance, the temperature drift and the simplicity of circuitry were assessed. Two options, the AD8000 and AD8099 were selected for the test to be used as the cable driving amplifiers.

5.2.4.1.1 Amplifiers Comparisons

For the first stage of testing, AD8129, AD8130, OPA3691 and EL5167 were soldered individually on a PCB board with the AD8000 as the cable driving amplifier. These four

circuits were constructed with a double sided PCB board. The top layer of the PCB board was used as the component side and the copper tracks for the signals between components, and the bottom layer was used as the tracks for the power signals. A ground plane filled all unused space. The gain for all of these circuits was the same, i.e. 10.

The AD8129 is a low noise, high gain device. The gain was set by the ratio of two resistors R29 and R33 in the schematic diagram in Figure 43. The bandwidth of this amplifier at gain of 10 is 200 MHz with the noise of 4.5 $nV/\sqrt{Hz}$. The minimum gain of this amplifier is 10. With high frequency of 10 MHz, this amplifier enables a high CMRR of 70 dB.

A similar setup and connection was carried out for the AD8130 amplifier (see Figure 42). This amplifier is from the same family as the AD8129. The overall gain of the AD8130 - AD8000 connection was the same as AD8129 – AD8000 connection. However, since the AD8130 amplifier is not able to reach as high gain as AD8129, this stage was set to a gain of 2 for AD8130 then with the gain of 10 for AD8000.
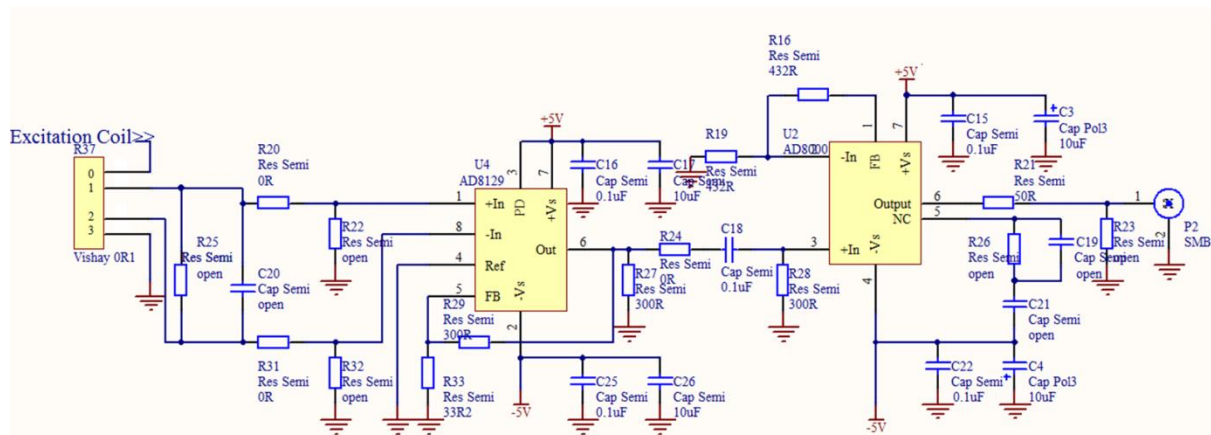
Figure 43 Schematic diagram of current sensing circuit with AD8129 and AD8000 amplifiers

The Texas Instruments OPA3691 must be set for a lower gain in order to provide a higher bandwidth. This disadvantage can be compensated by setting the AD8000 stage with a higher gain of 10. However, this amplifier is a manufactured with three individual operational amplifiers in a package, thus, it has to be connected manually to form a differential amplifier. The typical value for CMRR for this amplifier was 56 dB, which is lower than AD8129. This

amplifier also has the disadvantage of a more complicated circuit layout, which increases the difficulties in troubleshooting and closed loop stability.
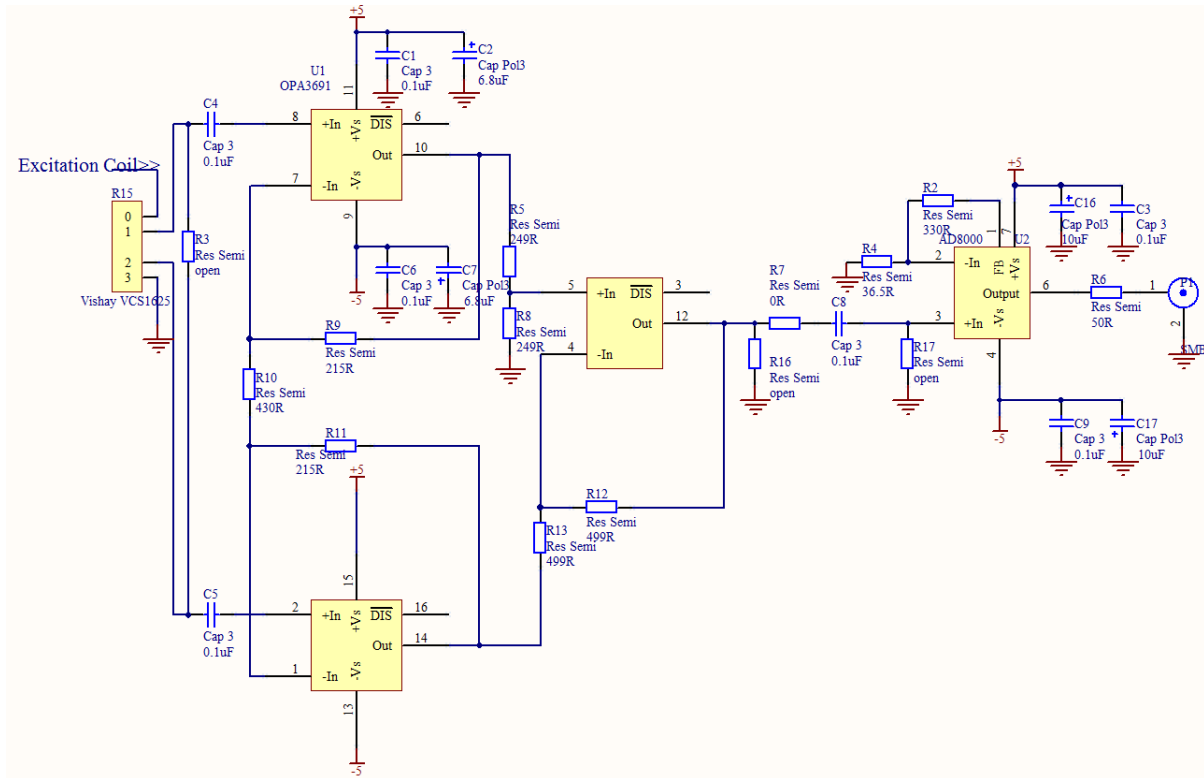
Figure 44 Schematic diagram of current sensing circuit with OPA3691 and AD8000 amplifiers

The fourth selected amplifier was the Intersil EL5167. This amplifier provides the highest bandwidth among three of the amplifiers which is 800 MHz with the gain of 2. The CMRR of this circuit was 57 dB. The design to form a differential amplifier required two operational amplifiers. The individual package of the components has provides more room in the circuit layout designing. However, this leads to more components required in the overall design. As a result, it increases the cost of the components and also will cause the design to be untidy with more tracks.
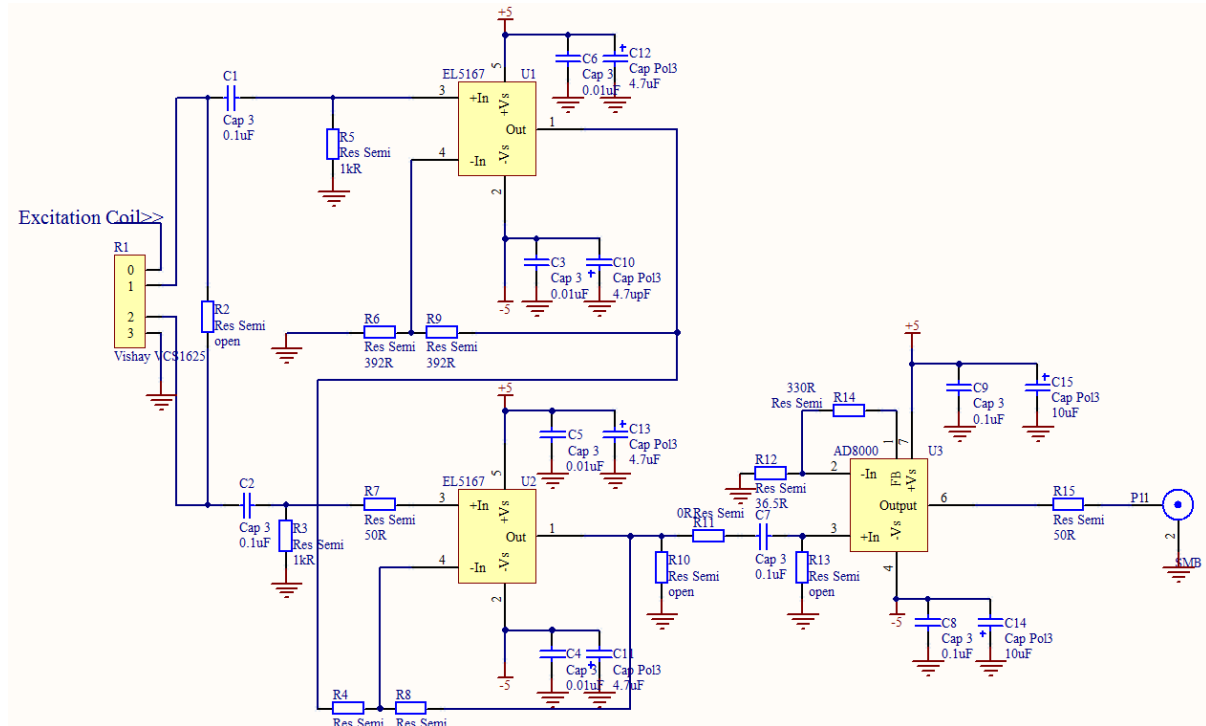
Figure 45 Schematic diagram of current sensing circuit with EL5167 and AD8000 amplifiers

5.2.4.1.2   Thermal Stability

With the consideration of high temperature operation under the furnace, and to ensure the electronics were able to provide repeatable measurements, a temperature drift test was carried out. The equipment used in this testing was a National Instruments data acquisition system (PXI system), a computer with LabVIEW software, a dicast aluminium box with dimensions of 120 mm x 60 mm x 80 mm, a 3.9 Ohm power resistor with 25 Watt rating as a heater, a temperature sensor LM35 (TO-92 plastic package) and a voltmeter.

The 4 PCB boards containing the AD8129, AD8130, OPA3691 and EL5167 circuitry respectively were thermally tested. The temperature sensor was connected to the PXI system to record the effect of the temperature change for each of the amplifiers. The measurements of the deviation of the signal and the temperature change were recorded at the same time. To ensure that the PXI system was sensitive to the temperature changes detected by the sensor, the sensor was synchronised and connected to the multimeter and PXI data acquisition system for the initial calibration.

The thermal stability tests were carried out by heating and cooling the circuitry. The power resistor was used to heat up the dicast box containing the amplifier under test. The experiments were performed with forced heating from the 3.9 Ohm resistor, but free cooling to the ambient. Measurements taken at approximately 2 seconds per reading and the mean of the data over 2000 samples was calculated in order to study the trends of the signal values. The signals obtained are plotted with response to the change of temperature.

For these experiments, these amplifiers were not connected to a receiver coil, but instead, the input signal was fed directly from the signal generator to the amplifiers. The output signal from the amplifiers is compared to the signal from the signal generator by using the LabVIEW program. The change in magnitude and phase, which was the temperature drifts from its original level of reading, was considered. To calculate the drifts, it required the deduction of the reading for the magnitude / phase level with respect to the change of temperature of interest. As the circuit designed are for current sensing purpose, the signal from the signal generator was fed into the connection of pin 1 and 2 in the Vishay resistor.

Although the environment is not directly compatible with the high temperature under the furnace, the experiments were able to approximate the characteristics of amplifiers at temperature below 70 °C. This temperature study gives an indication of the thermal effect of the amplifiers when the compressed air and thermal shield is applied into the system during the experiment, which is used to reduce and maintain the overall operating temperature.
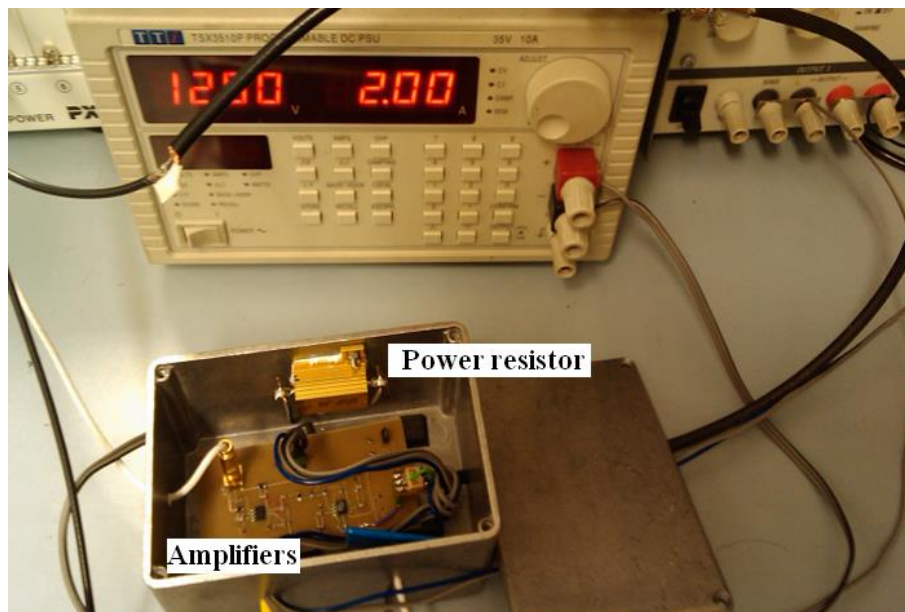
Figure 46 Amplifiers in dicast aluminium box
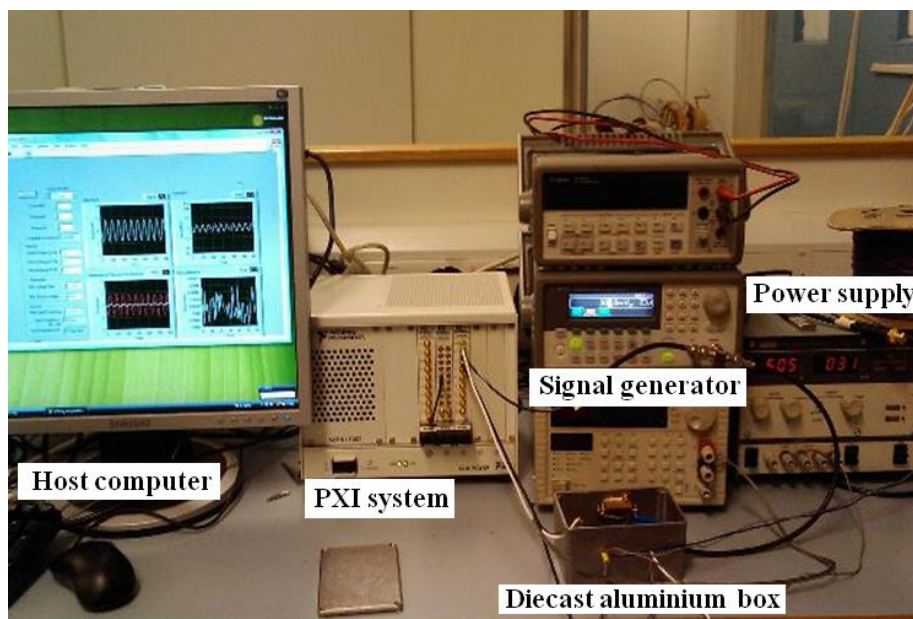
Figure 47 Instruments setup for thermal test

a)
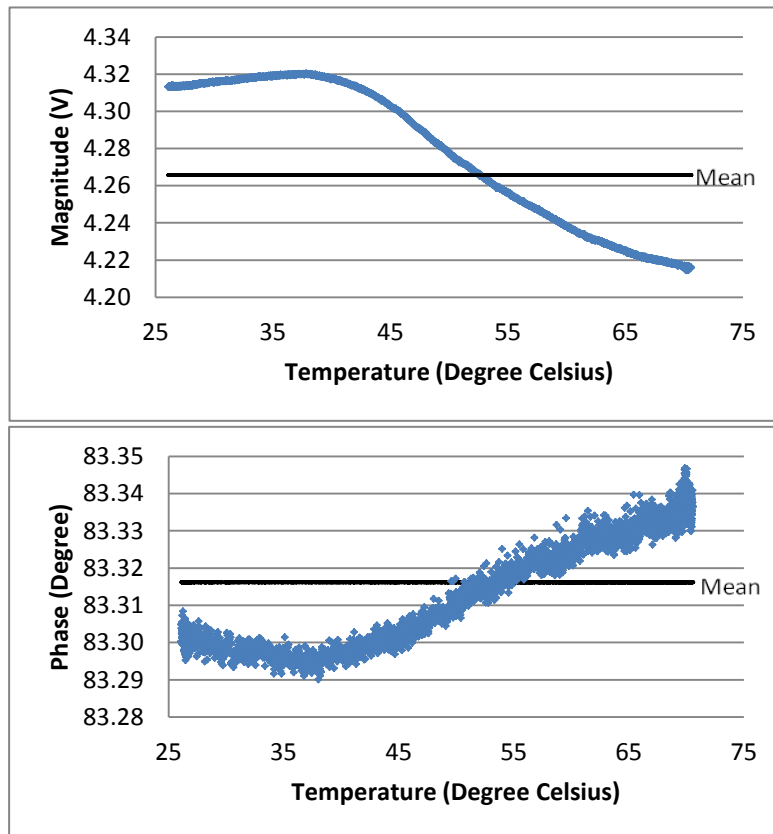
b)

Figure 48 Magnitude and phase response of AD8129 and AD8000 amplifiers connection in a) heating process b) cooling process

a)

b)

Figure 49 Magnitude and phase response for AD8130 and AD8000 amplifiers connection in a) heating process b) cooling process

a)

b)
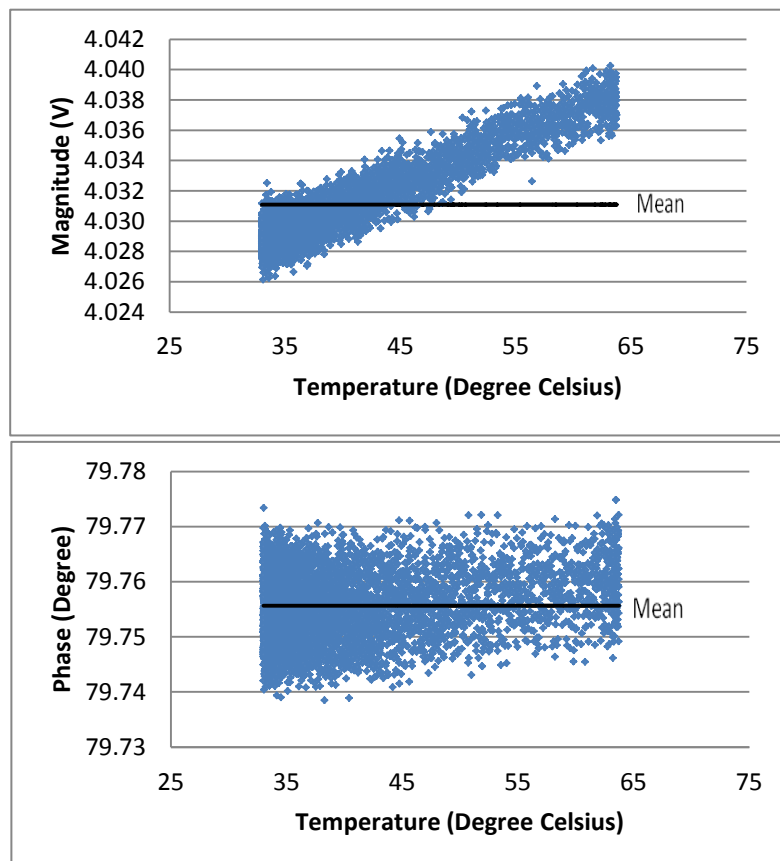
Figure 50 Magnitude and phase response for EL5167 and AD8000 amplifiers connection in a) heating process b) cooling process

a)
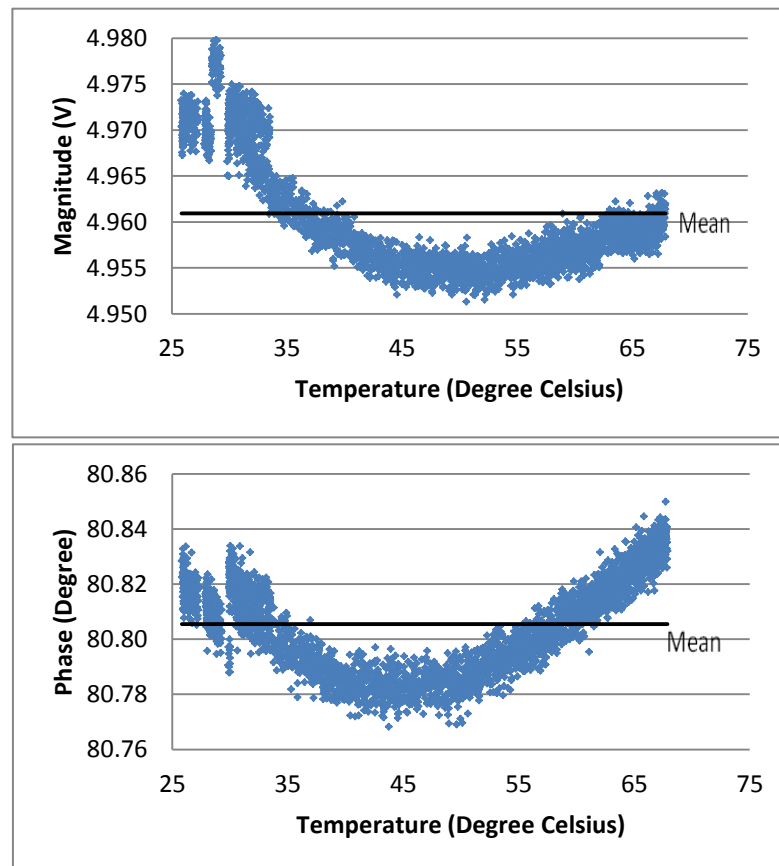
b)
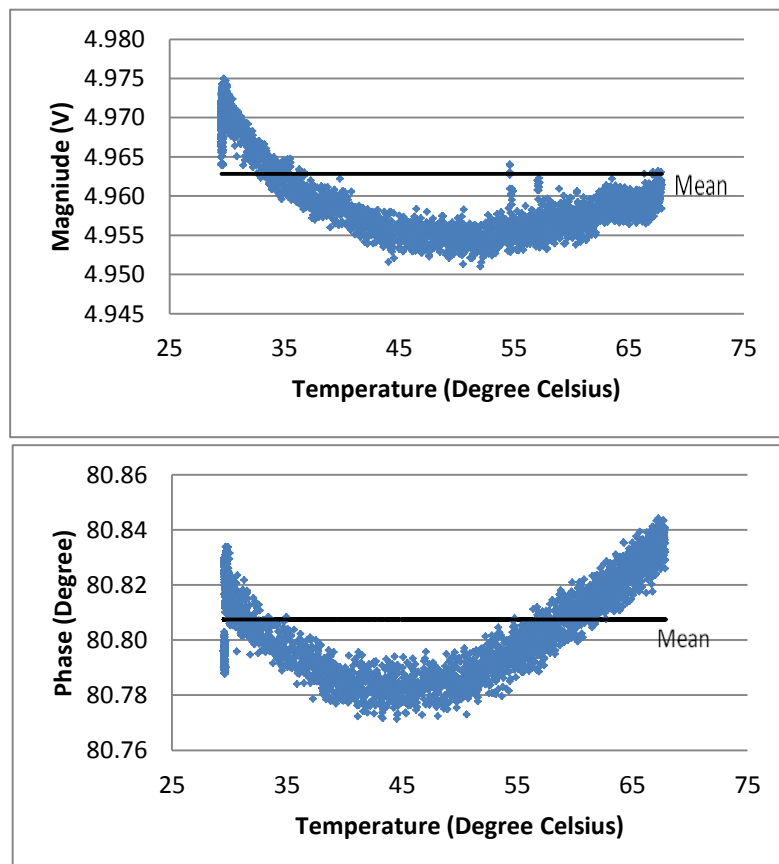
Figure 51 Magnitude and phase response for OPA3691 and AD8000 amplifiers connections in a) heating process b) cooling process

From the thermal stability tests, the drifts of the signal as the temperature increases and decreases are plotted for comparison. As shown in Figure 49 and Figure 50, the amplifier sets of AD8130 - AD8000 and EL5167 - AD8000 have a similar phase drift levels for the complete heating and cooling process. By comparing the same temperature range for both of these amplifiers connections with temperatures up to 65 ^{o}C, the AD8130 – AD8000 amplifier set has a slightly higher phase drift compared to the EL5167 – AD8000 amplifier set, which is approximately 40 millidegree. The EL5167-AD8000 amplifiers set shown approximately 35 millidegree phase drift. This indicates that for every ^{o}C change in the thermal stability test, the AD8130 – AD8000 amplifiers set drifted about 1.1 millidegree. For the EL5167 – AD8000 amplifiers set, every ^{o}C of the temperature change results 1 millidegree phase drift.

Although the AD8129 is from the same family as AD8130, this amplifier has a higher temperature drift comparatively as shown in Figure 48. It drifted approximately 55 millidegree in phase during the heating and cooling process. For the board with OPA3691 - AD8000 amplifiers set; the amplifiers work with no oscillation at room temperature, however, when it is located in the aluminium box with increasing temperature, its magnitude and phase change shows a its drift response more than the other amplifiers. The cooling down process for the OPA3691 – AD8000 amplifiers set has shown a phase drifts of approximately 80 millidegree, which has doubled the phase drifts of AD8130 – AD8000 and EL5167 – AD8000 amplifiers sets. With a higher phase drift with response to temperature, this amplifier set has shown a less reliable thermal stability comparatively in the warm operating environment.

When these four amplifiers; i.e. the AD8130, AD8129, EL5167 and OPA3692 are connected with AD8000, the amplifier of AD8130 and EL5167 have shown a better performance with lesser temperature drifts. However, considering the more components required, hence, more tracks and complications occured in the circuitry design for EL5167, the AD8130 amplifier was still preferred.

For the next step, the driving amplifiers for driving cables were tested. Two amplifiers from the same family; AD8129 and AD8130 were used to connect to the AD8099 amplifier. This allows a direct comparison with the AD8000 amplifier from the results of previous heat test with the AD8099 amplifier for its temperature effects. The pins for the AD8099 amplifier are

exactly the same as AD8000. Hence, the circuit for the test did not change, apart from replacing the AD8000 amplifier with AD8009.
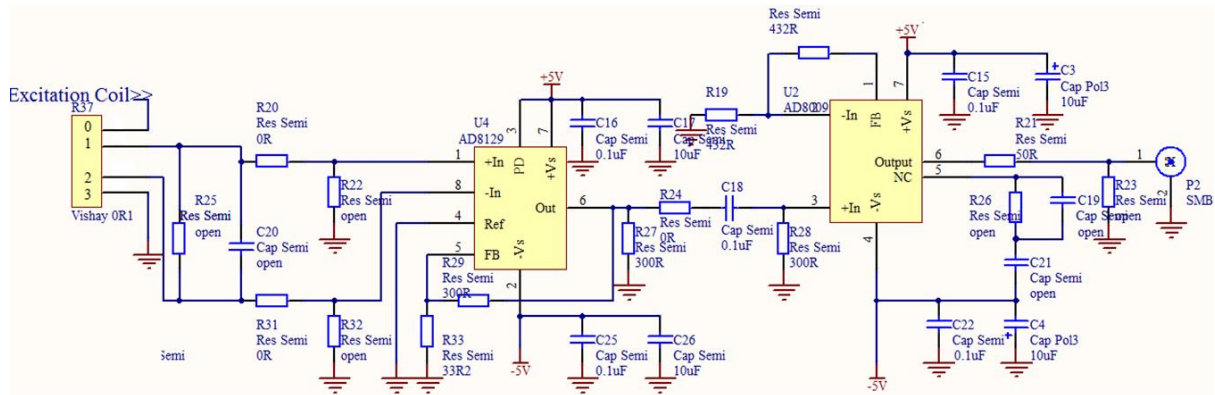
Figure 52 Schematic diagram of the current sensing circuit with AD8129 and AD8009 amplifiers
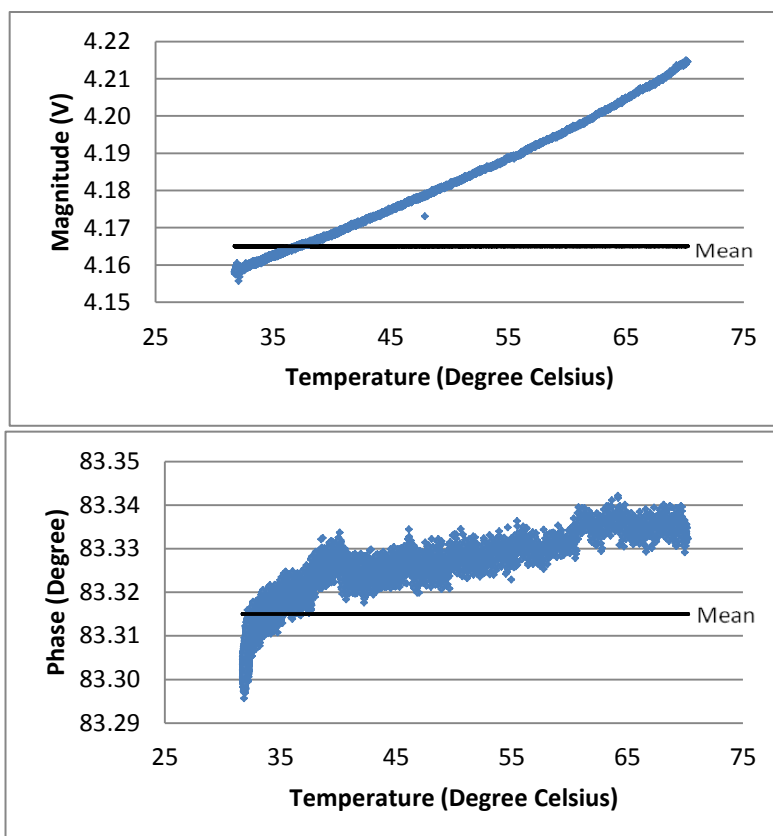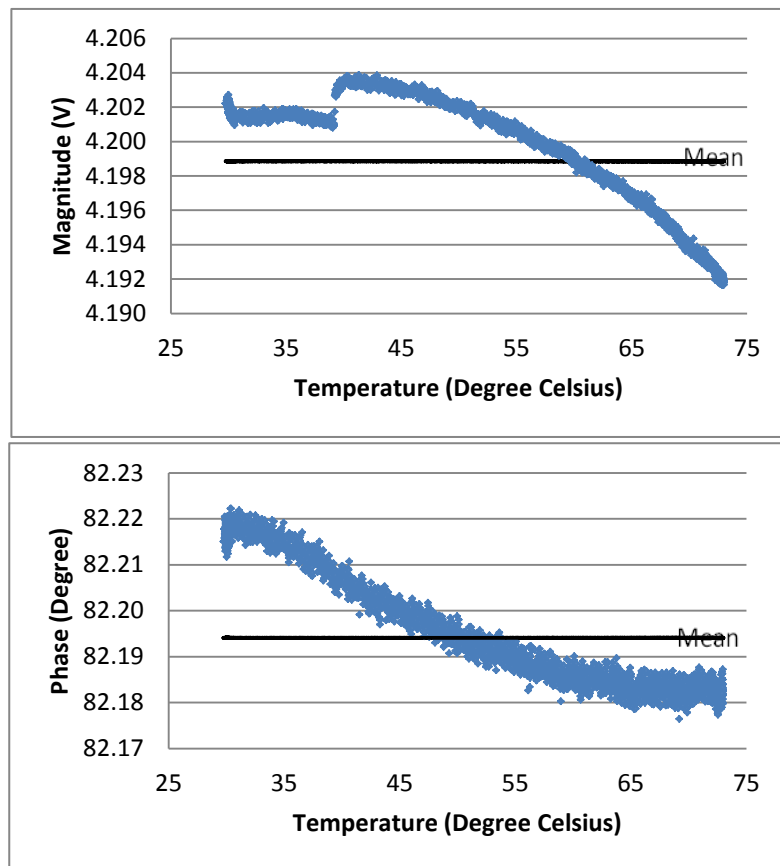
a)
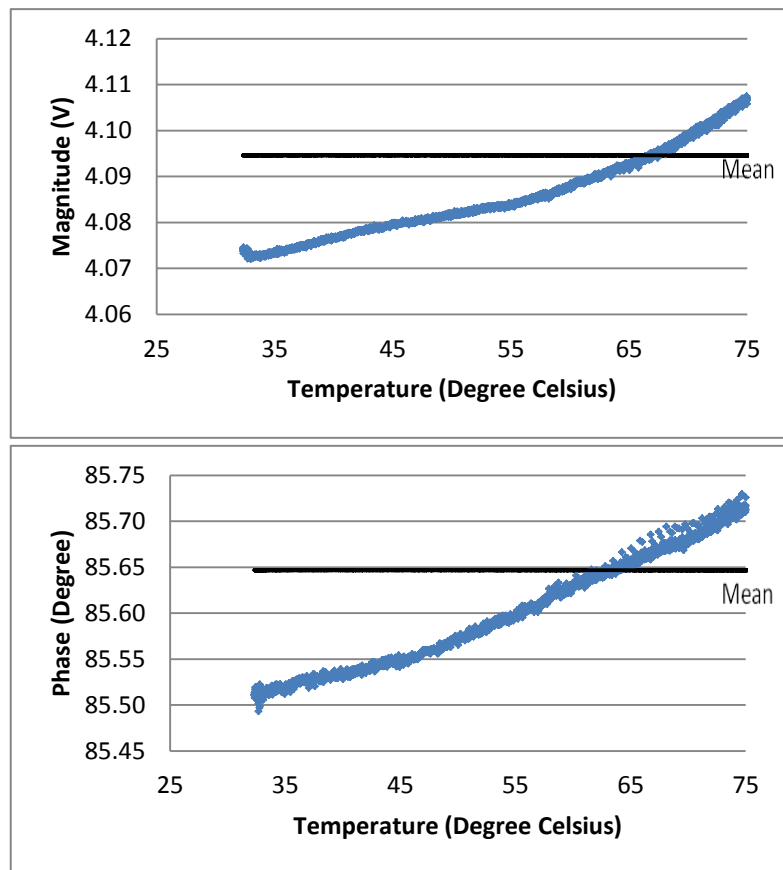
b)
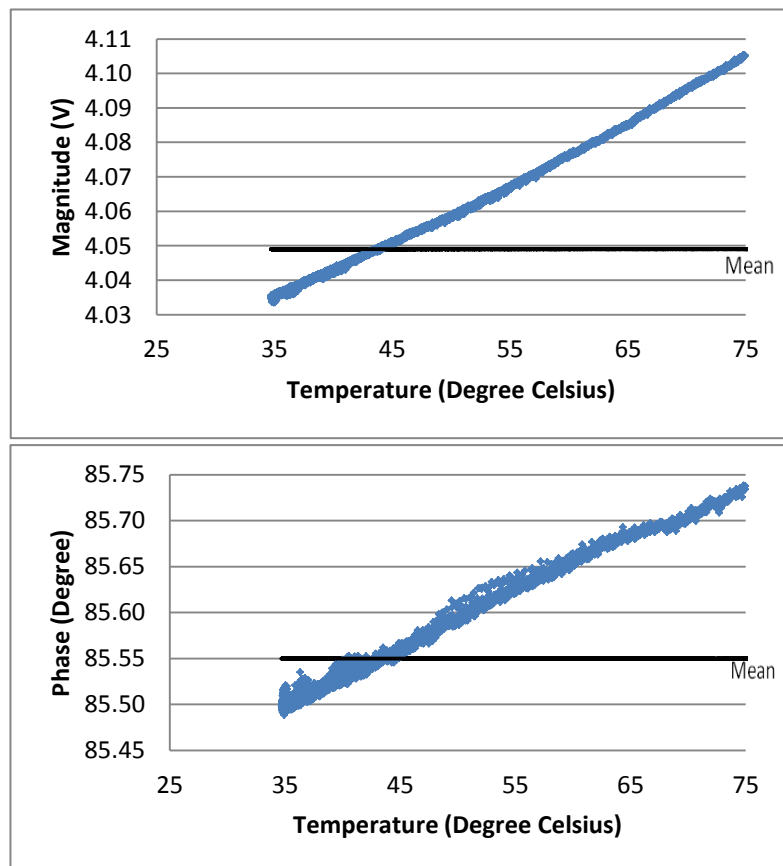
Figure 53 Magnitude and phase response for AD8129 and AD8099 amplifiers connections in
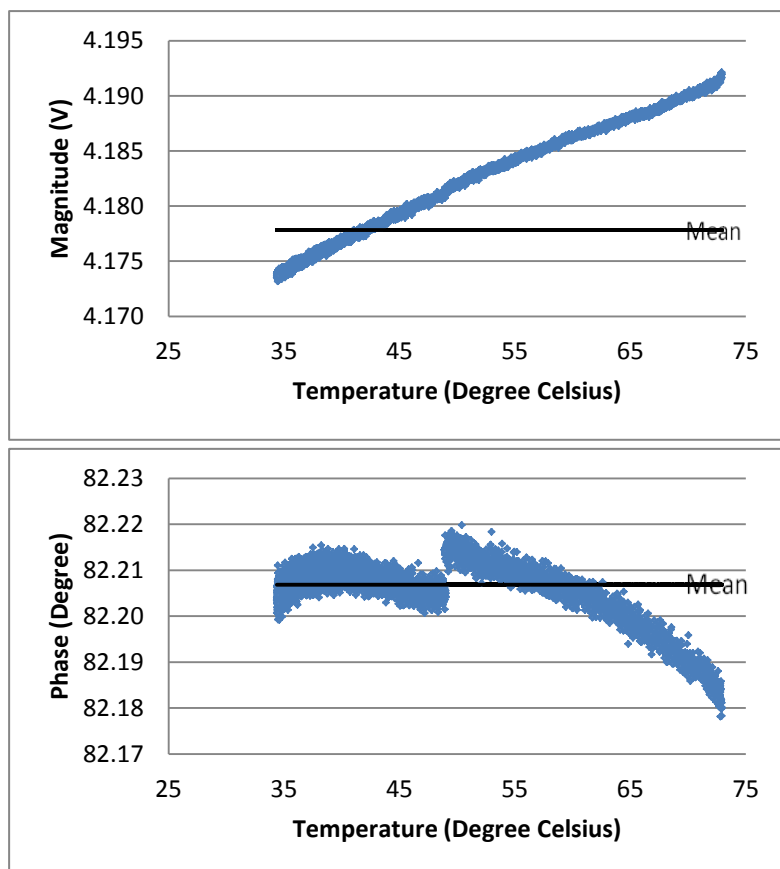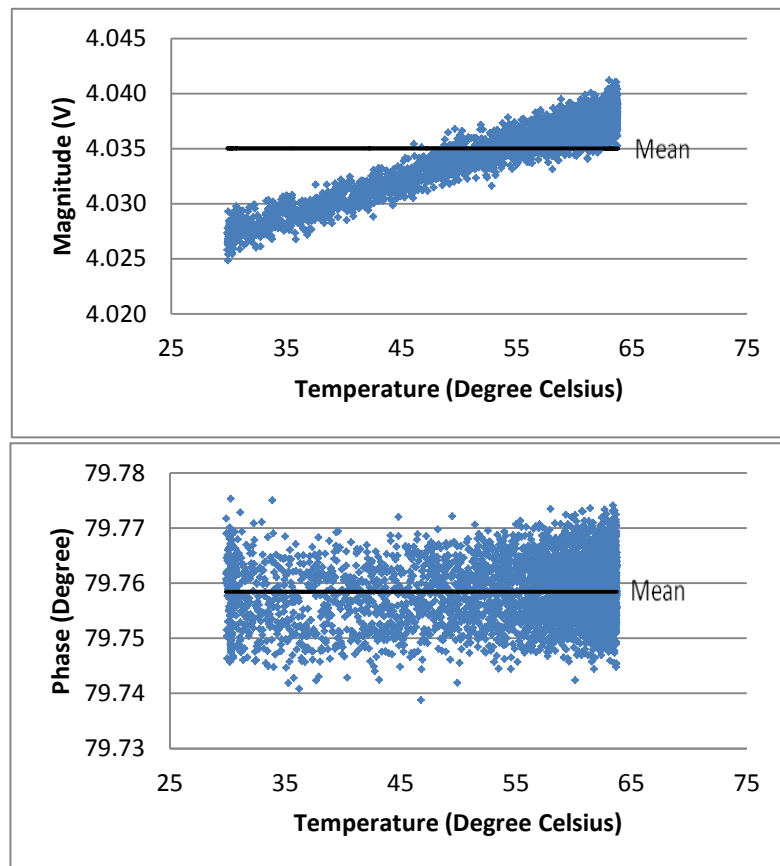
a) heating process b) cooling process

a)
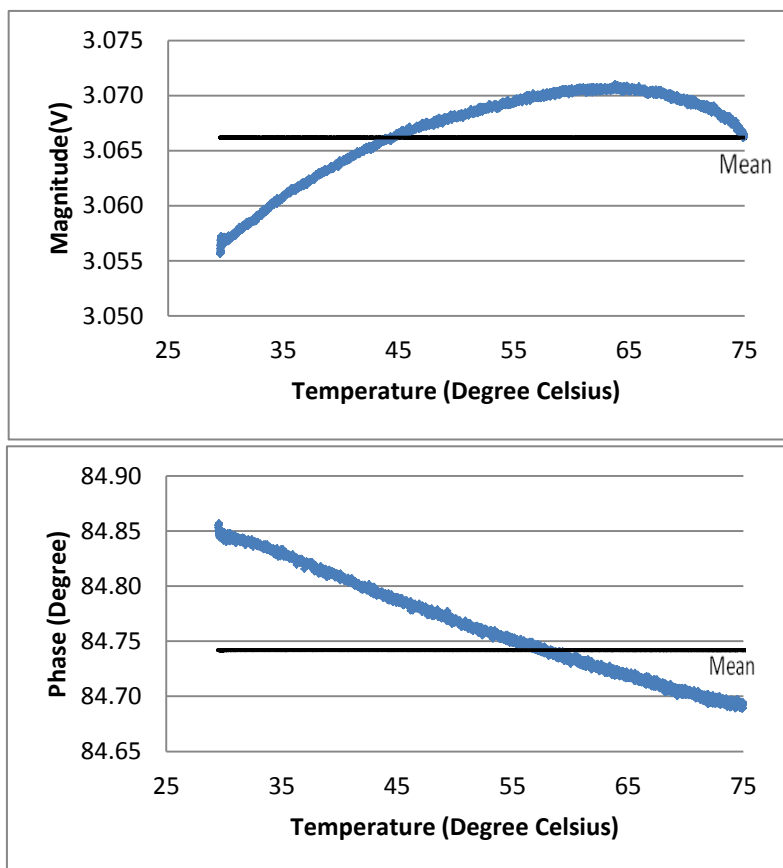
b)
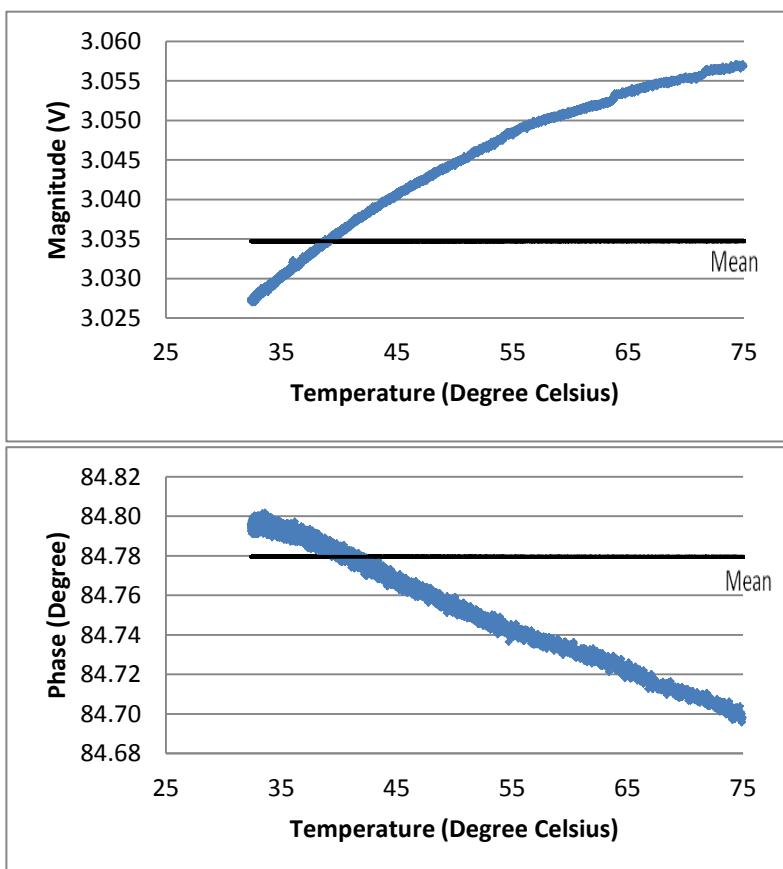
Figure 54 Magnitude and phase response for AD8130 and AD8099 amplifiers connections in a) heating process b) cooling process

By comparing Figure 48 with Figure 53, both of the amplifier connections were constructed with the AD8129 as the first amplifying stage. Hence, the characteristics of heat effects of the AD8099 and AD8000 output buffers can be compared. For the connections of AD8129 - AD8099 amplifiers, the temperature drift in phase is much higher than the connections of AD8129 - AD8000 amplifiers as shown in Figure 48. The overall temperature drift for the connection of AD8129 - AD8099 amplifiers is approximately 250 millidegree, which is about 4.5 times more than the temperature drifts for the connections of AD8129 - AD8000 amplifiers during the overall heating and cooling process.

For the connections of AD8130 – AD8099 amplifiers in Figure 54, the magnitude and phase drifted with respect to the temperature and as the temperature is left cooled, its value of magnitude and phase returned to similar range. This characteristic enables the reduction of temperature effects of the amplifiers if the drift characteristics are known. However, the phase drift levels in the connections of AD8130 – AD8099 were also higher than the connections of AD8130 – AD8099 by approximately four times. Hence, as a conclusion for the thermal stability test, the connection of AD8130 and AD8000 was chosen due to its better temperature performance.

5.2.4.2 Reference Signal Measurement Method

5.2.4.2.1   Resistors

To measure accurately the current reference signal, a four terminal resistor was preferred. A four terminal Kelvin connection was used to remove the unwanted influences of lead resistance. The resistor for current sensing had a small Ohmic value; hence, it is a challenge to test the stability and suitability of this vital component.

Thermal Stability Test

In order to test the thermal stability, two identical resistors were connected in series; one resistor was kept at a constant temperature and another resistor was located inside the dicast box, which was heated with the 3.9 Ohm power resistor. The electronics circuit was not used in this experiments to prevent the temperature drift introduce by other sources. Figure 55,

shows a schematic of the experiment. The signal was inputted by the signal generator to the resistor that is outside of the dicast box. Two probes were placed across the two resistors as shown in the schematic and the phase of the two signals was compared. This experiment has an assumption that the phase across the first resistor situated outside of the box with room temperature does not vary throughout the experiment.
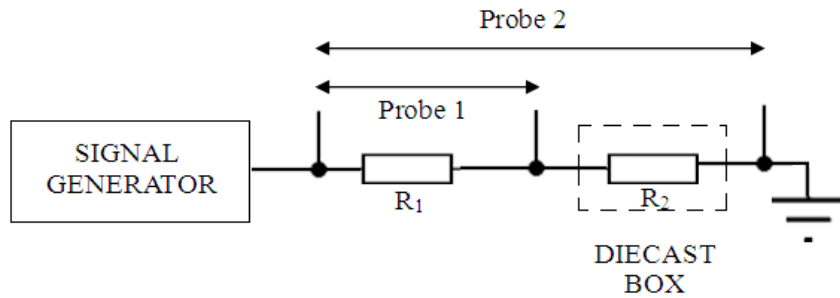
Figure 55 Schematic of the resistor thermal stability experiment

As the resistor required in this experiment is very crucial for its temperature rating, there are limited sources of Kelvin connection resistors in the commercial market that fulfils the small Ohmic and low temperature coefficient conditions. Two of the resistors, which are the Rhopoint AN series and Vishay VCS1625 were used for the thermal stability test. Both of these resistors had a resistance of 0.1 Ohm. This value was chosen as the gains of the amplifiers for the reference signal, U_b are 10. It is easy to calculate the trans-resistance of the overall current sensing system using Ohm's Law (V=IR). The (through hole) Rhopoint AN series resistor has a 0.1% tolerances and the (surface mount) Vishay VCS1625 resistor has a 0.5% tolerance.

Similar to the previous thermal stability tests for the amplifiers, the experiment for this thermal test requires a long heating and cooling time. Hence, the results shown are formed by the mass collections of signals as previous experiments to allow the trend of the signal to be studied corresponding to the heating and cooling process. A minimum length of connection leads was used in the experiment to reduce the interconnect effects on the results.

a)
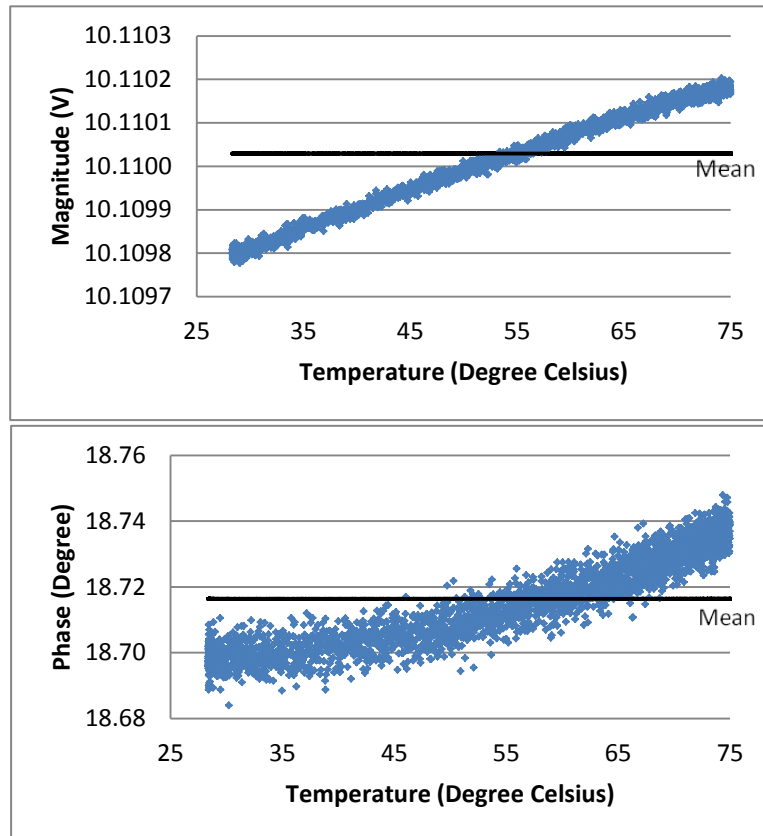
b)
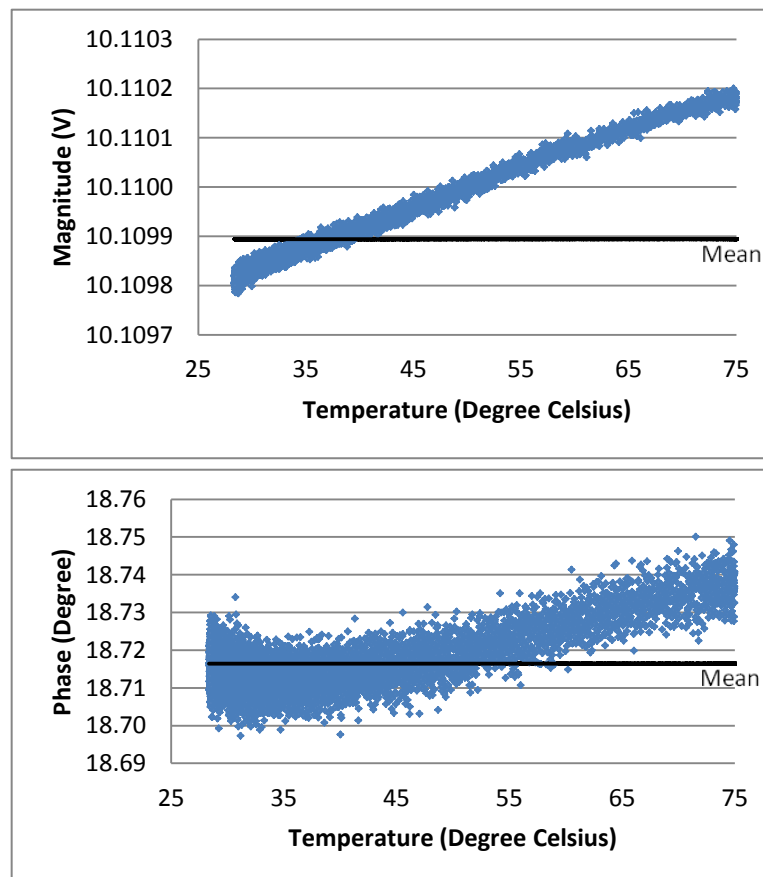
**Figure 56 Magnitude and phase response for Rhopoint AN series in
a) heating process b) cooling process**

a)
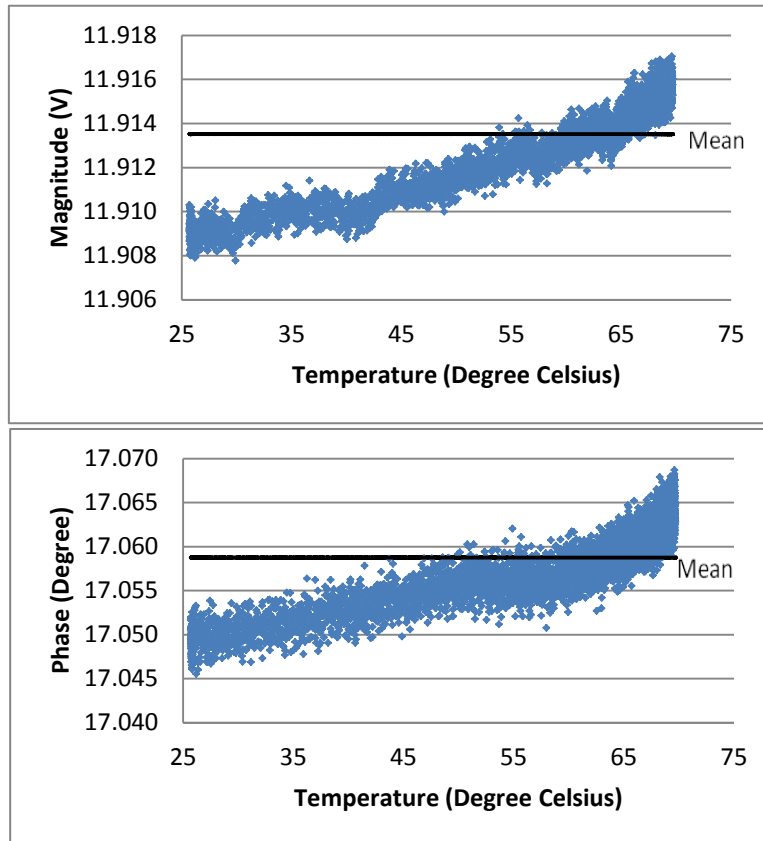
b)
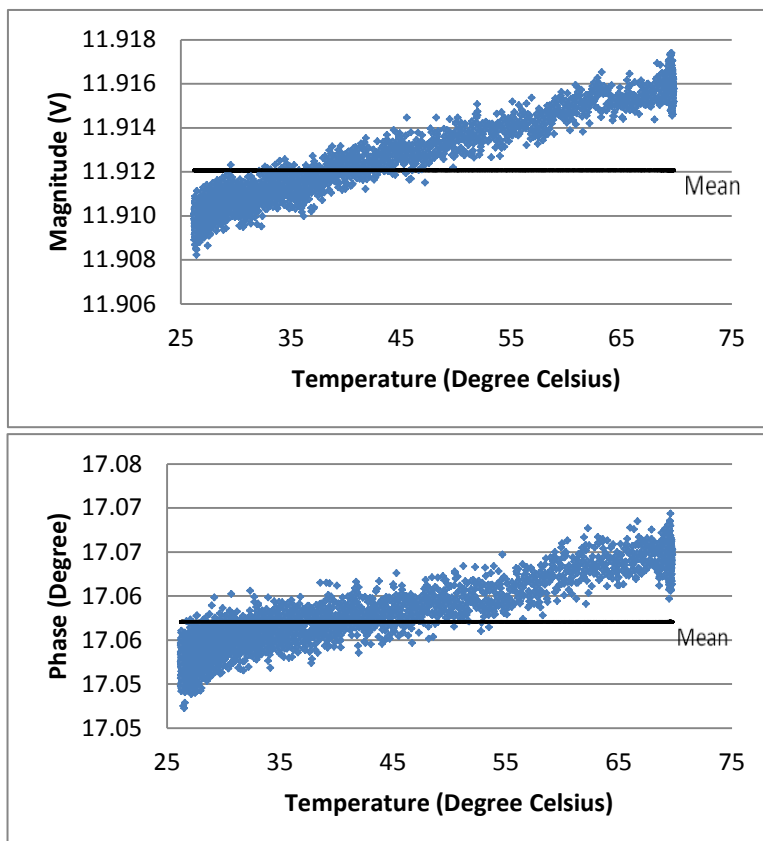
**Figure 57 Magnitude and phase response for Vishay VCS1625 in
a) heating process b) cooling process**

As shown in Figure 56 and Figure 57, both of the resistors are stable in magnitude towards the change in temperature as the figure shown is very small. The Rhopoint AN Series has the magnitude changed of approximately 4 x 10^{-4} V and Vishay VCS1625 has a magnitude changed of approximately 3 x 10^{-3} V for the complete thermal test cycle.

However, for the change in phase, the Rhopoint AN series resistor has twice the drift of Vishay VCS1625 resistor. The drift of the phase signal in the Rhopoint AN series is about 50 millidegree for the overall heating and cooling process. For the Vishay VCS1625 resistor, the drift is 20 millidegree for the overall thermal test. By observing the signals for both of the resistors, Vishay VCS1625 displays a better trend in the phase change. During the heating and cooling process, the signals of Vishay VCS1625 resistor varies in the same scale according to the rise and drop of the temperature.

By closing and opening the lid of the dicast box where the resistor was placed, a significant influence of the aluminium lid towards the Rhopoint AN series resistor was observed. The Vishay VCS1625 resistor appeared to be unaffected by having metal located near it and removed. This effect is very important as the resistor has to provide a very precise reference measurement in order to reduce the error rate. The experimental setup and the furnace supporting structure contain metals; hence, the Rhopoint resistor was considered to be not suitable for the use in this project.

5.2.4.2.2   Reference Coil

Further investigation on the method to obtain the reference signal was carried out. In [78], a pick up coil, also known as reference coil was used to obtain the reference signal by placing it next to the transmitting coil.

Metal Test

To observe the stability of the reference coil, a metal test was carried out. The magnitude and phase change for the pick up coil and Vishay VCS1625 resistor were compared. This experiment has implement a single pair of transmit and receive coil with the circuit

containing the amplifiers chosen in the previous thermal test. The signal was measured by VCS1625 resistor when the current was passed into the excitation coil. This signal obtained from the resistor was compared with the signal obtained by the receiver coil. Then, the difference in phase and magnitude between the excitation signals with the receiving signal was calculated. A similar method was used for the reference pick up coil. By having the pick up coil etched next to the excitation coil the transmitting signal will be coupled to the pick up coil. The signal obtained from the pick up coil will be used as the reference signal to be compared with the signal obtained from the receiver coil.

For this experiment, only the change in magnitude and phase value was considered. This experiment has an assumption that the electronics have no effects on the steel target. A ferritic steel ball was used as a target metal object by moving it from left to right above the excitation-receiving coil pair, reference pick up coil and the current sensing resistor.
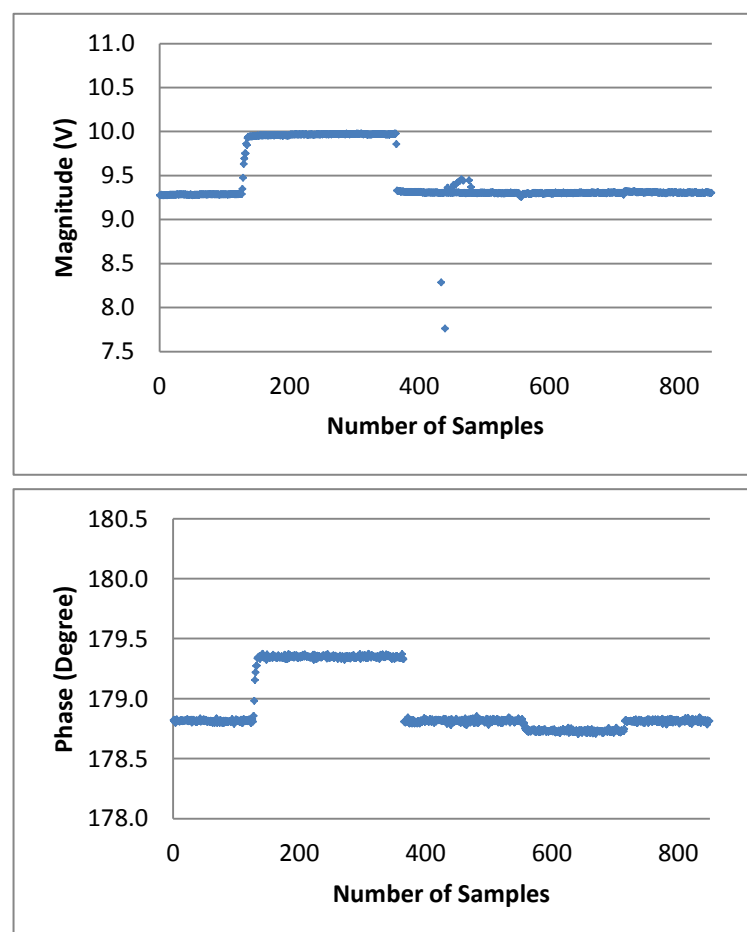
Figure 58 Effect of steel target on magnitude and phase for reference pick up coil

According to Figure 58, when the steel ball was hovered above the reference pick up coil, at samples 130-350, a significant change occurred for both of the phase and magnitude. The phase change is approximately 500 millidegree. When the ball is hovered above the receiving coil, at samples 560-810, the coil shows a small perturbation in phase signal, which is approximately 20 millidegree. No changes were observed in magnitude at this sampling interval. This signal change when the target is above the reference coil is much bigger compared to when the target is above the receiving coil. This indicates that the reference pick up coil is prone to act as a receiving coil itself and was affected by the target object. This mechanism causes difficulties in obtaining an accurate reference signal and unable to predict a proper change of phase and magnitude in the system with respect to the target.
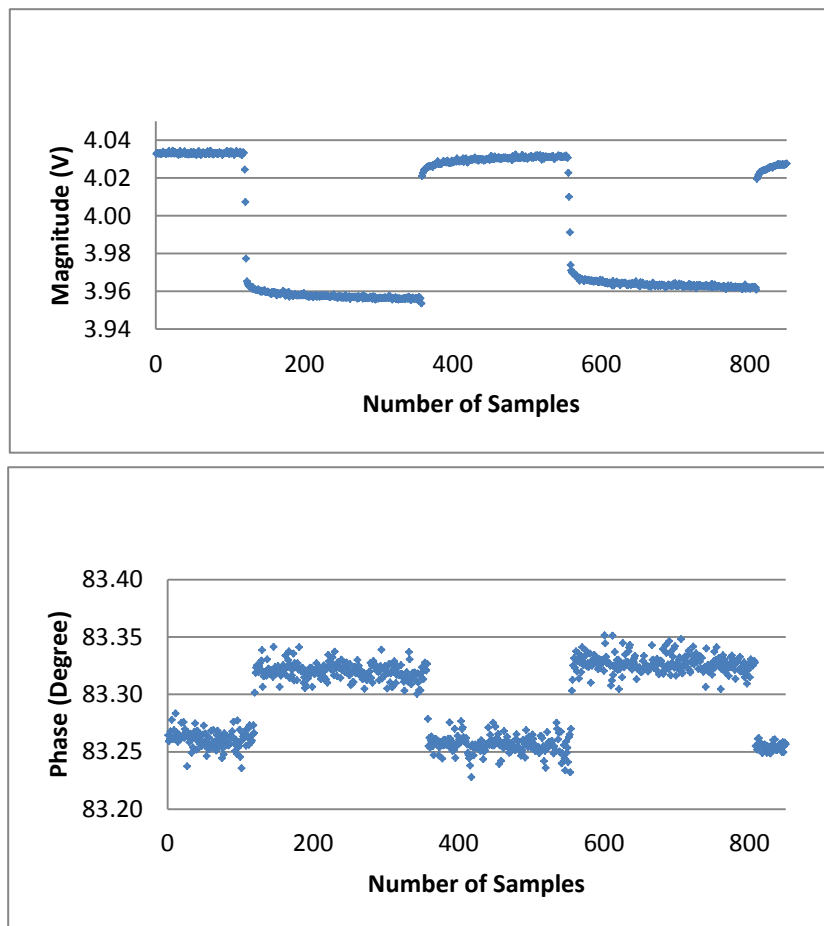
Figure 59 Effect of steel target in magnitude and phase for current sensing resistor, Vishay VCS1625

In Figure 59, the steel ball target was hovered above the receiving coil at samples 144-370 and 567-716. The phase and magnitude have changed simultaneously at the same level for these two incidents, showing consistency in measurement. At samples 420-490, the target is

hovered above the resistor. There is no change in signal at this sampling interval. Hence, it can be concluded that the resistor is more stable with the effect of external sources and reliable in obtaining reference signals.

Temperature Stability

To study the thermal response of the reference pick up coil compared to the current sensing resistor, the coil and the resistor were both connected to the electronics circuit with a pair of transmit and receive coil individually and the acquisition system. This arrangement was able to provide a complete study of the thermal characteristic for both of these methods for obtaining the reference signal. As the previous thermal experiments, the dicast aluminium box was used for heating and also as an electromagnetic shield the external sources of interference which may affect the reading.

The result for the system thermal stability of the reference pick up coil connected with electronics is displayed in Figure 60. During the heating process, the reference pick up coil on the PCB board drifted in both magnitude and phase. The temperature drift in magnitude is not constant with the change of temperature. However, the signal shows a constant change in the phase. The overall heating and cooling process has introduced approximately 350 millidegree change in phase and 0.1 V change in magnitude for the reference pick up coil.

As shown in Figure 61, current sensing resistor shows an approximately 80 millidegree phase change and 0.033 V in magnitude. Comparing the pick-up coil, the resistor drifted 270 millidegree less. Consequently the better thermal stability and the insensitivity to external metal objects for the resistor have encouraged the use of the resistor to obtain reference signal instead of using the reference coil. According to the thermal test results with only resistors involved in Figure 57, the results for thermal test for the current sensing resistor after connecting to the electronics and coils has increased the phase change by 55 millidegree. This may be reduced by the used of other components such as the capacitors and resistors in the circuit that are manufactured for high temperature use. Hence, when re-designing the electronics system in the next stage, components with low temperature coefficient were chosen.

a)
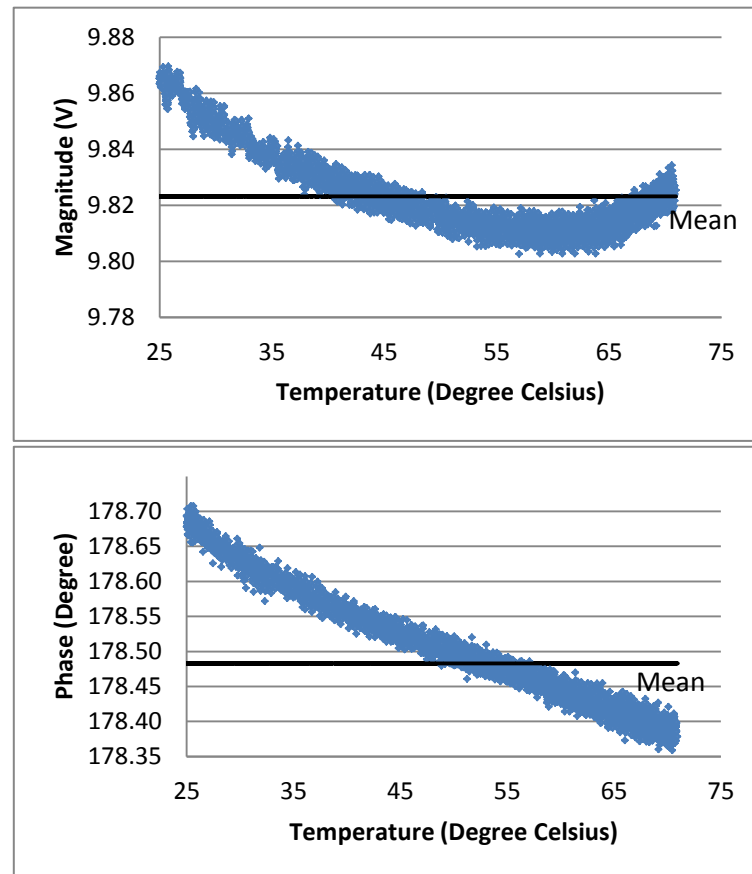
b)
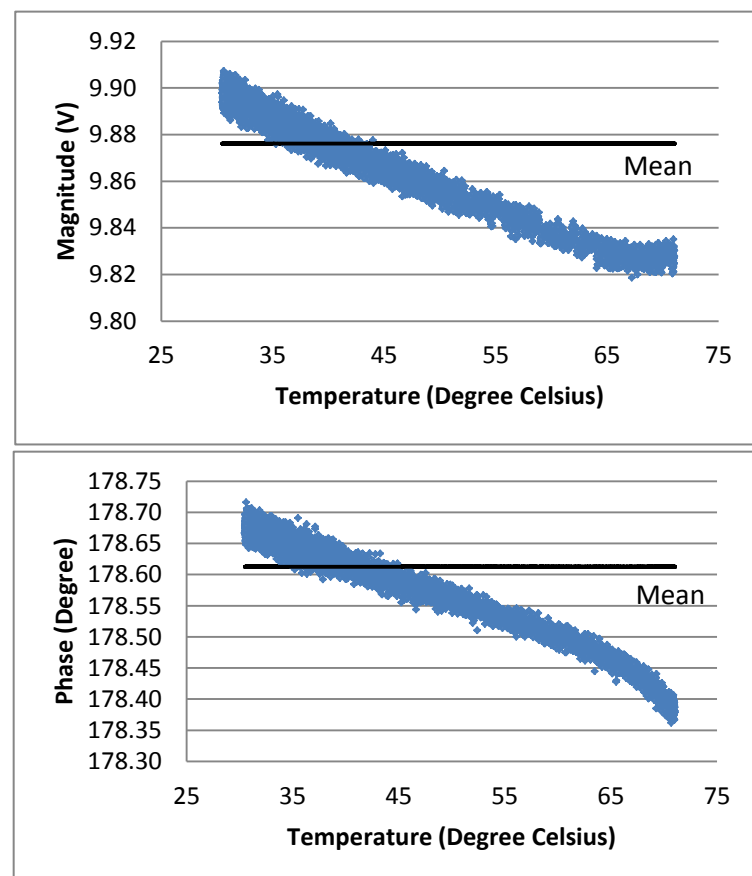
Figure 60 Magnitude and phase response for reference pick up coil with electronics in

a) heating process b) cooling process
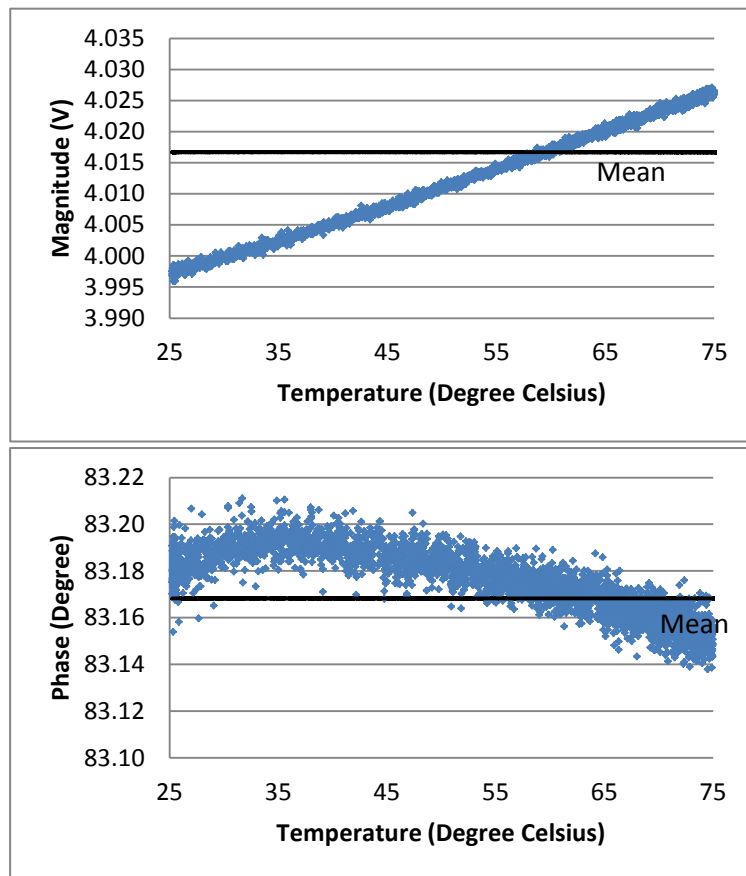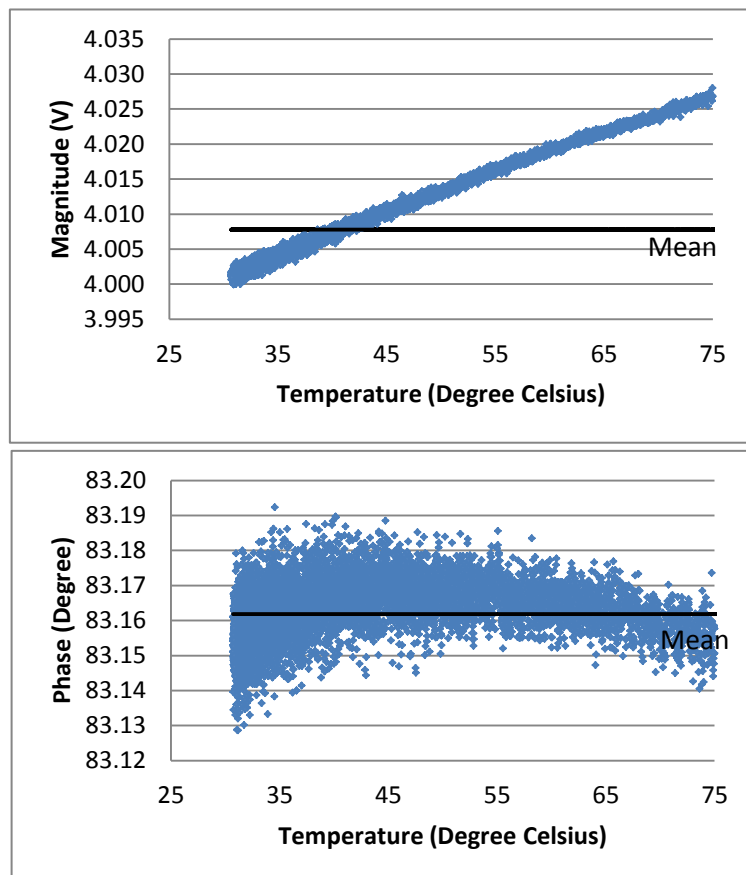
Figure 61 Magnitude and phase response for current sensing resistor, VCS1625 with electronics in a) heating process b) cooling process

5.2.5 System Design and Modification

After finalising the choice of electronic components with the previous experiments by testing with a single transmit and receive channel, the electronics and coils were fabricated with 8 channels side by side. Each individual coil was designed to have its own individual control circuit. As there are 8 channels in the system, with this design enables the simultaneous measurement for 7 channels when one of the coils is transmitting. For the first approach, the channels were designed to operate with a plug-in mechanism. This was to enhance the flexibility in changing the circuit design for development purposes. Figure 62 illustrates this configuration.

(a)

(b)
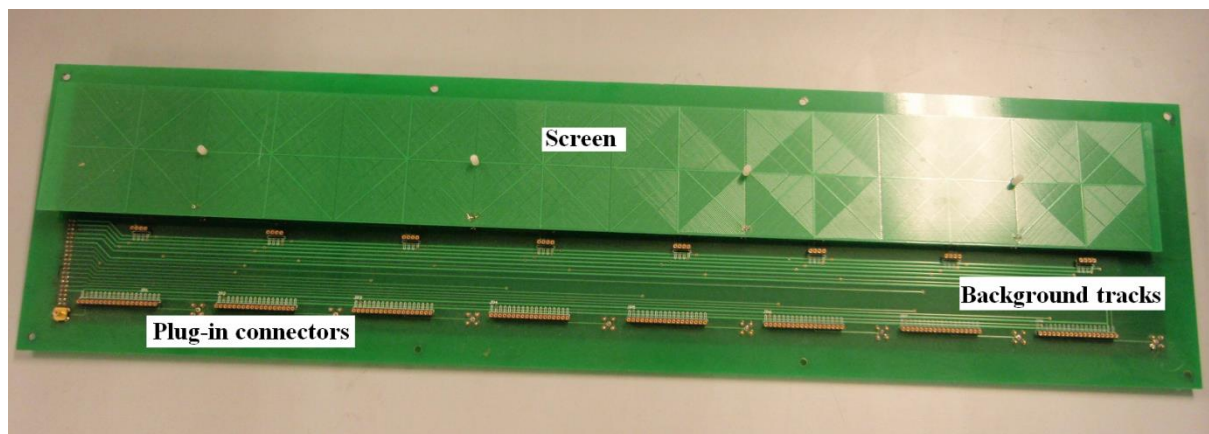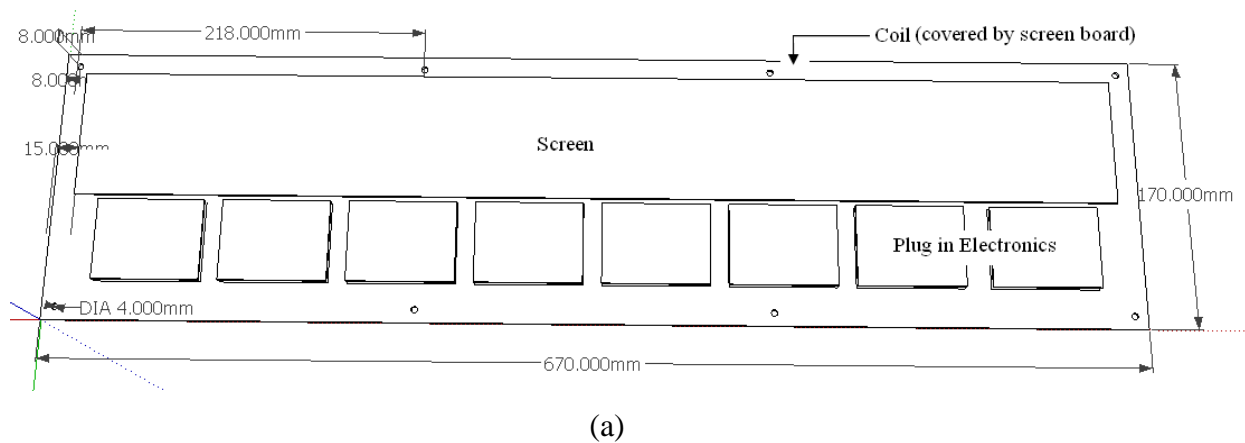
Figure 62 Electronics and coil system a) dimensions b) unplugged electronics channel with background tracks

Each electronics channel was fabricated on a 4 layer PCB. The top layer and bottom accessible layers were used for the transmit and receive circuits. The middle layers of the board were used for power tracks and ground plane. The system was designed to operate with only one active transmitter channel live at a time. When the transmitter channel was operating, the receiving circuit on the same channel was be turn off. This was to avoid overloading the amplifiers by exceeding their maximum operating signal range for the receiving circuit. Since only one channel transmits at one time, this means that the remaining 7 receiver channels in the array are switched on.

In the first design of the circuits, long background tracks on the 2 layers coil board were used to supply the power, to input sinusoidal signal to the transmitting channel, and to control the relays and output signals from the receiving channels. The input signal from the signal generator was constantly connected to all of the transmitting amplifiers. To connect or disconnect the circuits of each individual channel, relays were introduced in the system. They were controlled by the parallel port of the host PC that has power supply of 5 V. The power amplifier of LT1210 in the transmitting circuit has a built-in shut down control pin (pin 3). When re-designing the circuit, the shut down pin was also integrated into the system. This shut down pin was connected to the same line as the relays. This was to ensure that simultaneous control was applied for the two of the signal control mechanisms, preventing leakage of the input signal to the circuit.

5.2.5.1 Crosstalk

An experiment was carried out by utilising this electronics design by operating just one transmit channel and one receive channel. However, when the relays were turned off for the transmitting channel, there was still signal passing through the coil and circuit. It was found that this signal was introduced by the parallel control tracks, which have significant signals in most of the power tracks, as well as the ground tracks.

Crosstalk is one of the most significant problems that are commonly found in long circuit tracks, long cables [118] and also connectors [119]. In order to overcome crosstalk on the unshielded long parallel background signals traces, individual coax cables for transmit, receive and input signal for each channel were used. The coax cables, RG316 are shielded

and hence can prevent interference of signals from other channels. This has stopped the crosstalk effect on the transmitting channel when the relay has switches the channel off. The RG316 cable is small size and a high temperature coax cable that is able to withstand temperature up to 200 ^{o}C. The diameter of the cable is 2.5 mm. An additional step for the crosstalk interference prevention was to twist the coax cables together. Twisted cables are in common use in telecommunication applications to reduce the crosstalk. Unfortunately, with the introduction of more cables into the system, the weight of the sensor increased significantly.

5.2.5.2 Capacitive Coupling

For the first screen design as shown in Figure 62(b), when the system was tested with tap water (conductivity 0.012 Sm^{-1}), there was a small signal change. After investigation, it was shown that capacitive coupling between the targets to the coil was not able to be shielded appropriately by the screen. Hence, the screens were modified to be bigger for the top coil and bottom coil with more coverage at the side and top of the screen following the maximum size of the coil array. The new screen was made in house with a single layer board as shown in Figure 63.

5.2.5.3 Reference Ground

A significant interference in signal was observed when the equipment was physically contacted. These included the signal generator, the PXI system, and the power supplies. The interference in signal was up to several degrees in phase change. This value is significant and comparable to the signal obtained from the molten glass. In the observation, the PXI system has shown the biggest effect towards the physical contact. The signal change was according to the area of the contact surface with the equipments.

The external cases of the equipments are made of metal. It is often connected to the ground reference internally. However, appropriateness in the ground connection was unknown. Initially, each of the instruments was connected physically at several points to the power supply ground pins. This method reduced the sensitivity of instruments towards physical ground contacts. By connecting all of the equipment with the same extension plug, is able to

provide the same ground level as reference for the power input to all the equipments, which has overcome the problem of physical contacts with the equipments and the associated circulation of common mode ground currents.

5.2.5.4 Aluminium Ground Plane

The elimination of the use of the long tracks left the bottom area to be not in use. Hence a modification on the electronics arrangement was carried out. Considering the ease and accuracy of modelling, an aluminium strip has replaced the heat sinks that are attached to the individual power amplifiers, which often comes with complicated shapes and appears to be a chunky metal in the circuit. The aluminium strip was placed together with the electronics and positioned at an angle of 90° with the coils, reducing the effects of the magnetic field on the electronics circuit. The aluminium strip was also useful as a ground plane for all the channels circuits, which helps the electronics to have the same reference ground. Figure 63 shows the position of the aluminium ground strip as well as the electronics.
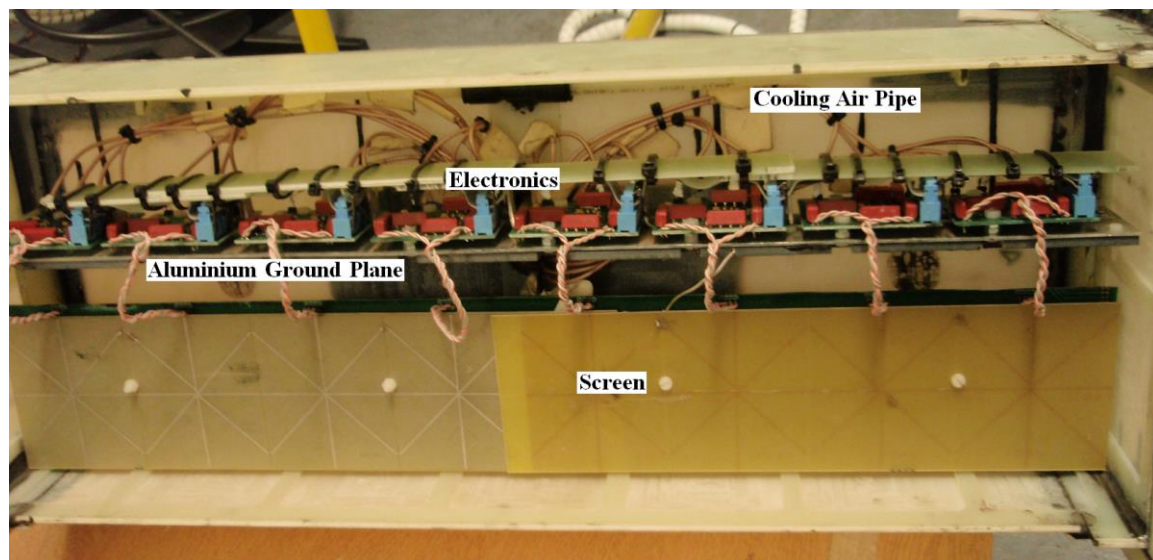
Figure 63 Sensor fitted in glass fibre housing

5.2.6   Enclosure

At the beginning of this project, the experiments were carried out in the laboratory and test rig, at room temperature. A wooden base container as shown in Figure 64 was used to hold the sensor in place, and no lid was used.
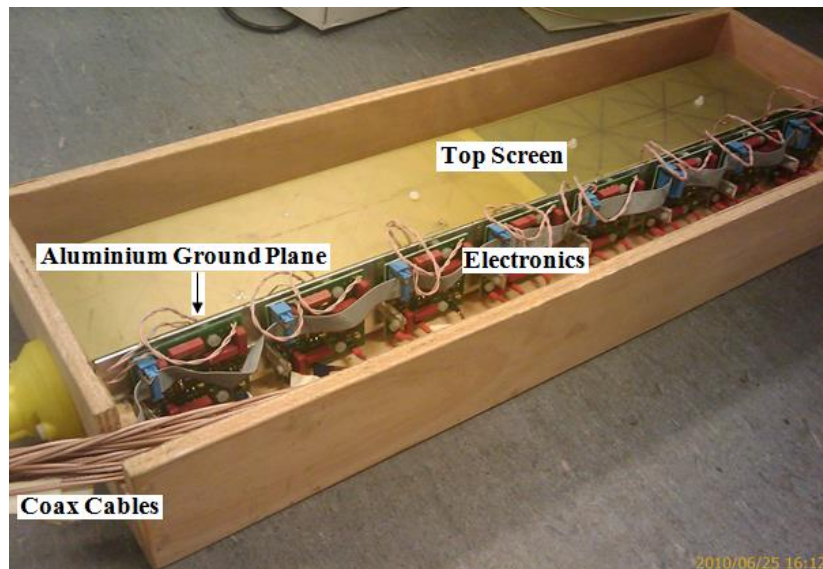
Figure 64 Electronics fitted in wooden base container

To carry out the experiment under the furnace, where the effect of the high temperature was the main concern, an enclosure, also known as the sensor housing was required. The enclosure is used as a protector for the electronics systems from the heat radiation from the furnace. It was also used to stabilise the physical position of the sensor.

The enclosure was formed by two parts, a top lid and a bottom pan. The design was to allow the internal electronics to be accessible and gives freedom to modify or fix the electronics. The top lid will be directly in contact with the furnace bottom, which has a temperature of 400 to 500°C. This is the main thermal shield to protect the electronics from burning. For the bottom pan, the temperature of the location is much milder, which is approximately 70 to 100°C. The main criteria for this enclosure were to be robust enough to be moved and used in different locations. It also has to withstand some pressure applied on it whilst pressing against the furnace base. As the sensor will be lifted by the technical staff during the measurements, the enclosure has to be as lightweight as possible. To construct the enclosure, the material of

the enclosure has to be non-conductive and non-magnetic to avoid any influence on the signals.

The first bottom pan housing was made with a glass fibre material, Flame Retardant 4 (FR4). This material is able to withstand temperatures up to 150 ^{o}C. To ensure that the material is strong enough to hold and secure the electronics and coils, the walls of the bottom pan was made of 5 mm thick panels. To reduce the weight of the FR4 holder, a cut-outs technique was exploited. Cut-outs are often used in aerospace, civil, mechanical and marine structures [120] to lighten the weight of the structures but maintain the stiffness and strength. However, the main application of the bottom pan is to defend the electronics from the heat, hence, the board for the walls are only thinned down in columns instead of drilling through holes. The cut out experiment was carried out by thinning down the wall to 4 mm, 3 mm and 2 mm with a sample material. However, the in house workshop was unable to produce a wall that is thinner than 2 mm, hence, the minimum thickness of the cut-outs column was chosen to be 2 mm. As shown in Figure 65, all of the walls are thinned down in columns with the cut-out technique. A high strength and high temperature epoxy, 832HT was used to bond the boards together for the bottom pan.
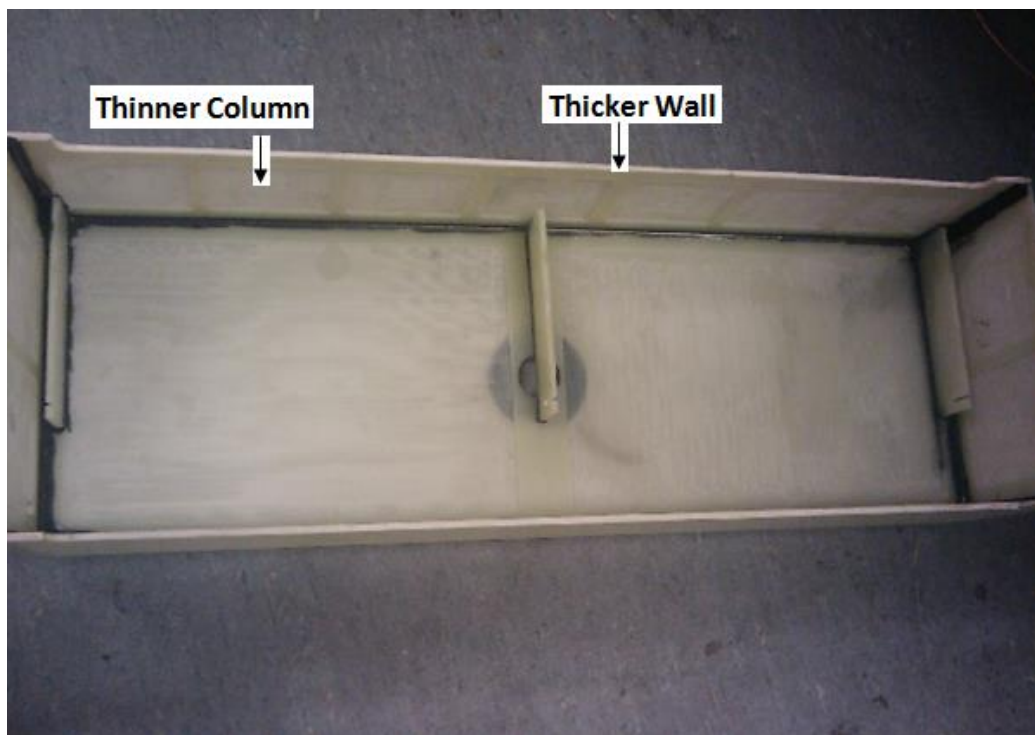
Figure 65 FR4 electronics holder (bottom pan)

The cooling air pipes and the cables were designed to be connected into the enclosure via 40 mm holes in the centre of the bottom pan. An EXTREN structural fibreglass pole was embedded at the bottom of the enclosure as a support for the enclosure. The fibreglass pole was able to act as a sleeve for the cables, protecting them from the heat and also to tidy the cable runs.

For the enclosure lid, a higher temperature resistant was required as the lid has direct contact with the furnace during the experiments. Two materials, which are the FR4 and Fiberfrax Durablanket were chosen as the materials for the lid. The FR4 material with cutouts was used as a moulding frame to hold the Fiberfrax Durablanket, as the blanket is soft and not able to maintain its shape to form of the lid. The blanket was bonded with a high temperature adhesive, Fixwool Adhesive 1000 from Unifrax. This adhesive was able to withstand up to 1000 ^{o}C. This blanket is able to provide a high ability in shielding the electronics system from heat. It is able to withstand temperature up to 1350 °C. For the top wall of the lid, a 50 mm thick blanket was used to cover the FR4 frame. For the side walls, only 25 mm is used. This made the overall lid dimension to be 701 x 350 x 200 mm (external). The top lid design is displayed in Figure 66.

To prevent overheating, the electronics in case of a failure of cooling system during the experiment, the internal temperature of the enclosure was measured under the furnace without cooling pipes and electronics in it, for approximately 5 minutes. The internal of the heat shield reached up to 72 ^{o}C. This temperature was near the maximum operating temperature for most of the electronics. Therefore, the electronics cannot be left without cooling for a long period. In this experiment, since there is no electronics operating in the box, the heat dissipated is not considered. Hence, the internal of the box is assumed to have a higher temperature during the experiments.

5.2.7   Modification of Sensor Head

The overall weight of the first sensor head was approximately 13 kg without cables. This weight for the sensor is dangerous to be held over the head for measurement.

A new design of the sensor head was proposed in order to reduce further the weight of the sensor. Two materials, which are the Microtherm® Quilted Panels and Microtherm® Standard Panels, are supplied by the specialist for heat shield as the material for the new enclosure. These materials are covered with woven glass cloth, which is much cleaner to be used compared to the fibreglass blanket used in the first enclosure. To provide the same heat protection level as the fibreglass blanket, only half of the thickness is required for these Microtherm® materials. The Microtherm® Standard Panels are used to form a frame for the top lid. Then, the Microtherm® Quilted Panel is layered on the top layer of the lid, as a shock absorber for pressing against the furnace wall. The external dimension for the new lid has decreased down to 667 x 113 x 290 mm.

The electronics and screens PCB boards are printed on a 3 mm thick material. This is to provide strength and firmness when it is stacked together. In the new sensor design, the PCB boards are used as the bottom support without needing an additional bottom pan. The electronics and circuits are the same as the previous due to its reliability in the measurements. For the cooling system, the sensor head uses the external compressed air supply to be connected into the system as the previous version of enclosure. Figure 66 shows the comparison of the original top lid with the new lid which is in smaller size. The overall weight for the new sensor is approximately 6 kg without cables. This new proposed sensor head has successfully halved the weight of the previous sensor head.
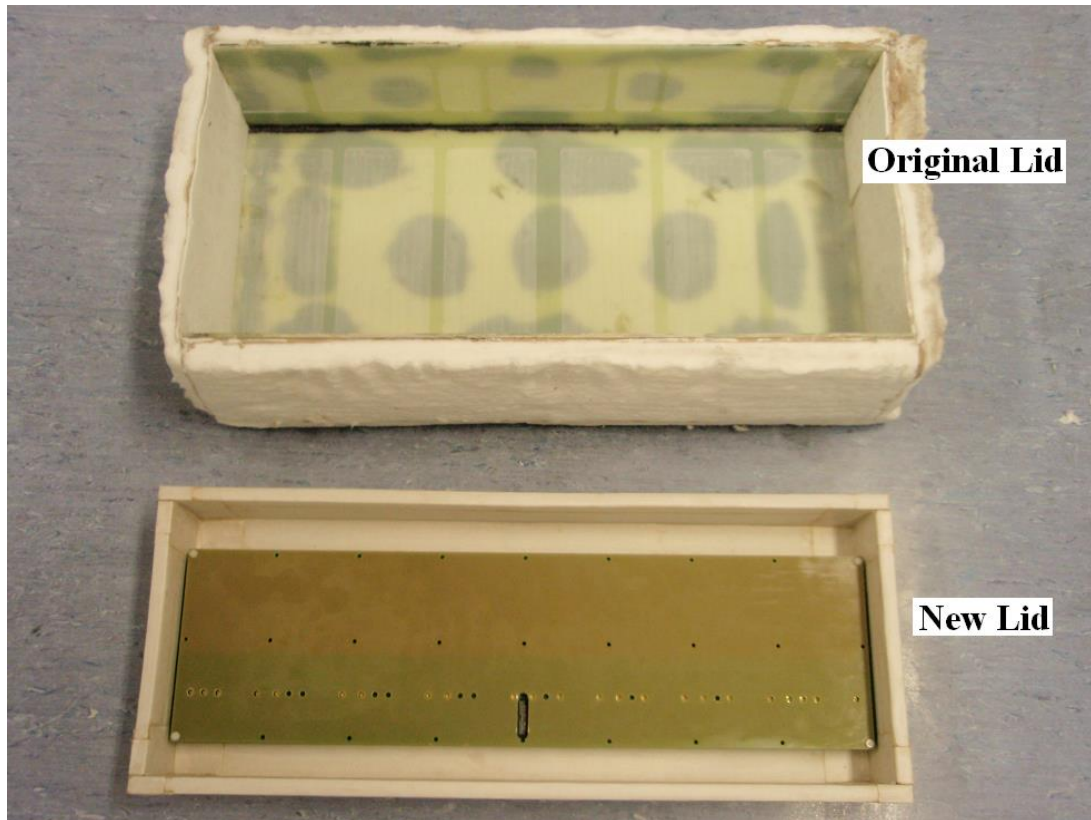
Figure 66 Comparison of the lid sizes for the original sensor head and the new sensor head
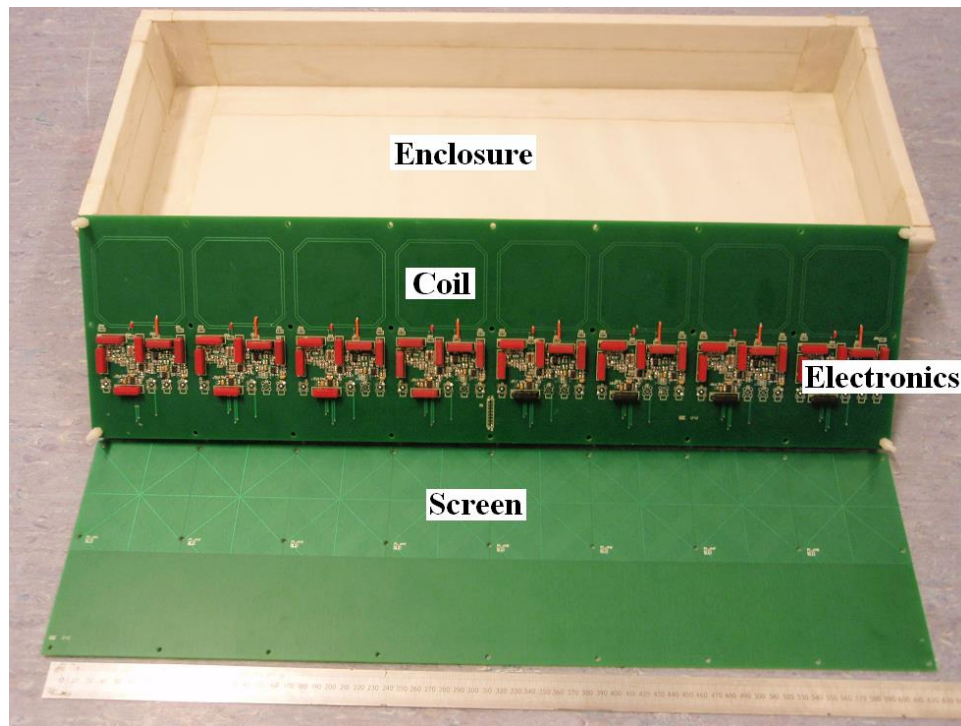
(a)
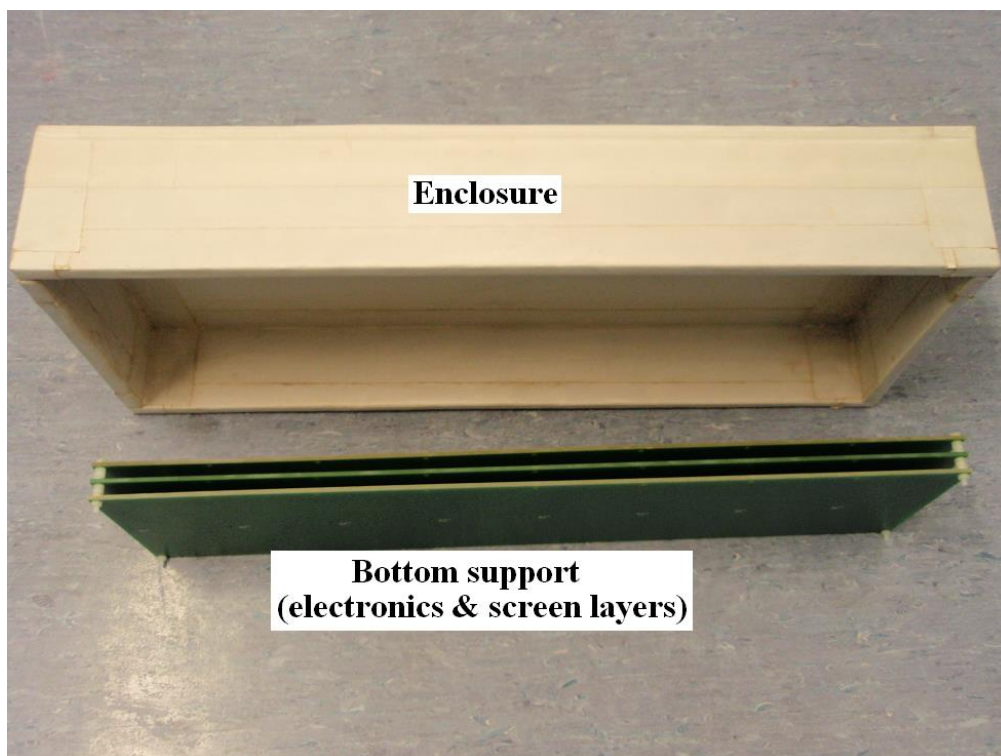
(b)

Figure 67 Electronics and screen layers as bottom support

(a) individual PCB layers with circuit and screen displayed

(b) electronics and screen layers stacked together

5.3   Acquisition System Instruments

Figure 68 shows the instruments required for a basic acquisition system. It is formed by a group of hardware devices which consists of two laboratory bench top power supplies for +/-5V and +/-15V DC supplies a PXI data acquisition system, a desktop computer as the host computer, a signal generator and the front end electronics sensor. In the diagram, a bench top multimeter which is used for measuring temperature is not included, as it is an optional measurement tool depending on the experimental locations. When the experiment has taken place in the laboratory or test rig, temperature measurement is not required. However in the furnace test, it is a requirement to monitor the temperature to ensure the electronics are not overheated.
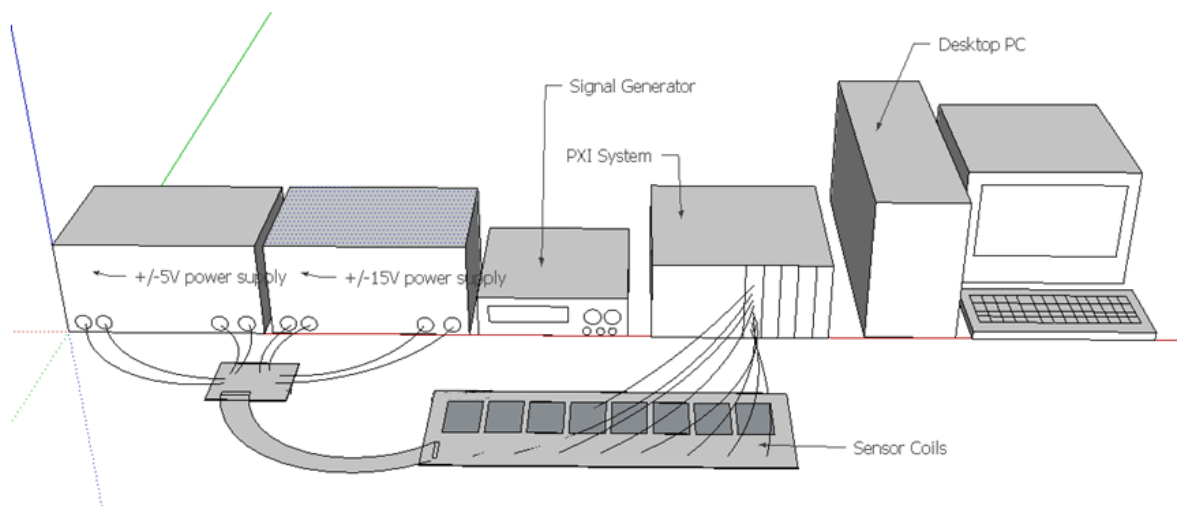
Figure 68 Data acquisition system instruments

The operation of the system is controlled by a host computer using LabVIEW software, which will be discussed in a following chapter. This software is mainly used to run the PXI system, the parallel port to control the relays of each electronics channel and to save the measurement data. The PXI system consists of a 5 slot chassis (PXI-1033), which has 2 digitiser modules (PXI-5105) and a multiplexer (PXI-2593) fitted in. The two digitiser modules enable 16 input signals to be measured and analysed simultaneously.

Initially, the electronic circuit for all channels were designed to be connected to the signal supply in all states. This fully relies on the parallel port to turn on and off the relays and controlling the shut down function of the power amplifiers to cut off the signal connections. However, an additional modification was carried out to prevent the signal leakage into the channels during their off-state. The signal from the signal generator is passed to the multiplexer before inputting into the power amplifiers. This has added an additional cut off function for the signals from entering the system at the instruments stage. The multiplexer uses custom software written in LABVIEW to scan through the channels of interest, connecting the input signal to one transmitting channel at a time.

As discussed previously, 3 coax cables; transmit, receive and the signal cables are connected individually to each channel. To reduce the time of mounting and dismounting time for these 24 cables individually, all of these cables are secured in three 8-way D-sub connector as shown in Figure 69.
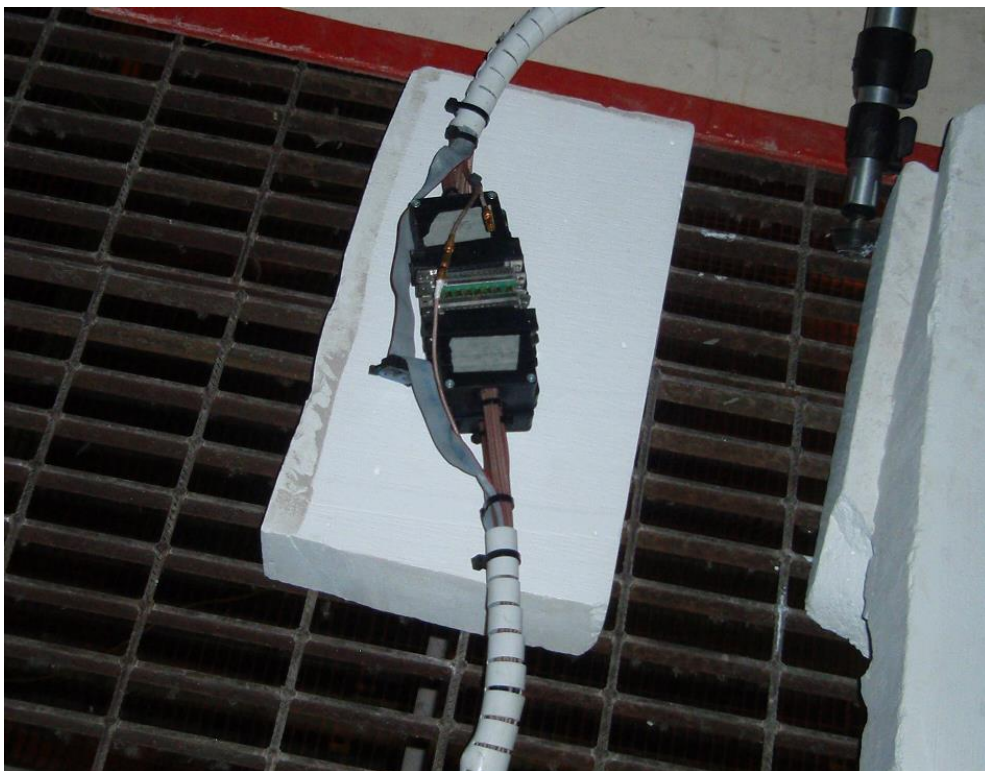
Figure 69 D-sub connectors clustering transmitting, receiving, and input signal cables

To make the system more portable, the weight and size of the overall equipments were taken into consideration. For online measurements, a portable computer and lighter equipment as illustrated in Figure 70 are desired.
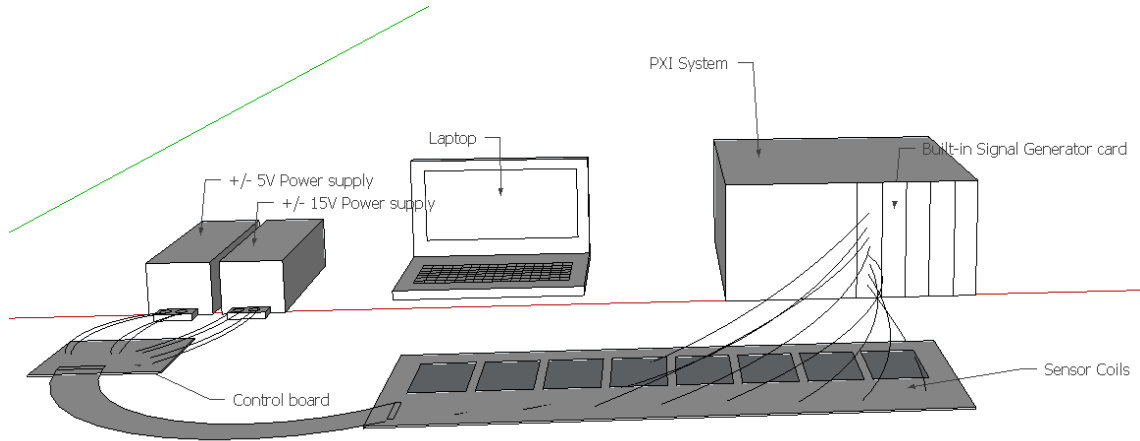
Figure 70 Light-weight data acquisition system equipments

The main contributions among all the equipments are the two bench top power supplies, which have the size and weight of 366 x 254 203.2 mm and 13.61 kg respectively. The power supplies were change to two small chassis power supplies; +/-15V and +/-5V. Both of these power supplies were manufactured by Traco. These Traco power supplies have improved in both the size and weight of the power supplies, with the weight of 200 g and size of 63.8 x 112 x 29.6 mm for one chassis.

During the setup for experiment under the furnace, a tedious task was to connect each of the connection and also moving the equipment from one location to the other. Hence, the bench top signal generator was replaced with a PXI function generator, PXI-5406. This generator was able to generate sine and square waves at frequencies up to 40 MHz. With this plug-in signal generator, it is easier to control and synchronise with the digitisers by using the LabVIEW software as the hardware is clocked simultaneosly for all the cards plugged in in the system.

With the desktop as the host computer, the system is not able to be relocated easily without switching the computer off and unplugging it from the mains as well as from other instruments such as the PXI system. Hence, it requires more time for resetting up at different

locations. During the experiment, before taking any measurements, the instruments are left to be warmed up to prevent any drifts due to the instruments. Therefore, by switching the computer off, it may require a repeat procedure to allow the instruments to warm up each time. To allow a more portable system, the desktop computer was replaced with a laptop, Dell Vostro 3560. A PXI-8360 express card is used to link the PXI system with the laptop.

Since the laptop does not have a parallel port by default, modification in the system to switch the relays and shut down function on the power amplifier was made. An additional interface, a NI USB-6009 with the size of 81.8 x 85.1 x 23.1 mm and weight of 84 g was added into the system to replace the switching controller. The NI USB-6009 has 8 single ended (or 4 differential) analogue inputs with 48 kS/s sampling rate, 2 analogue output channels and 12 digital bi-directional channels. The digital bi-directional channels are able to output 5V, with 102 mA. Eight of these digital channels were used for programming into an output channel, which was used to control the switching in the system.

The multimeter was used to measure and monitor the temperature at the sensor head. Temperature monitoring is able to avoid overheating the equipments during experiment under the furnace. In the electronics board, two temperature sensors (LM35 with SOIC package) were fixed at two ends of the board. However, the temperature monitoring task is limited to take only one side of the measurement due to the limitation of having just one input for the multimeter. The upgrade of replacing the multimeter using this NI USB-6009 for temperature measurement enables both of the temperatures to be monitored at the same time.

The improved acquisition system was formed by equipment with smaller sizes and lighter in weight. To cluster all of these instruments into a single, portable self-contained air cooled system, a 19" 6U case was designed to enclose all of these instruments. Four 120 mm fans as shown in Figure 71 and Figure 72 were fitted at the front and back panels of the enclosure to allow air flow in the box.
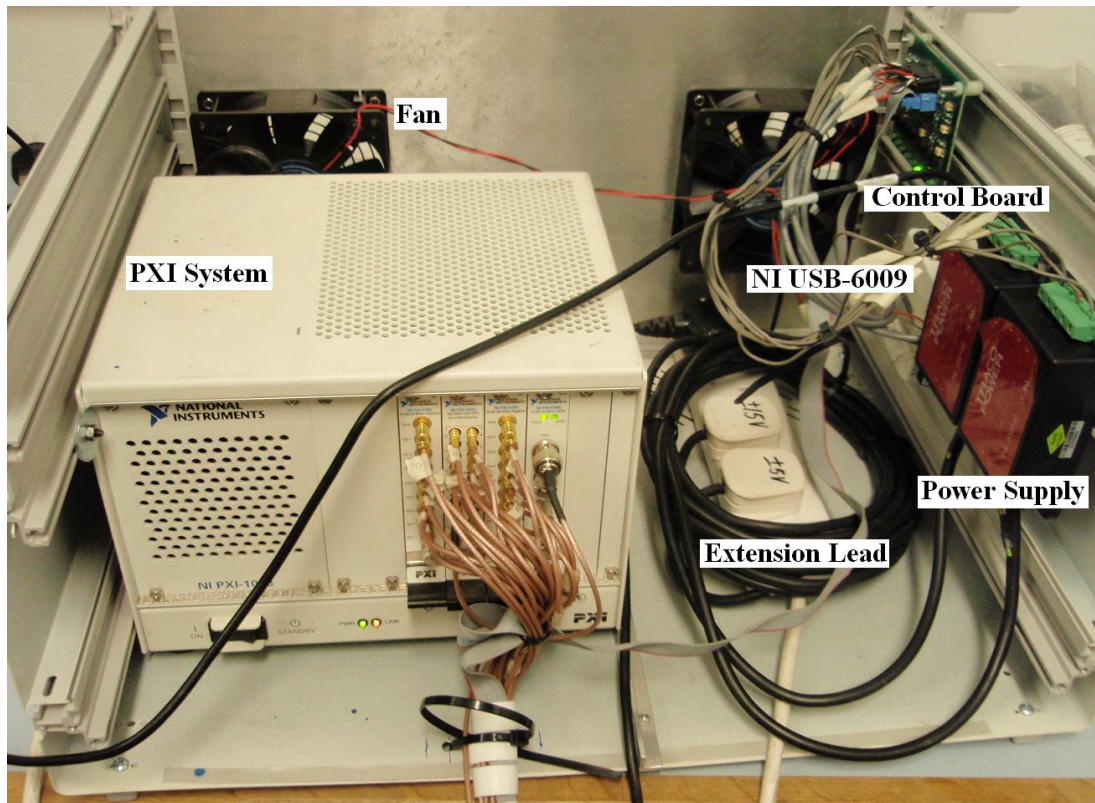
Figure 71 Insight of self-cooling instruments enclosure
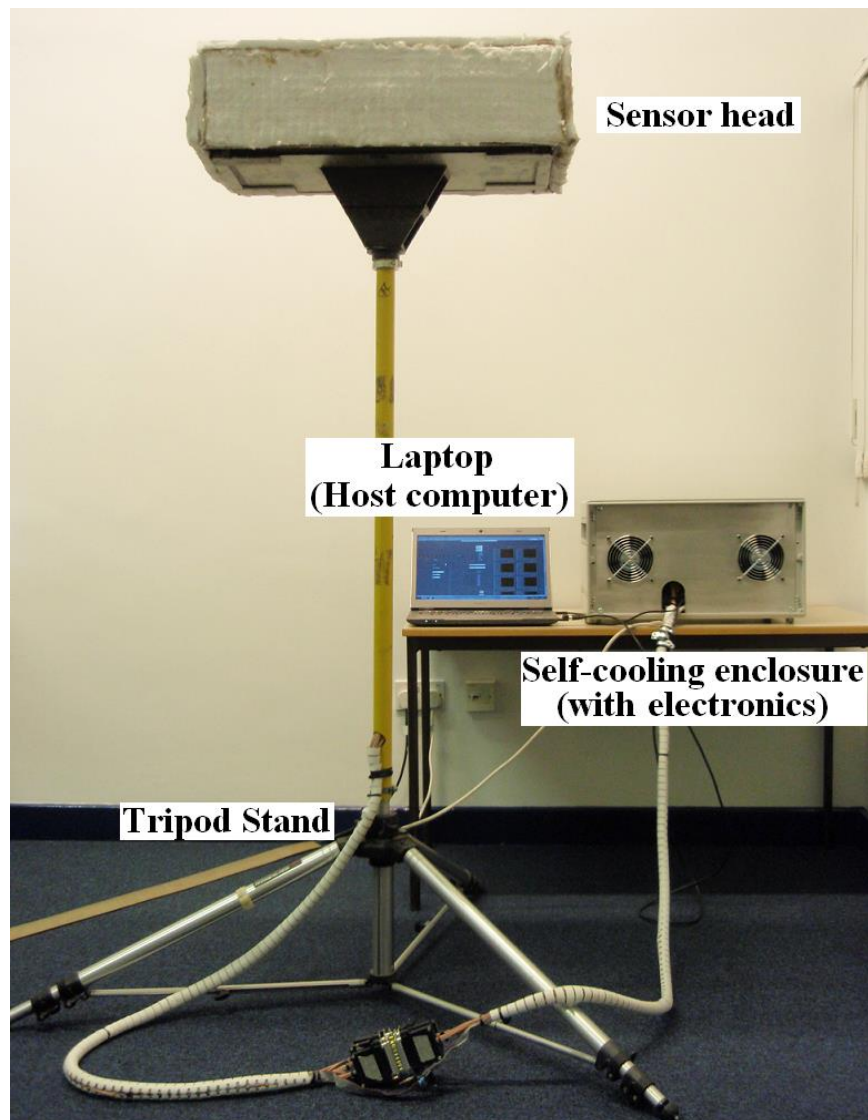
Figure 72 Acquisition system with laptop, self-cooling enclosure and original sensor head

5.4   Conclusion

To produce reliable sensing equipment for measurement in the hot environment under a glass production furnace, the steps in selecting electronics is crucial. In this chapter, electronics and circuits are tested carefully to monitor their response towards temperature. This is to reduce the possibility of temperature related drift in electronics that will affect the signal. However, after comparing and finalising the circuit channel by experimenting with one transmit and

one receive coil, 8 identical circuits were fabricated on a single long board. The board was shielded with top and bottom screens, giving a three layers sandwich design. To produce a sensor that has a minimum weight, the board comes with the long background tracks for signals and power supplies, reducing the needs of cabling. This has significantly introduced crosstalk and pushes the design to use cables for signals and power supplies instead.

For a better portability, the data acquisition hardware has successfully reduced to 3 units, containing a laptop, sensor and the self-cooling enclosure (with electronics). To reduce the weight of the enclosure, a cut-off method was introduced for the enclosure walls. Although the walls were thinned down, the strength and stiffness of the wall was still able to be maintained. A new sensor head is proposed as the original sensor head was too heavy for operation over the head for the operating staff. This sensor head has significantly reduced the weight to half of the weight of the original sensor head.

Chapter 6 Acquisition Software

6.1   Introduction

A PXI data acquisition unit (also referred to here as the PXI system), manufactured by National Instruments, was used in this research. As introduced in the previous chapter, the PXI system is divided into software and hardware. The software was coded in LabVIEW and was used to control the hardware units and record measured data for subsequent analysis.

LabVIEW is a virtual instrument that uses graphical programming to control the instruments, data acquisition and to analyze data. The system can be control easily by programming in blocks in LabVIEW without requiring a highly skilled programmer. It enables the development of a graphical user interface (GUI) which can control the measurement process, scanning control, device setup and specification and etc. In this project, software was developed for the use of collecting data, channels switching controller, temperature acquisition and generating multi-frequencies excitation signals.

A multi-function program to control the equipments was developed to control the 2 digitisers modules (PXI-5105), a multiplexer module (PXI-2593) and a signal generator modules (PXI-5406, which was upgraded later in the project). Apart from controlling the PXI system, this software was used to drive the rest of the equipment such as a bench top signal generator, parallel port, a NI USB-6009 multifunction data acquisition system (DAQ), and a bench top multi-meter.

The PXI-5105 is a digitising module with 8 simultaneous sampling channels, which allows the input signal ranges from 50 mV to 30 V. This instrument enables a virtual selection for the input impedance of 50 Ω or 1 MΩ. For the front end electronics, it has 8 receiving channels and 8 transmitting channels, hence, 2 of these modules were required.

The multiplexer, PXI-2593 was used to output the sinusoidal signal to the selected transmit channel. This multiplexer has 18 channels that are fully controlled by software. It is capable of handling signals with frequencies from DC to 500 MHz. The 18 channel module which has two connections for input (COM 0 and COM 1), can be flexibly configured with 16x1, dual

8x1, quad 4x1 sparse matrixes or any size in between, depending on the application. It is also possible to connect different cross point configurations simultaneously.

There were several upgrades in the hardware units for the acquisition instruments as described in the previous chapter. The desktop computer was upgraded to a laptop computer; hence, the parallel port originally used was replaced with a multi-function DAQ, NI USB-6009. These instruments were able to supply up to 5 V to switch the necessary channels. As the name of NI USB-6009 suggests, the unit was connected to the laptop computer via a USB interface. This DAQ system comes with 4 differential / 8 single ended analogues input which the voltage range of -10 V to 10 V. As the temperature sensor, LM35 outputs 10 mV/^{o}C to indicate the temperature of its surrounding, it allows the same instrument to be used for measuring the temperature, hence, eliminating the need of a bench top multimeter. A PXI platform signal generator, PXI-5406 was used as a replacement for the original bench top signal generator (HP Agilent 33220A). This signal generator module is able to produce signals up to 40 MHz. Controlled by the virtual platform of LabVIEW; it comes with selection of 50 and 75 Ohm output impedances and a 100 MS/s sampling rate.

6.2 Software Design and Measurement Strategies

6.2.1 Input Control

When building the GUI in LabVIEW, the controls and indicators are located on the front panel. The structures of the controls are separated in another window called the block diagram. The GUI designed in this project allows the changes of parameters for measurement easily without having to change the code of the program.
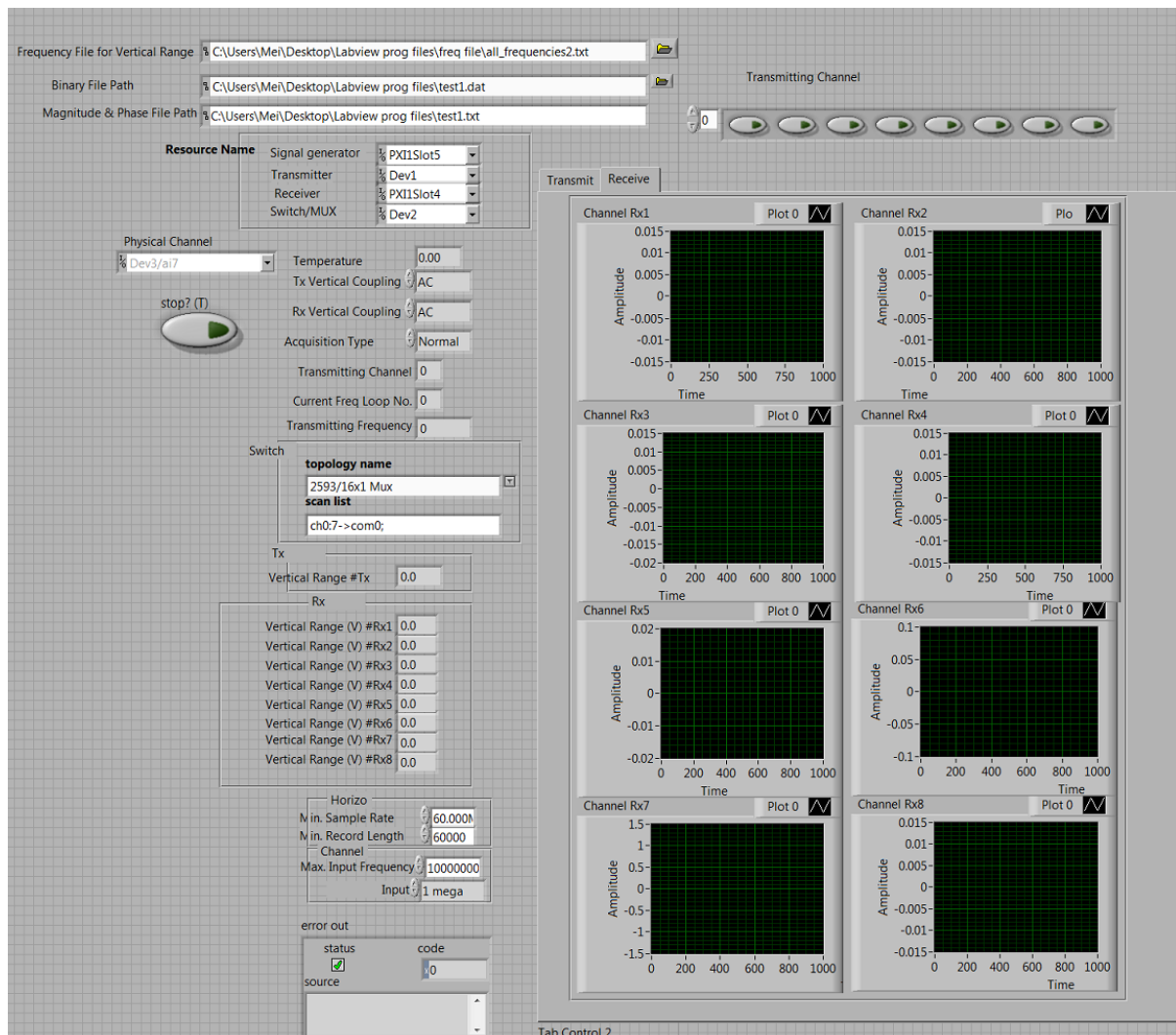
Figure 73 GUI for data acquisition system control

The GUI for the data acquisition system is shown in Figure 73. By using this program, it provides a high degree of flexibility where it acts as an input and output controller at the same time. This allows an easier modification on the input parameters as well as eases the user in visualising the real time graphical results. To reduce the setting time of the measurement parameters for every experiment, files contain the information of the parameters, such as the vertical range of the input and output signals, input signal voltage for the signal generator, frequency etc were saved to the hard drive to be loaded during the experiments.

6.2.2   Digitising

By inputting the vertical range of the signal, the PXI-5105 digitisers are able to digitise the analogue input signal on the PXI system more efficiently than relying on the devices auto-scaling. The sampling rate was set to 60 MHz. By applying a dot product function to the digitised signal with a virtually generated signal in LabVIEW, the real and imaginary components of the demodulated phasor could be obtained, which can be readily converted into phasor magnitude and phase. This algorithm was applied to all the signals on the inputs of the digitiser modules, allowing the transmitting and receiving signals to be compared, and to obtain its difference in magnitude and phase for both signals.

As the PXI system has the ability to demodulate more than one input simultaneously, the signals on every transmitting and receiving channel were recorded at the same time. This allowed 7 receiving signals to be measured in parallel when a transmitting circuit was operating. As a result, 56 mutual coupling impedance values could be obtained from the complete sensor array. The value of the mutual coupling between the same coil pairs are assumed to be the same due to reciprocity, for instance, the impedance value of coil 1 as transmitter and coil 3 as receiver is assumed to be equivalent to the impedance value of coil 3 as transmitter and coil 1 as receiver. The measurements of the coil pair that are next to each others are ignored due to their sensitivities towards the target are low. Therefore, only 21 values for each frequency were used for analysis.

The Agilent Technologies 34401A multi-meter was controlled by the GPIB-USB interface to indicate the temperature for each cycle of measurements. Only one measurement was taken due to the limitation of inputs. With the multi-functions USB-6009 DAQ, two measurements or more could be taken simultaneously for the temperature on the sensor at different locations.

6.2.3   Channels Switching

The system operates by measuring the impedance of the coil pairs with the sequence of switching the transmitting channel from channel 1 to 8, for 2 cycles, and then the frequency is changed to the next value. This process is repeated 9 times since 9 frequencies were used in the experiment. Hence, the synchronisation for three of the main switching mechanisms is

important. As mentioned earlier, the parallel port was used to drive the relays in the circuit. The multiplexer PXI-2593 was controlled to switch the excitation signals to the system at the same. To synchronise the switches of channels simultaneously, the clock for every switch is set to be 500 ms, which in theory is 4 seconds for switching 8 transmitting channels, per frequency cycle. However, the switching takes approximately 12 seconds for one cycle of measurement in reality. The longer period of time may be due to the large amount of data are processed simultaneously.

The parallel port is used initially as it is an economical way for data acquisition system control for the relays and power amplifiers. It does not require additional investment with desktop as the host computer. However, the upgrade to a laptop has resulted in the replacement of the parallel port with NI USB-6009. The same configuration in software is designed by having the relays and power amplifiers controlled by this DAQ unit.

6.2.4   Input Signal

Considering the multi-frequency system is able to provide more spatial data for data analysis, the input waveform has to be programmed to different values for its frequency and amplitude. The frequencies chosen were 500 kHz, 600 kHz, 700 kHz, 800 kHz, 1 MHz, 2 MHz, 4 MHz, 8 MHz, and 10 MHz. For the beginning of the project, a bench top, HP Agilent 3322A signal generator was used. The LabVIEW software was able to communicate with signal generator via the GPIB - USB interface. The values of the amplitude, frequencies were pre-stored in a text file for automatic update of the settings during measurements. This procedure is also applied for controlling the parameters of the upgraded PXI-5406 signal generator module.

6.2.5   Synchronisation

The accuracy of synchronisation between modules and equipments was unknown. Therefore several tests and experiments were applied to the system. The accuracy of synchronisation between channels on a single digitising module of PXI-5105 was analysed. A 1 MHz, 2 V_{pp} sinusoidal waveform, which was generated from the bench top signal generator was inputted into two of the inputs of PXI-5105 in a single module, and repeated on different sets inputs

on the same module. The phase differences in rms between the inputs pairs are found to be 2 to 5 millidegree.

Then the same test was carried out to analyse the accuracy of synchronisation between the two identical modules, which fitted into the same chassis. The signal from the signal generator was connected to one input each, on both of the digitising modules. The difference in phase was measured and the tests were repeated for different input pairs to obtain their phase differences. The rms phase differences was found to be between 4 to 7 millidegree, which shows that the synchronisation is less precise for different modules when compared with the values in the previous paragraph.

6.2.6 Data Storage

When the measurement is finished, the system sends the analysed readings to be recorded and stored in a text document (.txt). It gives a total of 130 columns (or 131 columns for two temperature measurements) and 18 rows of data for a complete cycle of 9 frequencies measurement. The mutual couplings impedances are recorded separately for magnitude and phase difference in each column. However, the results will have one pair of valueless readings; which are the magnitude and phase for the mutual coupling between the coil pair from the same channel itself. These results as well as the coupling between neighbouring coils results can be eliminated in the program for inversion. Depending on the number of temperature taken, the last or last two columns for each cycle is / are used for saving the temperature reading of the measurement cycle. The column before the temperature is used for storing the excitation signal frequency. For each row of the data, it represents 1 frequency. For each frequency, the measurement is repeated. Hence, there are 2 rows of reading for each frequency.

The algorithm for demodulating the raw sinusoidal signals into their real and imaginary phasor components in LabVIEW was unknown. Due to the uncertainty of the reliability of the default functions in LabVIEW in producing magnitude and phase, the raw data of the waveforms are stored as a separate file. The data is able to be evaluated with MATLAB to obtain its phase and amplitude. The MATLAB program is a numerical computing tool; it allows matrix manipulations, the plotting of data, creation of GUI and etc. As the raw data

saved in LabVIEW are in binary form, an intermediate medium was coded in Visual Basic, Microsoft Visual Studio to convert the binary file (.DAT) into MAT file (.MAT). Figure 74 shows the interface of the file converter system.
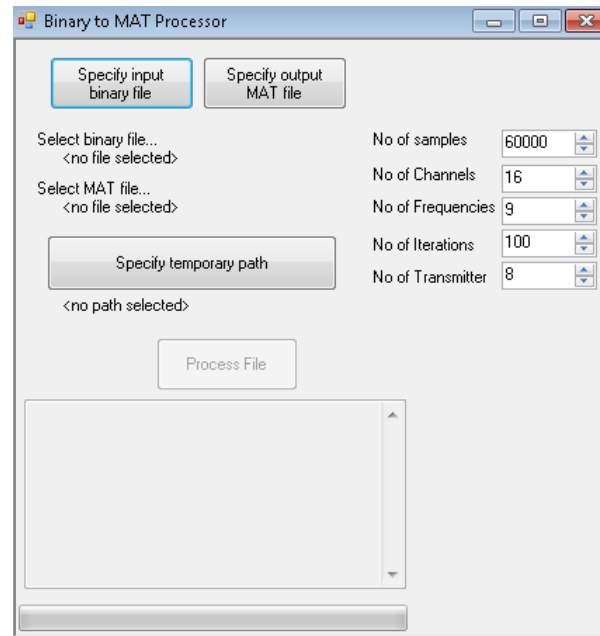
Figure 74 GUI for binary to MAT file converter

6.2.7   Output Display

The design of the GUI in Figure 73 provides the real time monitor of the signals on the screen. It eases the parameters setting and troubleshooting process as it allows user to observe the shape of the signal; ensuring that the signals are not distorted. It also provides a simple indication during the experiment if any of the circuitry stops functioning and does not produce a sine wave.

There are 2 tabs in the display screen. One tab shows the transmit signals and the other tab shows the receive signals. Each tab contains 8 windows, with each window indicating one channel. When the electronics are switched on, all of these windows are displayed at all the time regardless of its state; whether it is switched on for transmitting or receiving or switched off. Since the same channel will not be transmitting and receiving at the same time, therefore, when one window is showing signal as transmitting, the receiving window for the same

139

channel will be displaying random signals or noise. The windows are deliberately left as displaying noise because this helps the user to monitor the system for the existence of crosstalk between channels as well as monitoring the noise levels.

The output of the parallel port / NI USB-6009 are connected to the sensor circuit with a ribbon cable via an intermediate control board. The software programmed is design to have the same LEDs indicator on the display screen as the intermediate control board. This is to provide a reference for user to have visual understanding of which channel that is transmitting signals at that particular instance.

6.3 Conclusion

The current data acquisition system is controlled by LabVIEW software. It is flexible to program for the desired data to be measured and recorded, as well as inputting different parameters automatically for the measurement setup. This allows a quicker measurement at the hot environment and for the data to be analysed offline.

Switching between channels for signals connection is important to prevent signal leakage into the system, preventing it from causing inaccuracy data in the experiment. The software design has put this into consideration by allowing the same clock for switching the relays, power amplifier and multiplexer at the same instance. Apart from that, the GUI also allows the signal behaviour for each channel to be observed during operation. By having the windows for each channel, the user can monitor the signals all time, to observe any existence of crosstalk or appearance of undesired signals.

The multiple chassis of the PXI system has a benefit for the system by reducing the number of external equipment containers to be carried around during the furnace tests. Although the system is able to obtain reading instantly once it is switched on, it is always a good practice to leave it to be warmed up for approximately 30 minutes before experiments, to reduce any drifting in signals and also to ensure good repeatability of results can be obtained.

Chapter 7 Experiments and Measurements

7.1   Introduction

The previous chapters have shown the details of the construction of the electronics by analysing individual performance of the component blocks and the program designed to control the data acquisition system. Although the tests carried out show the stability of the electronic blocks individually, it is important to ensure that the system is able to provide accurate response in practical situations. The experiments were carried out initially in the laboratory environments (room temperature) with a laboratory tank in the University of Manchester and a test rig installed by Pilkington at St. Helens. Then, hot online trials were carried out on UK6 Pilkington at St. Helens before it was due to shut down for repair.

The main challenge for the project is to operate the system in the harsh environment of the furnace with the presence of steel beams around it. As shown in the simulated results, the magnitudes of the signals are found to be sensitive to the steel structure dimensions and distance. Apart from that, the magnitude changes according to the variation of conductivity. It is almost impossible to obtain the actual conductivity of the molten glass, as it varies from point to point throughout the refractory, hence, only the phase change will be use in this chapter to compare the experiment data with the simulated results from the Maxwell® v15 FEM simulator.

7.2   Measurement Techniques

The 8 pairs of sensing coils were constructed on a double sided PCB material as shown in Chapter 5. According to the proposal of Dodd and Deeds, the effect of steel is much less at high frequencies; hence, it is an interest in this project to use a multi-frequency setup to eliminate the steel effects. Each of the sensing channels was connected to the PXI system with 3 RG316 coax cables. The lengths of the cables are 3 meter each. Salt was added into tap water to obtain saline with similar electrical conductivity to represent the molten glass for the purposes of the experiments. Every 7.4 g of salt will increase the conductivity by

approximately 1 Sm^{-1} for 1 litre of water. The saline conductivity was also measured by a conductivity meter, (Hana HI8733).

Initially, the sensor was tested in the laboratory. A tank with the dimension of 450 mm x 620 mm x 420 mm was used as the vessel to contain the saline. However, this laboratory test tank was not able to provide the complex steel configuration as the furnace structure. It was only able to provide the general estimation for the outcome of the experiment. In Figure 75, the setup of the experiment in the laboratory in the early stages of the project is shown. The sensor was placed in the cabinet below the tank. The cabinet is able to give a stable distance between the coil and the tank, and the lift-off level can be adjusted with the internal hooks which hold the cabinet divider shelf.
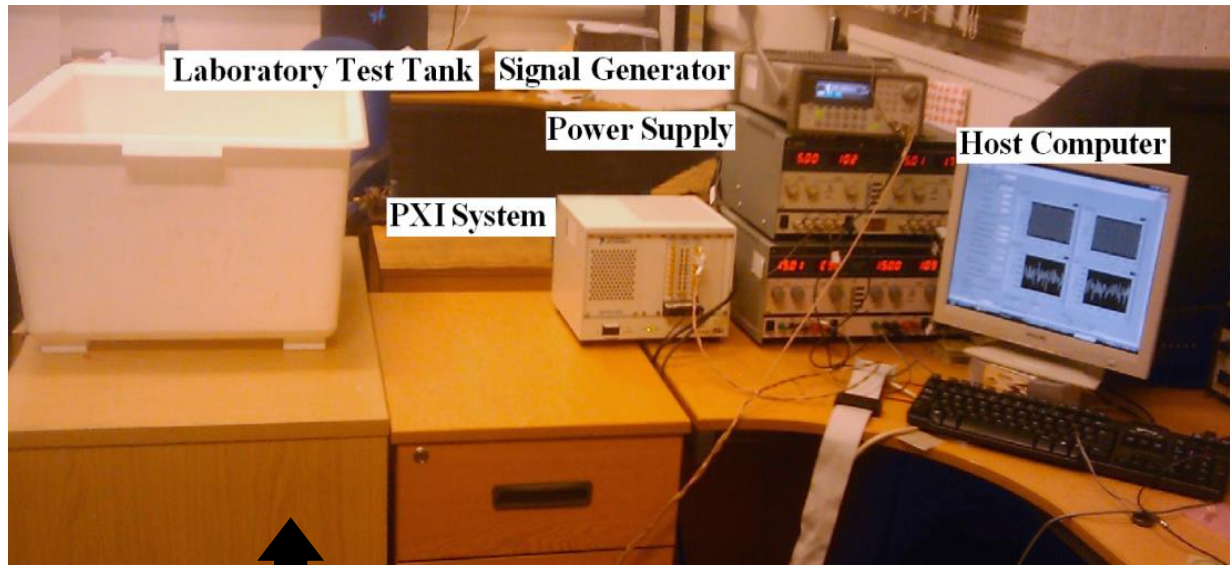
(a)
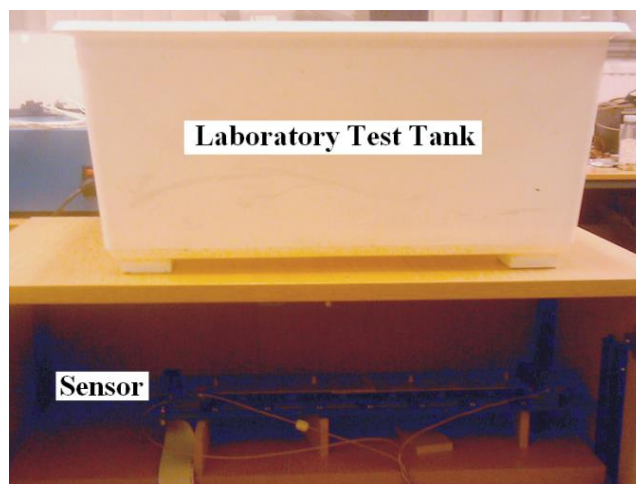
(b)

Figure 75 Laboratory experiment setup
(a) Position of equipments
(b) Position of tank above the sensing electronics in the cabinet

However, the laboratory tank is very small in size compared to a real furnace; therefore it was unable to provide a very good analogue as the small volume of saline in the tank will induce a very small eddy current. Therefore, the trial was repeated in a test rig which contained a higher volume of saline and which will give a higher signal during the test. The test rig was

constructed by Pilkington and designed by Zysko [1]. It was a setup that follows the geometry of the furnace, as shown in Figure 3.
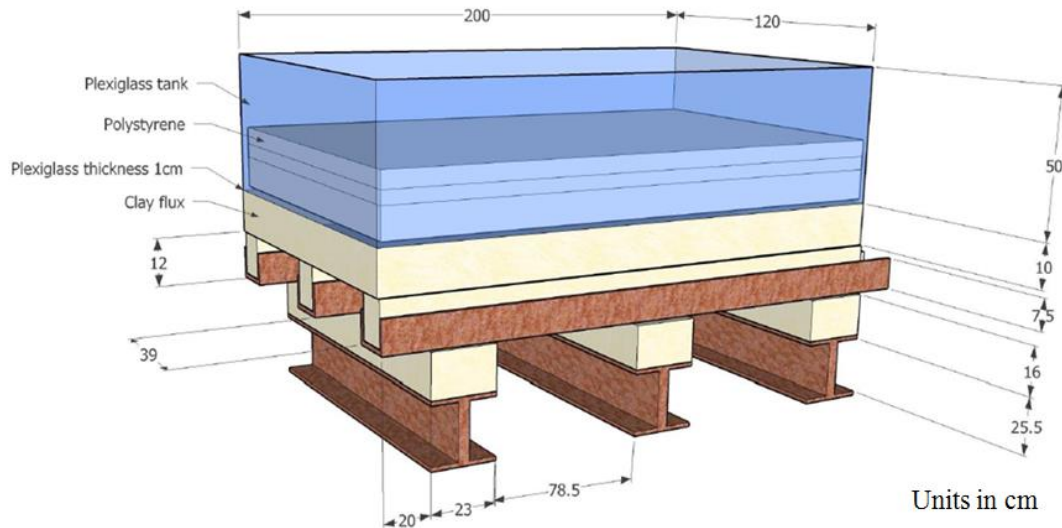
Figure 76 Test rig dimensions designed by [1], located at Pilkington, St Helens.

The saline container was made from Plexiglass, 10 mm thick. As shown in Figure 76, this container sits on the clay flux blocks that are supported by the steel U beams and I beams. This allows a controlled environment for experiments, ensuring that it is at its optimum state before it is tested under the furnace.

As shown in the Chapter 5, a wooden housing was used for the initial experiment to hold the front end electronics. In the test rig, a wooden holder was made to ease the sliding action for the bottom housing for the measurement under the saline container. This provides an accurate positioning tool for the sensor. This holder were designed to allow the sensor to go with one direction and making sure that the position for its left and right as well as the height remains the same.
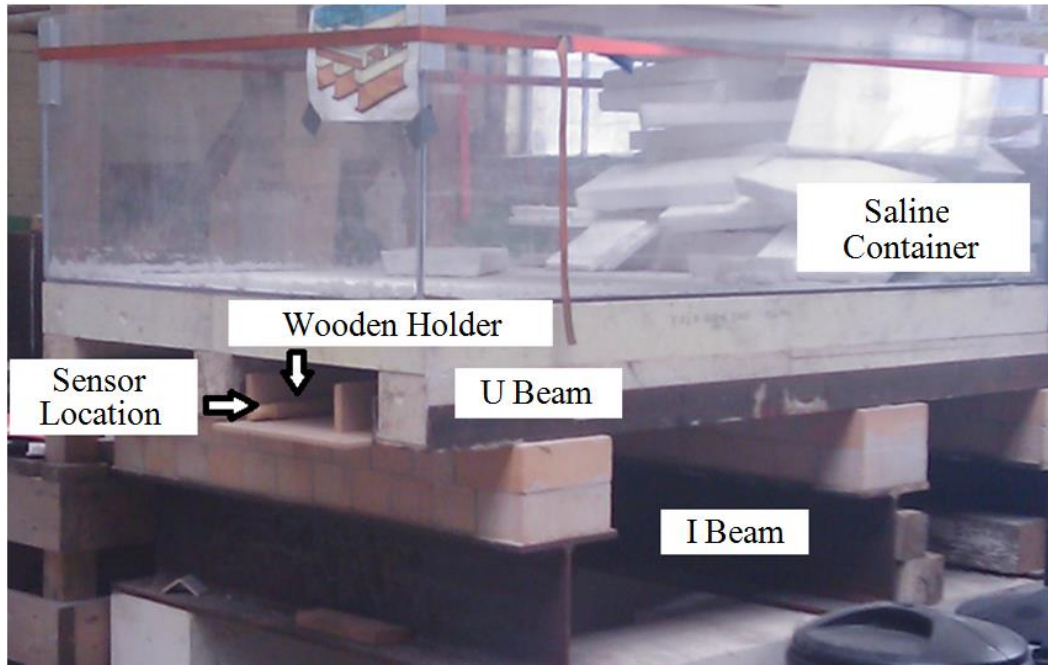
Figure 77 Test rig with steel supporting structures

7.2.1 Stability and Sensitivity of the System

The time for the sensor to achieve equilibrium, with no drifting on the signals was studied. For repeatability, instruments are usually left to warm up for it to achieve an equilibrium before taking measurements. However, in this case, the pre-warm up for the overall system does not reduce the drifting time of the system. When the sensor was left to operate with the same transmitting channel, the signal drifted up to 150 millidegree over a 2-3 minutes time period. A similar characteristic appeared every time the transmitting channel was switched.

Since the time for each channel to achieve its equilibrium takes at least 2 minutes, therefore, for 8 channels, it would requires at least 16 minute for the signals to stabilise. This figure does not include the measurement time. It was found that when the transmitter switches, the signal always start at the same point. Hence, an alternative method is to switch the transmitting channel continuously, in a scanning mode which scans through the 8 transmitting channels. It takes one measurement for all receiving channels at a time then switch to the next transmitting channel, instead of taking continuous measurements by

transmitting with the same channel. This will leave the system with insufficient time to start drifting. This scanning technique successfully maintained the readings without drift and only scatter around the noise level. Therefore, the sensing system was designed to have a dual set of transmitter scanning mechanisms.

The individual noise levels were analysed and it was found that as the distance between the transmitting and receive coil pair increases, more noise was introduced into the system, from 5 millidegree (coil-12) to approximately 46 millidegree (coil-18) at 1 MHz. The rms values of the noise signal were also affected by the volume of conducting material and the operating frequencies. Signal-to-noise (SNR) ratio was calculated with Equation 37.

$$SNR = 20\log(\frac{\Delta S}{N_{RMS}})$$

Equation 37

where

$$N_{RMS} = \sqrt{\frac{1}{n}\sum_{i=1}^{n}(x_i - \bar{x})^2}$$

Equation 38

where

N_{RMS} : RMS value of noise

ΔS : Difference of signal between freespace and conducting material

n : Number of samples

x_i : Value noise sample

$\bar{x}$: Average of noise samples value

The measurement for this signal-to-noise was taken in the test rig. The distance of the coil pair was 538 mm, which is the coil-17 in the coil array arrangement. Saline with conductivity of 13 Sm^{-1} was used. In this measurement, 50 samples were taken for each frequency from 100 kHz to 10 MHz. The SNR measurement was plotted in Figure 78, the SNR value is more than twice at the frequencies near 1 MHz compared to the SNR for the lower and upper range of the frequencies.
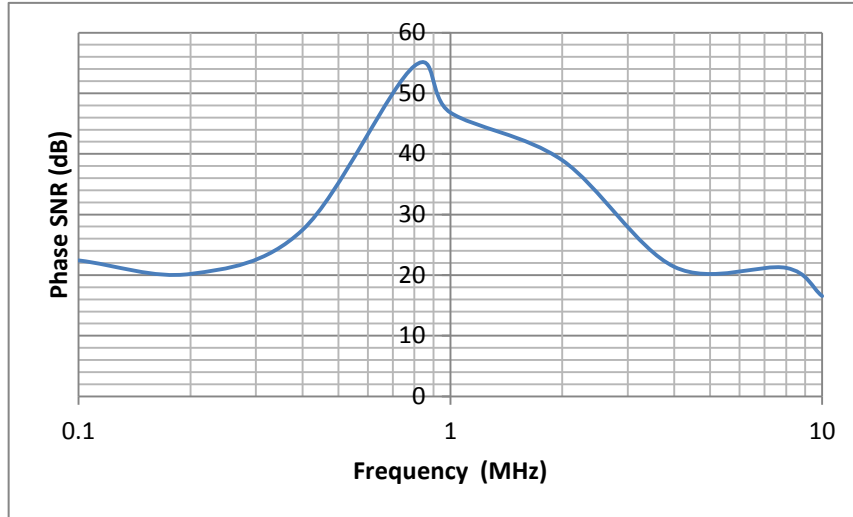
Figure 78 SNR of the sensing system

7.3   Cold Experiments

7.3.1   Conductivity

Variation of the temperature in the refractory will consequently causes the change in the conductivity of the molten glass. As shown in Figure 8, the conductivity is not directly proportional to the temperature change. For the temperature which was monitored and provided by NSG European Technical Centre, The molten glass in UK6 furnace is between 1148 ^{o}C to 1245 ^{o}C. Hence, for this range of temperature, every 25 ^{o}C of increment will increase the conductivity of the molten glass by 1 Sm^{-1}.

A laboratory test was performed to analyse the stability of the phase signals towards the change in conductivity of saline. Since the dimension of the laboratory tank is small and with similar size of the length of the sensor array, it is expected to introduce more noise in the signals. As a result, only four coil pairs were used in this test, with coil 1 as transmitter and coil 3, coil 4, coil 5 and coil 6 as receivers. The individual distances from the centre point of these coil pairs are 156 mm, 234 mm, 312 mm and 398 mm respectively. The distance between the coil array and the saline was 275 mm and the depth of the saline was 100 mm. To represents a 25 ^{o}C of change in temperature, the conductivity of the saline was varied from for 11.5 Sm^{-1} to 12.5 Sm^{-1}. The conductivity may have an error of +/-0.2 Sm^{-1} because

the conductivity reading was not constant when the meter was tested at multiple spots in the saline tank. This may be due to the concentration of salt are not be dissolved completely and thoroughly. Hence, an average reading of the conductivity was used in this experiment.
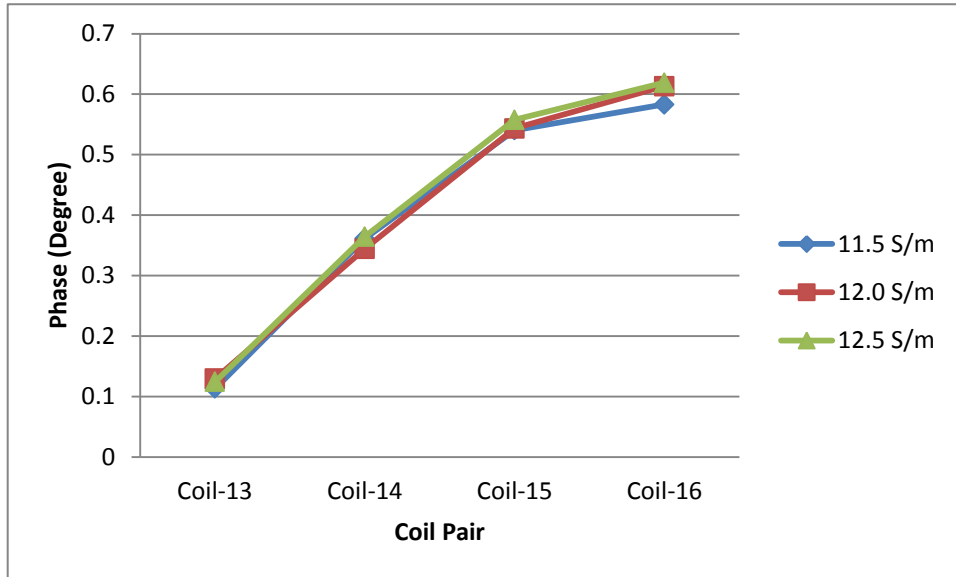
Figure 79 Effect of conductivities in phase with distances of coil pairs of 156 mm, 234 mm, 312 mm and 398 mm

As indicated in the graph of Figure 79, the signals between each conductivity line are at a similar range of values, with the maximum difference of approximately 40 millidegree. This difference becomes more significant as the distance between the coil pair increases, which may be introduced by the noise, which also increases with distance. As shown in Figure 86(b) later in this chapter, by comparing the simulated results with the experiment results; the experiment results for the laboratory tank have a high noise level, which similar to the noise level in this experiment.

7.3.2   Frequency Response

To construct a system with multi-frequency signals, the accuracy over the operating frequency range is important. The sensor was placed under the test rig with a lift-off of 324 mm to the saline. The conductivity of the saline was 14 Sm^{-1} with the depth of 90 mm. The frequencies response for coil-14 and coil-17 are shown in the following figures.
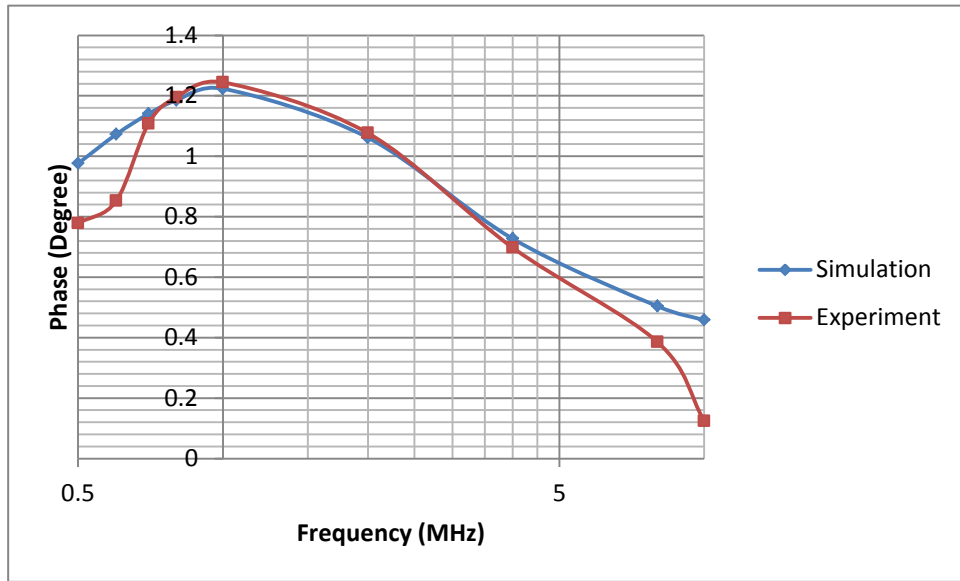
Figure 80 Frequency response for frequency range of 500 kHz to 10 MHz for coil-14
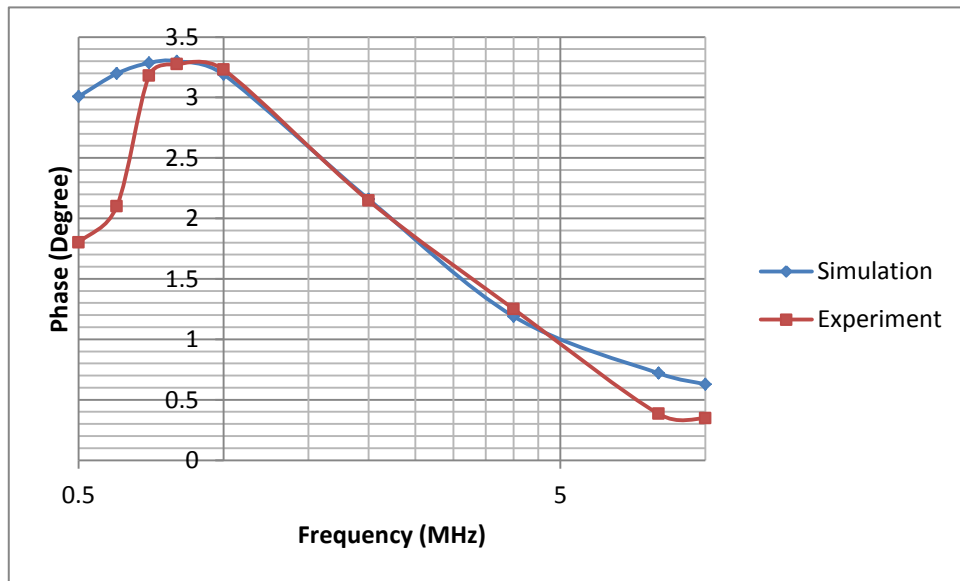
Figure 81 Frequency response for frequency range of 500 kHz to 10 MHz for coil-17

The frequencies of 500 kHz to 10 MHz were used in the test. Both graphs show similar characteristics, which can be separated into three parts. For frequencies below 700 kHz, the experiment results deviate from the simulated results significantly. As the frequency

increases, the deviation of the signals decreases and the simulated data matches the experiment results. Above 4 MHz, it is noticeable that the signals start to deviate again from each other.

For frequencies that are lower than 700 kHz, the system is more prone to noise at lower frequencies. Whereas for higher frequencies, as the sampling rate is limited to 60 MHz in LabVIEW program, the number of samples may be too low for an accurate analysis. Apart from that, the voltages at the receiving coil at high frequencies are very low. This will greatly reduce the sensitivity of the coil in picking up the signals. With the support of these two graphs, it indicates that the frequencies that give reliable data are range between 700 kHz to 4 MHz.

7.3.3   Steel Effect

The structure of the furnace steel supports was not build with very high dimensional tolerances and it is expected that the relative position of the supports may vary by the order of a centimetre from location to location. Therefore, the effect of the steel beams on the signal is important. Hence, a test was carried out by moving the U beam in the test rig by 30 mm. However, this test is only able to move the beam once since it is supporting the Perspex saline container, which causes it to be too heavy to move for the beam and the container together. The original distance of the U beams was 390 mm, a measurement was taken at this point, and then it was moved to 420 mm. During the experiment, the sensor location was not moved and it was aligned to the stationary U beam on the right, moving just the beam on the left. The distance of the saline with the coil was 194 mm, with a saline depth of 100 mm. The conductivity of the saline was set to be 14 Sm^{-1}. Figure 82 shows the comparison of the simulated results with the experimented results.
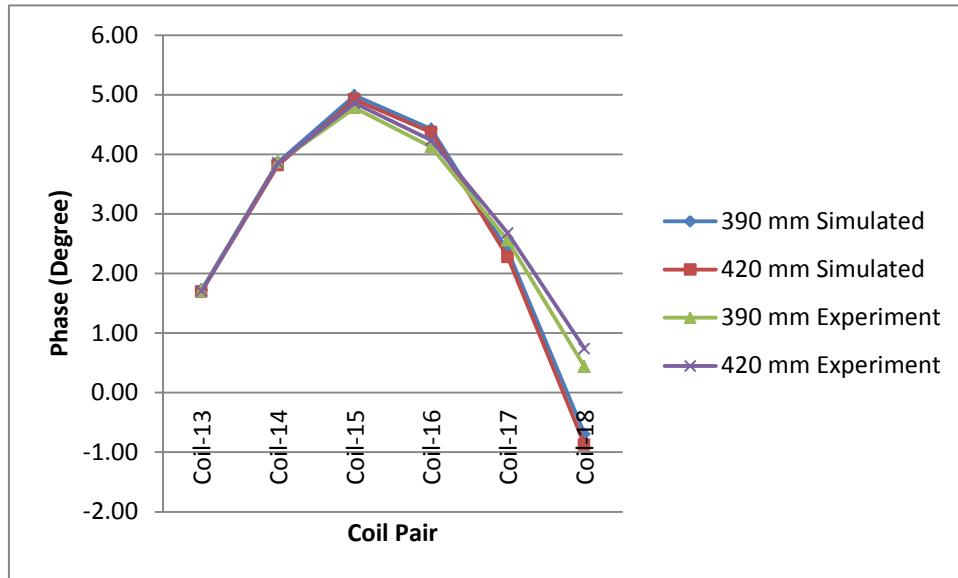
Figure 82 Effect of U beams movement in phase

As shown in the data, the simulated results for both of the distances, 390 mm and 420 mm are similar regardless to the movement of the U beams. The data of the simulated and experimented results are closely matched with each other when the coil pair distances are closer to each other. As the distance increased, the experimented results deviate from the experimented results. However, although the results deviate for approximately 1 degree in coil-18, both of the experimented results for 390 mm and 420 mm data are still closely following its own trend. The difference in simulated and experimented results may be caused by the error in the modelling or the noise in the system.

7.3.4   Grillage Structure

The structure of the furnace often varies from one site to another. A modern furnace structure was shown in Chapter 2. However, a furnace is usually built to last for 15-20 years, and repairs are common to extend furnace life. Therefore, there are still old furnaces that are still in operation. The old furnaces were designed to have grillage in the supporting structure. As the steel will deform the transmitting field, it is a challenge to apply the technology in this project into the furnaces that have grillage installed.

An experiment was carried out with a grillage panel with the dimension of 130 mm x 650 mm x 30 mm (as shown in Figure 83). The grillage was placed between the coils and the saline in the laboratory tank. This setup allows the analysis of the grillage without other steel effects such as the U beam and I beam in the test rig. The distance between the sensor and the saline was 275 mm. The conductivity of the saline was 10 Sm^{-1} with 100 mm depth. Two frequencies were used for this analysis, which are the 1 MHz and 4 MHz signals.

Figure 83 A cut out grillage panel from the furnace
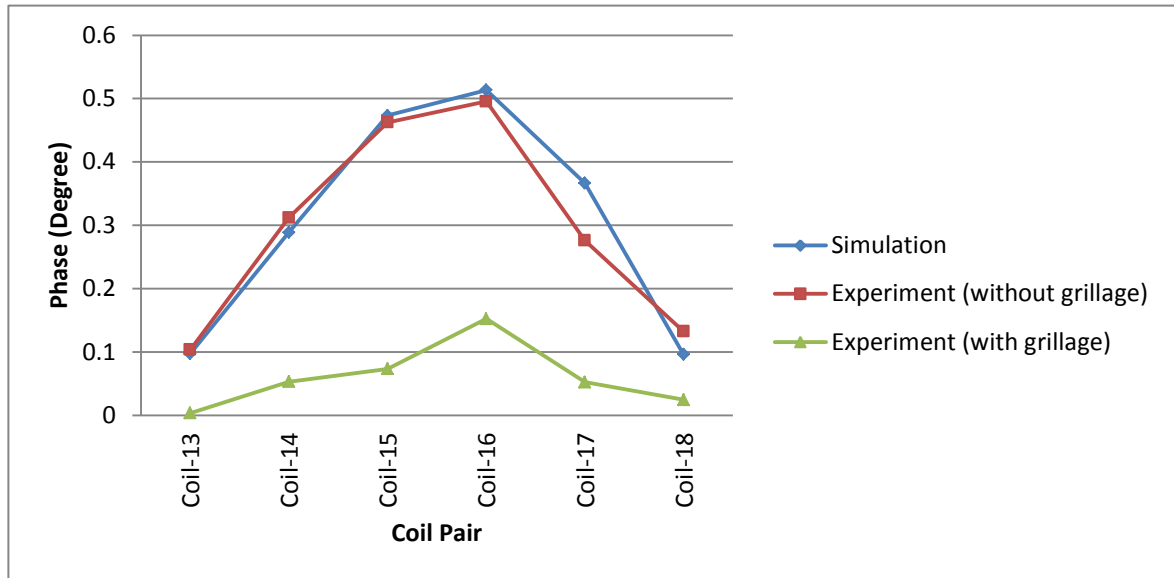
Figure 84 Effect of grillage in phase for 1 MHz signal
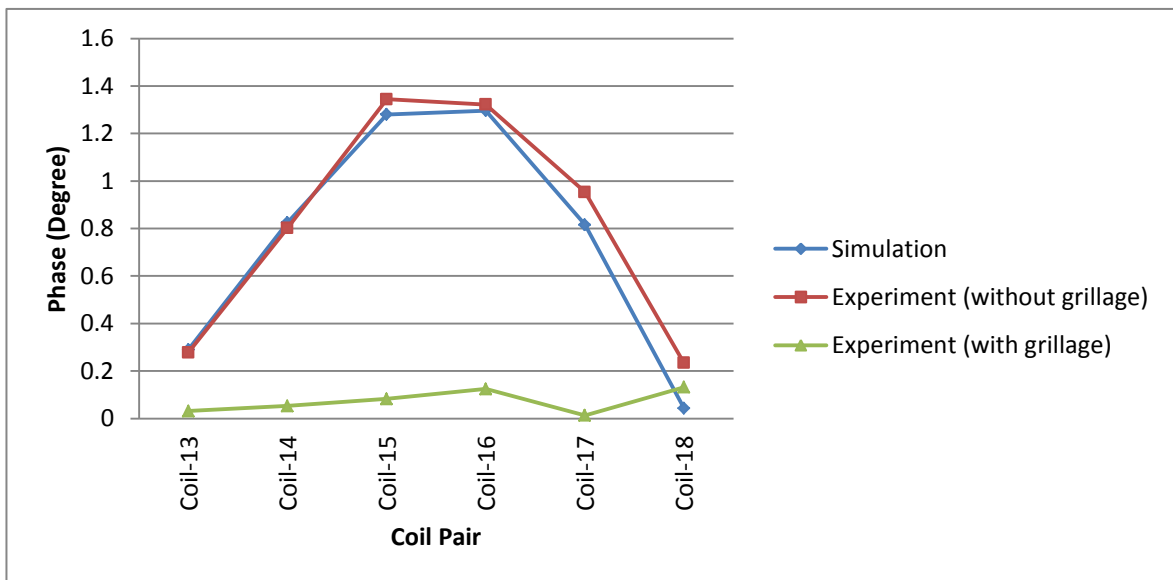
Figure 85 Effect of grillage in phase for 4 MHz signal

As illustrated in Figure 84 and Figure 85, the grillage has effectively shielded the signals from passing through it; hence, with the presence of the grillage between the coil and the target, no useful signals were obtained for both of these frequencies. This indicates that the sensor is not usable in furnaces that are covered with grillage. However, it may be possible to obtain results by cutting an opening at the grillage in the furnace. The disadvantage of this method is that it is being restricted to monitor just the particular areas with no freedom in measuring multiple locations under the furnace.

7.3.5   Lift-off and Spatial Response

Lift-off tests were carried out in the laboratory tank and the test rig to observe the sensitivity of the sensor towards lift-off changes and its spatial responses. To obtain a better accuracy in inversion of the data, for every frequency, 21 sets of mutual coupling impedances data were used. A full range of readings are plotted in Figure 86 and Figure 87with response to the lift-offs in the laboratory and the test rig experiments.

For the experiment in the laboratory, the tank was placed above the coils array. The tank was filled with saline with conductivity of 10 Sm^{-1} with 50 mm depth. The test started with a lift-off of 250 mm and gradually increased by 25 mm, measuring 4 lift-off levels. A 1 MHz frequency was used. Figure 86 shows the phase change of the signals across all the coil pairs as a result of the lift-off variation.
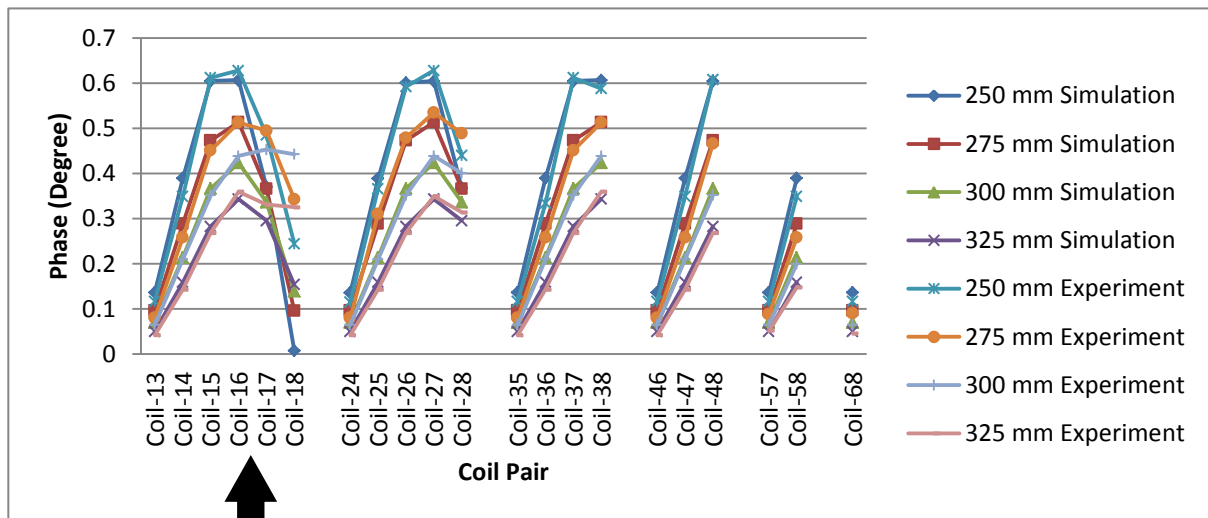
(a)
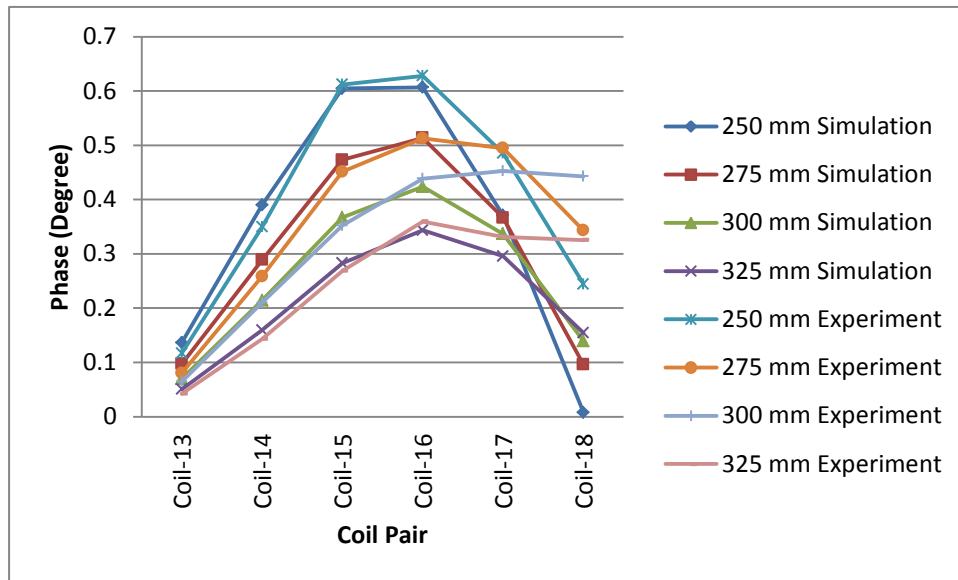
(b)

Figure 86 Comparison of effect of lift-off in phase for simulation and experiment data in laboratory (a) 21 coil pairs (b) 6 coil pairs with coil 1 as transmitter

As the data shows, it can be observed that the trends of the experiment responses are closely matched with the simulated results. As the separation between the transmitting and receiving coils increases, the higher the change of the phase signals; this indicates that it is more sensitive towards the lift-off change. However, emphasized in Figure 86(b), for separations of

coils from coil-16 onwards, the signals are interfered by noise. Therefore, the signals for coil-17 and coil-18 showed a significant difference for the simulated and experimented data.

The high noise in the signals may be due to the small volume of the saline in the tank, which only contained only a 50 mm depth of saline. This will contribute only a small signal. Also, as mentioned earlier, the length of the tank is 620 mm and the length of the 8 coils array is 616 mm. Hence, it is difficult to locate the tank right above the saline. It is also not practical as the coils nearer to the sides are not able to detect the saline.

To observe the same experiment results with a different set up locations, the experiment were carried out in the cold furnace test rig. This trial also allows a more realistic scenario with the coil beams at the surrounding of the sensor. The sensor was slid into the desired position with the wooden holder as guidance as described earlier. The lift-off levels were changed with the help of Styrofoam by having it stacked up before layering the waterproof sheet. Then a waterproof sheet was layered on top of the Styrofoam to allow the water to be easily removed from the tank when the experiment was finished.

Three lift-off levels were experimented; the lift-offs are 260 mm, 300 mm, and 350 mm. The saline conductivity was 9 Sm^{-1} with a saline depth of 100 mm. The comparisons of the simulated and measured values are shown in the following figures.
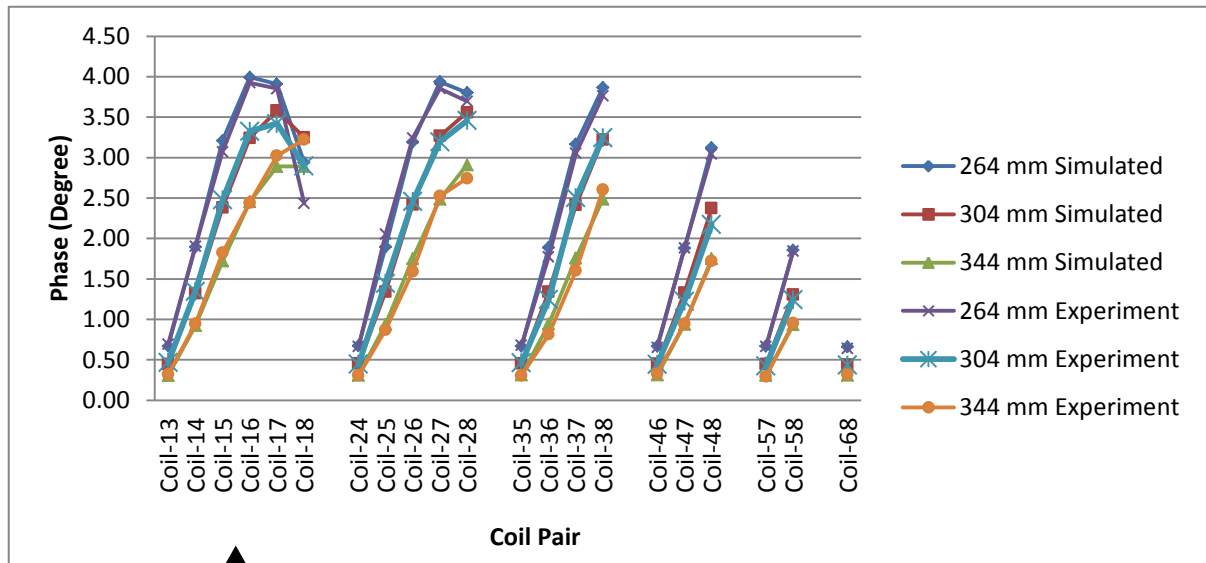
(a)
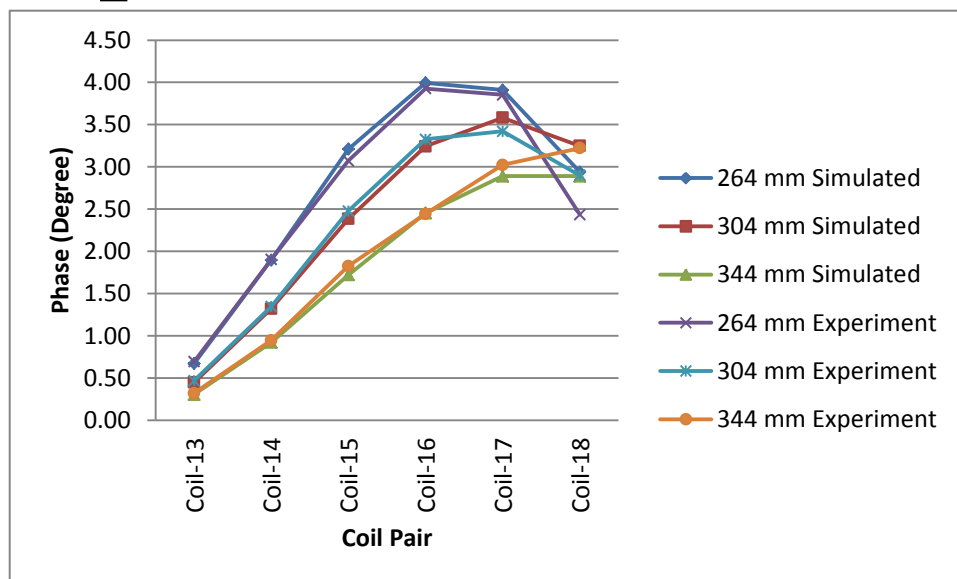
(b)

Figure 87 Comparison of effect of lift-off in phase for simulation and experiment data in test rig
(a) 21 coil pairs (b) 6 coil pairs with coil 1 as transmitter

By observing the figures, the values for coil-17 and coil-18 are affected by noise. However, the noise level is lower for coil-17. The signals scale is much bigger compared to the signals obtained in the laboratory. This is due to the bigger volume of saline; hence, improving the signals strength. Also the simulated and the experimental results show greater accord.

7.4   Hot Trial Test

As the laboratory tank and test rig experiment produced promising results, the next step was to try these methods in hot conditions under a real production furnace. The furnace experiment was conducted on the UK6 Pilkington site at St. Helens.

The difference for the experiment setup between the cold end and the hot end is for the hot end, it requires a much higher demand in the cooling system as well as the heat shield. To cool the equipment, a vortex air cooler was setup to direct cold air towards the equipment, which located in the cabinet. For the sensor head, a 10 mm cooling air pipe was installed and it was turned on constantly throughout the experiment, providing air circulation and preventing the overheating of electronics in the enclosure.

The front end electronics was placed in the enclosure with the support of a pole, which connected to a telescopic tripod stand such that the height of the sensor could be extended to press against the furnace wall during the measurement. Reference signals were obtained before and after the measurement for the furnace wall. This reference signal was for the calculation for the signal changed due to the existence of glass. The reference signals were obtained by placing the sensor at a lower level, as shown in Figure 88(a). Movement of the sensor, the cabling and the electronics might contribute inaccuracy into the measurements. Therefore, the reference signals will allow the study of the stability of the signals. This experiment was taken place at 6 locations under the furnace.
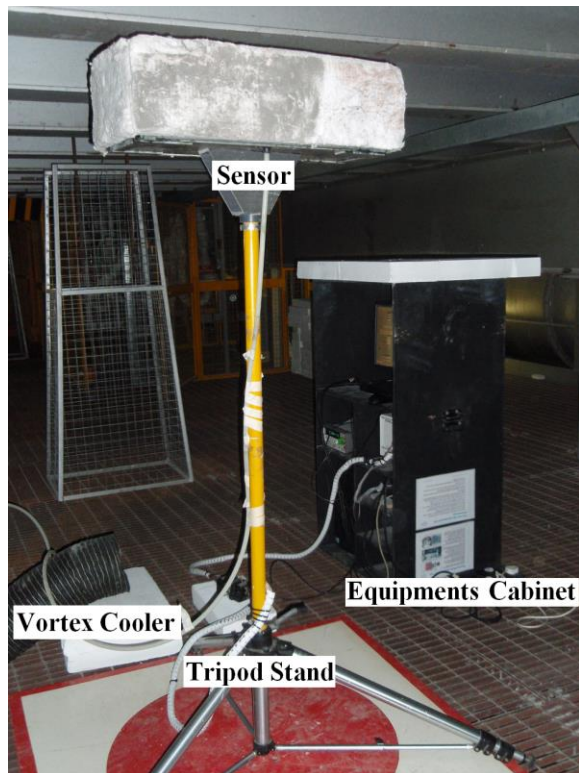
Figure 88 Hot end experiment setup in obtaining (a) reference signal (b) glass signal
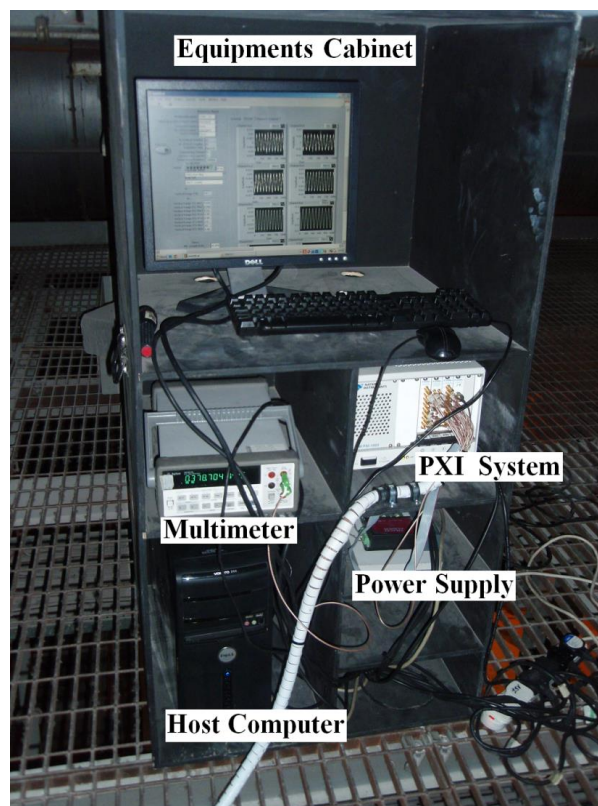
Figure 89 Equipments cabinet

7.4.1 Signal Processing Method

In the previous tests in the laboratory and the test rig, the experiments results were carried out by simulating a known thickness for a confirmation in the lift-off levels. The data produced in the laboratory experiment is used to analyse the error rate of the device. As observed in Figure 86 and Figure 87, the noise level in the furthest distance of coupling coil pair, the coil-18 is very high; hence, it is ignored in the data inversion and the error rate calculation.

The error rates for the laboratory lift-off experiment are calculated with Equation 39. By comparing with the known impedance data obtained from the FEM modelling, the error rates are given in Table 5.

$$S_{RMS} = \sqrt{\frac{1}{N} \sum \left(Q_{m_{nf}} - Q_{s_{nf}} \right)^2}$$

Equation 39

where

S_{RMS} : RMS of measurement error

N : Number of coil pairs

Q_m : Measurement value

Q_s : Simulated value

n : Coil pair configuration

f : Frequency

Lift-off level (mm)	250	275	300	325
Difference (%)	3.56	3.42	2.78	4.10

Table 5 Error rate of laboratory lift-off experiment

The analysis suggests that an average accuracy of 3.47% can be achieved by the instrument. Other sources, such as the millimetre scale for lift-off measurements, thermal drift in experiment, surrounding conductive materials, error of conductivity meter measurement etc may affect the accuracy achieved.

In the on-line trial, the thickness of the furnace wall is the interest of the experiment; hence, the previous method, which simulate the known lift-off levels for comparison is not able to apply into the on-line trial results analysis. A look up table was proposed in this project to invert the experiment results into the thickness of the wall. This is by simulating a multiple levels of wall thickness in the FEM simulator. The impedance data obtained was being stored in the table. Then by applying Equation 39, the comparison of the measurement data can be inverted to its thickness value.

By plotting the RMS value of the measurement error, at the minimum point of the curve, it indicates the least measurement error for the measurement data compared with the simulated data. Hence, this point indicates the thickness of the block.

7.4.2 On-line Trial Results and Analysis
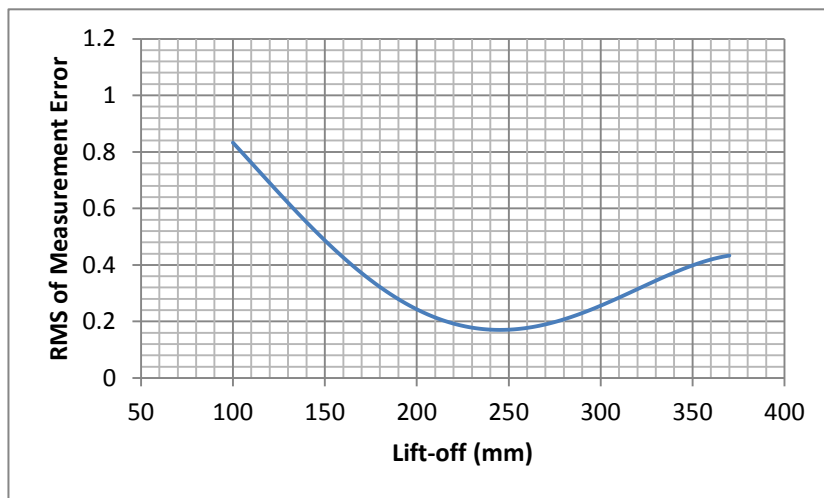
(a)
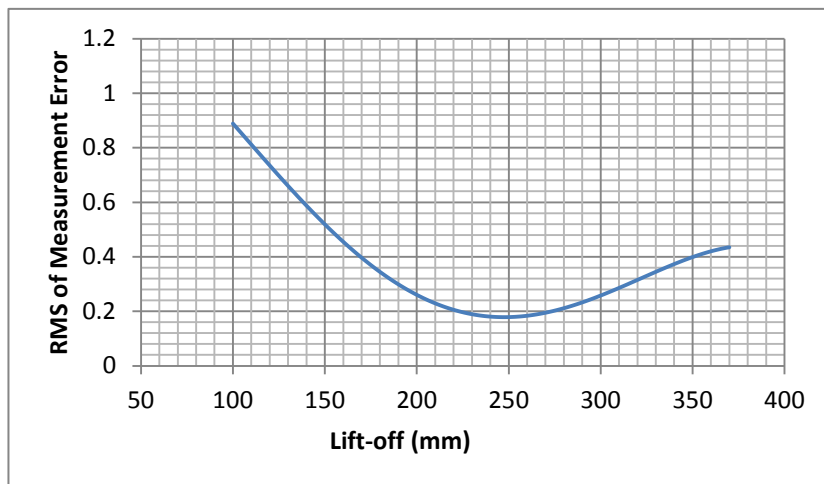
(b)
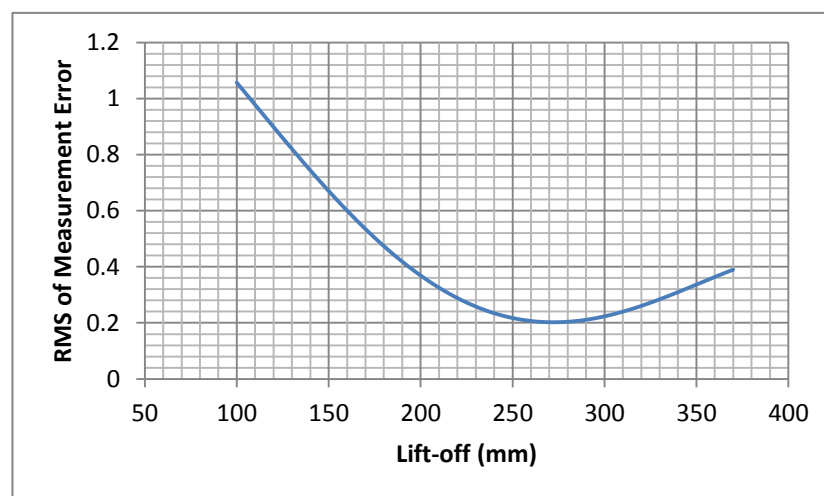
(c)
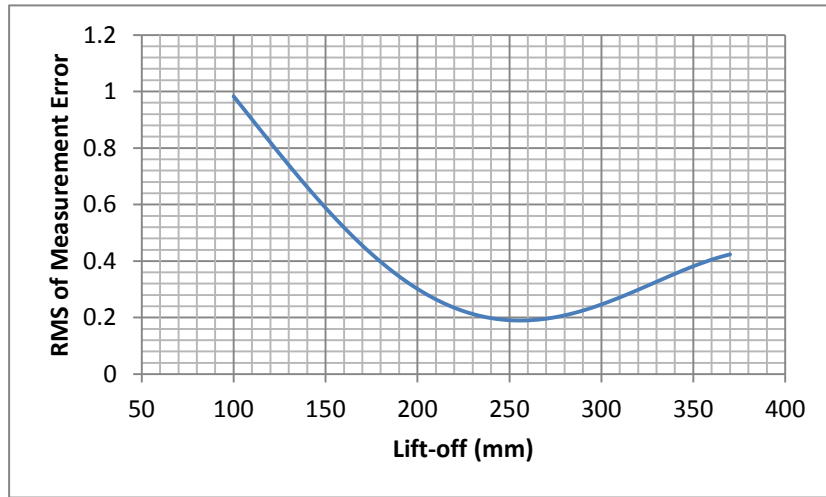
(d)
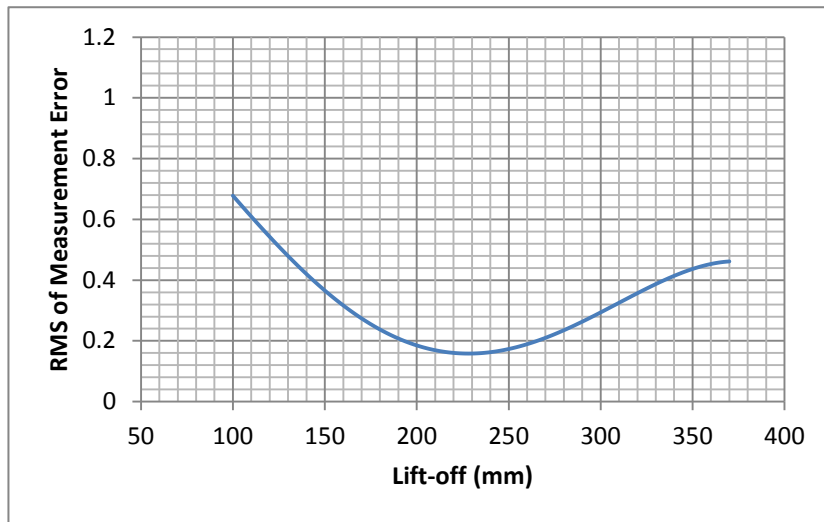
(e)
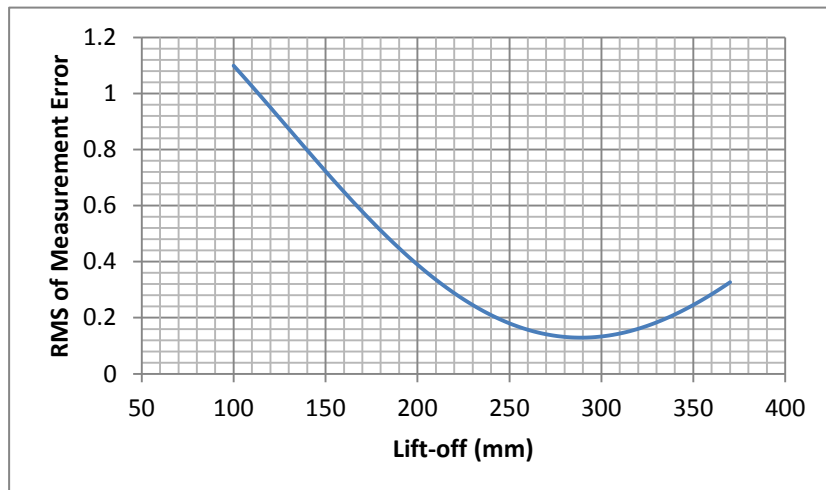
(f)

Figure 90 Inversion of measurement data (a) Position 1 (b) Position 2

(c) Position 3 (d) Position 4 (e) Position 5 (f) Position 6

For the experiment, according to the temperature range provided for the experiment location, the conductivity of the melt is calculated to be 9.26 – 10.50 Sm^{-1}. Therefore, 10 Sm^{-1} was used in the simulation and stored in the look up table. Full range of frequencies was used during the experiment, which is 500 kHz, 600 kHz, 700 kHz, 800 kHz, 1 MHz, 2 MHz, 4 MHz, 8 MHz and 10 MHz. However, the results for the lower range and higher range of frequencies appeared to be unstable. By plotting the graph of the spatial data for the high frequencies and low frequencies measurements, the signals appeared to be interfered by noise significantly. Hence, elimination was carried out and only 1 MHz and 2 MHz signals were inverted. The estimation for the bottom wall thickness were expected to be 245 mm, 248 mm, 272 mm, 256 mm, 228 mm and 289 mm with the sequence for position 1 to position 6.

However, the thickness estimation did not give acceptable results. The drilling result has shown that the thickness of the wall for position 2 is with 305 mm of clay flux block and 70 mm of AZS. Position 5 was drilled and 305 mm of clay flux appeared, the AZS was not fully drilled as drilling process takes a very long time. Hence, the AZS was predicted to be 55 mm to 65 mm.

The drilling results have shown a serious discrepancy with the previous prediction. The difference of the estimation may due to the distance of the molten glass is too far to be detected by the sensor. For distance of the coil to the bottom of the furnace, it has a margin of 200 mm due to the 50 mm blanket as heat shield and 150 mm of space from the coil to the enclosure wall, which was left on purpose to allow the air circulation in the enclosure. Consequently, the distance from the coils to the glass is approximately 555 mm – 570 mm.

Figure 91 and Figure 92 show the simulation for coil-14 and coil-17 with frequencies of 1 MHz and 8 MHz. The phase signal for the distance of approximately 555 – 570 mm of distance from coil to glass is can be estimated.
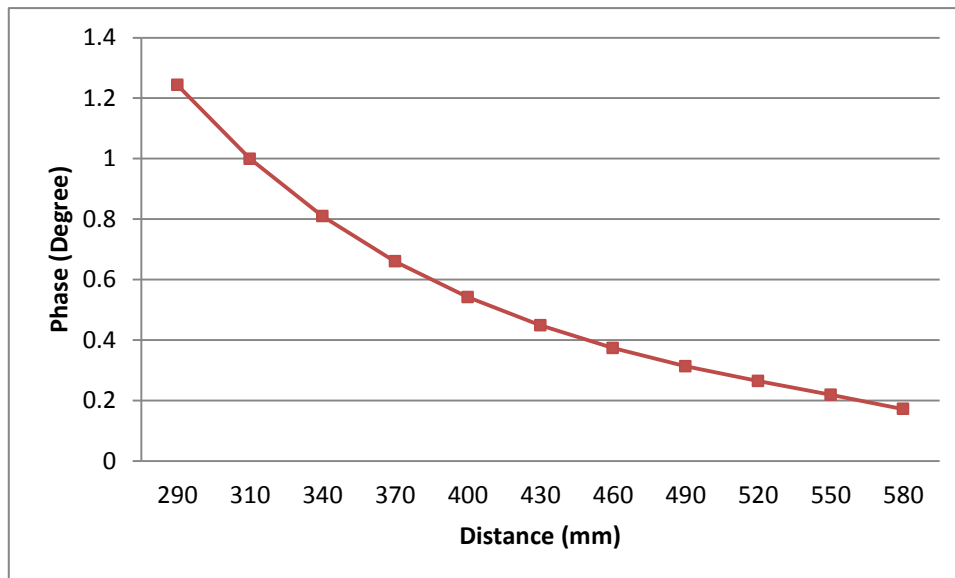
(a)
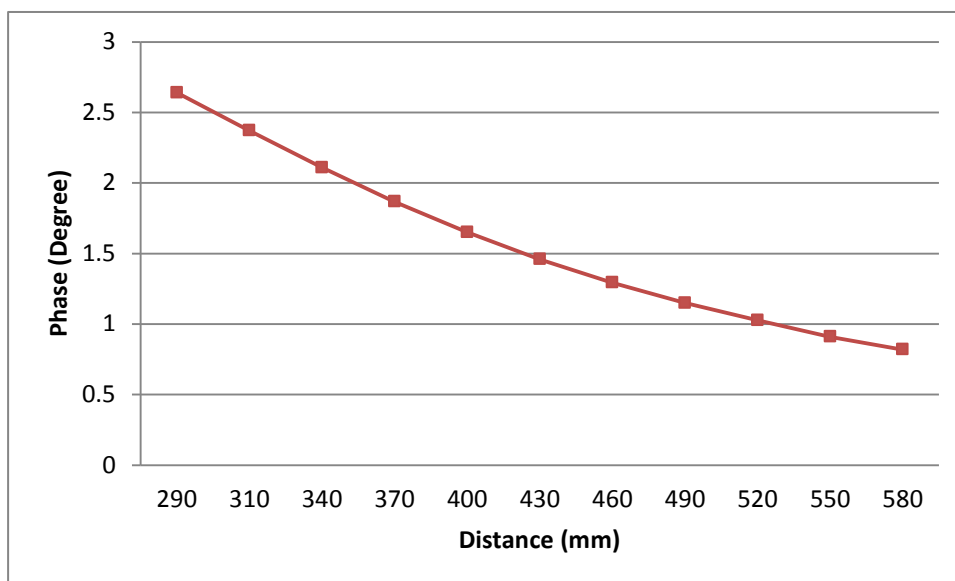
(b)

Figure 91 Analysis of phase signal for distance of 555 – 570 mm between coils and glass
(a) Coil-14 (b) Coil-17 at 1 MHz
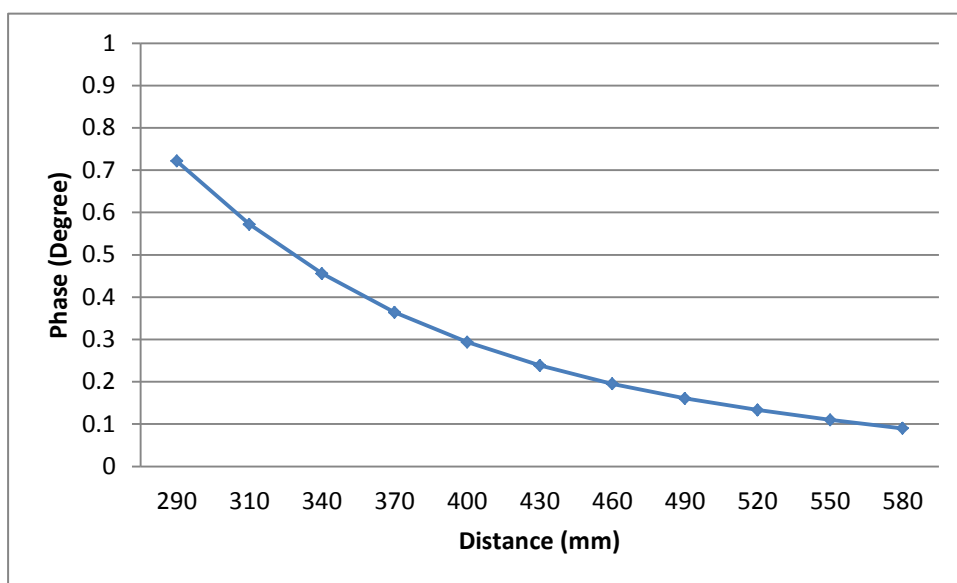
(a)
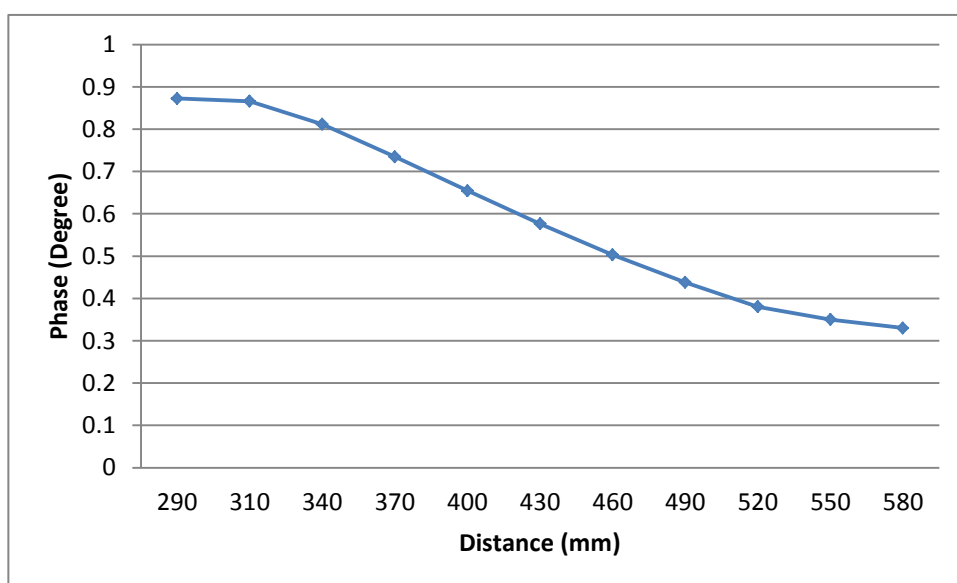
(b)

Figure 92 Analysis of phase signal for distance of 555 – 570 mm between coils and glass
(a) Coil-14 (b) Coil-17 at 8 MHz

As indicated by the Figure 91, the signal estimated to be detected in coil-14 for the distance of 570 mm is approximately 190 millidegree. For coil-17, it has shown that the signal is at approximately 750 millidegree. These show that the signal will be obtain for this distance is very small as the electronics will drift with temperature to a certain extent. Although the signal for coil-17 is estimated to be 750 millidegree, with a much harsher environment, the system may contribute more noise and affect this reading much more than the noise experienced in the same channel during the test rig experiment at room temperature. The inversion of thickness was calculated by RMS of measurement of error for 21 coil pairs; hence, with the low signals for the nearer distances coils such as coil-13, coil-14 coil-25 etc, it will contribute a significant error rate into the overall calculations.

Figure 92 has shown the estimated reading for 8 MHz transmitting signal. The graph indicates that for the same distance, the pair of coil-14 is estimated to obtain less than 100 millidegree phase change and 310 millidegree for coil-17. The far distance of the sensor with the coil has reduced the sensitivity of the sensor significantly.

7.5   Conclusion

The lift off levels is able to represents the thickness of the clay flux and AZS which acts as the support ground for the molten glass. In order to achieve the objective of producing a portable multi-frequency sensor that is able to work in the harsh environment, the tests on the sensitivity of the sensor was carried out.

Experiment was performed to ensure that the system is not affected by the difference in the steel beams in the furnace, as the steel beam supports might vary from location to location under the same furnace. The change in the distances between the beams, the signals are not significant compared to the lift-off of the saline. The consideration of different design of furnace with grillage supporter has shown that with the coverage of the grillage, the system has shown that the grillage has blocked the signals significantly.

The system has shown an excellent ability in providing a significant variation in signals with the change in lift-off levels in the cold environment. This has encouraged proceeding the trial

to measure the thickness of the wall at the hot end with this sensor. However, the results have shown disagreement for the simulated and the experimented data. This may be caused by the signal is too small for detection as the furnace wall is showing almost no sign of wear, which has challenged the limit of the sensor in detecting a far distance target. Also the signals may be introduced by noise as well as the contribution of the temperature drift for the electronics.

Chapter 8 Conclusion

In this PhD project, an improved version of an experimental system to be used in the demanding environment under a production glass furnace was researched, designed, built and tested. This experimental system has employed eddy current inspection techniques to measure a low conductivity target, which in this case was molten glass and saline.

The system has successfully enhanced its portability with a series of extensive improvements carried out on the data acquisition system. The hardware was improved and replaced with a smaller or lighter version, such as the signal generator was replaced with the PXI signal generator module. The current system consists of just three distinct pieces of hardware, namely the sensor array, a 6U box containing all the electronics and a notebook PC running the system software. The 6U box was designed to have 4 self-cooling fans fitted at its front and back panels, reduce the need of additional cooling during the online-trial test.

The heat shield made by fibreglass was experimented in the on-line trial to be able to provide protection to the electronics in the enclosure from exposing the high temperature. It was able to reduce the temperature at the inner of the enclosure from approximately 420 ^{o}C down to 70 ^{o}C. This allows the electronics to work at the temperature as suggested by the component manufacturers, preventing the signal drifts due to temperature. However, this heat shield has significant contribution towards the weight of the sensor head. Hence, a newly designed of the sensor head was built, which reduced the weight of the sensor head from approximately 13 kg to 6 kg.

The design of a multi-channel receiving circuit has greatly reduced the time of measurement in the experiment. The system has been also designed to have an automatic scanning system for switching the transmitting circuit which eliminate the time required for the system equilibrium to be achieved. While switching the transmitter, the program input the parameters automatically from the pre-stored file, which avoid the need of manual tuning on the equipments.

A modelling algorithm which provides flexibility in changing its lift-off was constructed. By using the layering method, the model for different lift-off can be easily developed by just

changing the properties of different layers. Initially, FEM modelling was used in designing the coil array system. The magnitude of the sensitivity of the sensing coil to the eddy currents increases as the distance of coupling coil pair increases. Hence, the system is designed to have a planar coil array to obtain more spatial analysis. As the temperature of the molten glass changes, the conductivities vary accordingly. With the simulation analysis, the phase signal of the coils' impedance coupling is able to provide stable measurement with the variation of conductivities in the target.

One of the main challenges in this research is the complexity of the steel support under the furnace. According to the simulations and experiments, with small variation in distances between the furnaces supporting steel beams, will not affect the phase signal. However, the magnitudes of the signal are more prone to errors from the proximity of the steel structures. For this project, a multi-frequency sweep system is built. The phase signal has shown to be immune to the existence of steels at frequencies that are higher than 0.8 MHz when tested in the laboratory. This provides the advantage of for any phase signal change observed at higher frequencies; the signal is solely from the glass. As the old furnaces have grillage as bottom support, experiment was carried out by locating grillage between the coils and the saline target. The grillage has effectively shielded the signals from passing through it, hence, indicating that the system is not usable in furnaces that contained grillage.

By using the curve fitting method, the sensor was successfully provided matching results for the lift-off experiment from low conducting saline target in the laboratory and test rig with the FEM simulated data. The instrument has an average error rate of 3.47%. For the highest test rig lift-off measurement, the error rate gives an uncertainty of deviation of +/-11 mm for 325 mm. For the on-line trial, the analysed data has shown a poor matching thickness from the actual wall thickness. This unsuccessful inversion is due to the limitation of sensing range of the system.

8.1   Limitations

To eliminate the effect of the steel beams on the signals, a multi-frequency system was proposed in this project. At high frequencies, the effect of steel is insignificant on the phase signal, hence, the signal change at the high frequencies are mainly from the molten glass. However, for the signals at high frequencies which are above 4 MHz, the voltage appeared to be very low to be able to pick up by the receiver. Apart from that, there is a limit in the PXI system with 60 MHz sampling frequency, which may be insufficient at the higher signal frequencies used. At low frequencies, the signals appeared to have too much noise. Therefore, the signals below 700 kHz and above 4 MHz were often discarded due to its less reliability.

The cabling also affects the signals when bent or moved. This may be introduced by the change of propagation speed for the signal when the cable is bent. During the experiments, it is always required to carefully reposition the cables and also wrap the cable looms with spiral wrap. This reduced the effect but a strong movement or bending the cables would still exasperate the problem.

The cooling system inputs the compressed air from the furnace. Unfortunately, the compressed air supply may also be hot as the air line run close to the furnace. Therefore, to reduce the temperature of the sensor, a vortex cooler, was used to blow towards the sensor head. This is to improve the air circulation of the sensor head from the air gap between the lid and the bottom pan. However, this method is not practical to be applied all the time.

The hot end online trial has shown that the distance of the conducting molten glass may be too far to be detected and this causes the signals to be too small to be picked up. The electronics would benefit from even greater sensitivity or a feature to determine if the molten glass is out of range.

8.2   Future work

A complete prototype which is much more portable was built as a refinement of the current system. The newly built enclosure is thinner yet giving the same protection properties as the fibreglass blanket. Hence, it allows the sensing coil to be placed closer to the furnace wall, which reduces the distance between the coil and the detecting target. However, the ability of the heat protection is still yet to be tested at the furnace.

An improvement in the cabling system can be carried out. The semi-rigid cable is a suitable option for the applications as it is manufactured to be less bendable compared to normal coax cable, hence, the speed of the signal will be less affected during the movement of the sensor.

For current system, the analysis is done offline. A curve fitting approach has been developed during the project to interpolate between coarse finite element predictions. However, this requires a specialist to do the calculations. Therefore, a simple inversion algorithm can be formulated in order to detect the wall thickness for on-site use. This algorithm should provide a user interface that is easy use and understood.

The simulations in the project assumed that the furnace wall is in a flat surface. However, this is often not the case. The walls that are located above the dwarf bricks are tend to have a higher corrosion. Therefore, with the application of reconstruction algorithms, the profile of the bottom wall can be obtained.

Reference

1. Grzegorz Zysko, *Electromagnetic techniques for glass furnaces inspection and monitoring". School of Electrical and Electronic Engineering.* The University of Manchester, 2008. **PhD Thesis**.

2. S. Budd, *Formation of gas bubbles in glass at high temperature.* Glass and Ceramics, 1963. **20**(5): p. 291-292.

3. Helen R. Golob and E. Lowell Swarts, *Disproportionation of SO2 in bubbles within soda-containing glasses.* Journal of the American Ceramic Society, 1984. **67**(8): p. 564-567.

4. B. Varghese, C. DeConick, G. Cartee, R. Zoughi, M. Velez, and R. Moore, *High‐temperature monitoring of refractory wall recession using frequency‐modulated continuous‐wave (FM‐CW) radar techniques.* American Institute of Physics Conference, 2005. **760**: p. 7.

5. R. G. C. Beerkens and O. S. Verheijen, *Reactions of alkali vapours with silica based refractory in glass furnaces, thermodynamics and mass transfer.* Glass Technology - European Journal of Glass Science and Technology Part A, 2005. **46**(6): p. 371-382.

6. Michael Dunkl, *Glass melt - refractories interaction.* http://kdsolution.com, 2003.

7. W. E. Lee and S. Zhang, *Melt corrosion of oxide and oxide–carbon refractories.* International Materials Reviews, 1999. **44**(3): p. 77-104.

8. M. Velez, J. Smith, and R. E. Moore, *Refractory degradation in glass tank melters. A survey of testing methods.* Cerâmica, 1997. **43**: p. 180-184.

9. John Ferguson, *Centrifugal glass-melting furnace.* United States Patent. **2006947**(July 1935).

10. Kazuo Kiyonaga, *Process for producing glass in a rotary furnace.* United States Patent. **4185984**(January 1980).

11. L. Recca, *Glass: rotary electric glass furnace.* Other Information: PBD: 29 Jan 1999. 1999. Medium: ED; Size: vp.

12. R. R. Hayes, S. Brewster, B. W. Webb, M. Q. McQuay, and A. M. Huber, *Crown incident radiant heat flux measurements in an industrial, regenerative, gas-fired, flat-glass furnace.* Experimental Thermal and Fluid Science, 2001. **24**(1–2): p. 35-46.

13. V. Sardeshpande, U. N. Gaitonde, and Rangan R. Banerjee, *Model based energy benchmarking for glass furnace.* Energy Conversion and Management, 2007. **48**(10): p. 2718-2738.

14. R. L. Webb, D. Marchiori, R. E. Durbin, Y. J. Wang, and A. K. Kulkarni, *Heat exchangers for secondary heat recovery from glass plants.* Journal of Heat Recovery Systems, 1984. **4**(2): p. 77-85.

15. Fabien S. Illy, *Method of glass manufacture involving separate preheating of components.* United States Patent, 2001. **November 20, 2001**(US 6,318,127 B1).

16. V. Kuzyak, *Electric boosting of glass heating in flame tank furnaces.* Glass and Ceramics, 1958. **15**(11): p. 586-591.

17. Aydin Ungan and Raymond Viskanta, *Three-dimensional numerical simulation of circulation and heat transfer in an electrically boosted glass melting tank.* Industry Applications, IEEE Transactions on, 1986. **IA-22**(5): p. 922-933.

18. B. E. Ydstie and Jiao Yu, *Passivity-based control of the float-glass process.* Control Systems, IEEE, 2006. **26**(6): p. 64-72.

19. L. A. B. Pilkington, *Review lecture. The float glass process.* Proceedings of the Royal Society of London. A. Mathematical and Physical Sciences, 1969. **314**(1516): p. 1-25.

20. Lionel A. B. Pilkington and Kenneth Bickerstaff, *Manufacture of flat glass.* United States Patent, 1959. **Nov. 10, 1959**(2911759).

21. Richard J. McCurdy, *Successful implementation methods of atmospheric CVD on a glass manufacturing line.* Thin Solid Films, 1999. **351**(1–2): p. 66-72.

22. J. Malzbender and G. de With, *Cracking and residual stress in hybrid coatings on float glass.* Thin Solid Films, 2000. **359**(2): p. 210-214.

23. R. J. Hand, F. H. Wang, B. Ellis, and A. B. Seddon, *Glass strengthening using ormosil polymeric coatings.* Journal of Sol-Gel Science and Technology, 1998. **13**(1-3): p. 695-699.

24. TianHe Wang and P. F. James, *Strengthening soda-lime-silica glass by a low-expansion coating applied by melt dipping.* Journal of Materials Science, 1991. **26**(2): p. 354-360.

25. Roy Gordon, *Chemical vapor deposition of coatings on glass.* Journal of Non-Crystalline Solids, 1997. **218**(0): p. 81-91.

26. Xiangqian Peng, Youping Chen, Wenyong Yu, Zude Zhou, and Guodong Sun, *An online defects inspection method for float glass fabrication based on machine vision.* The International Journal of Advanced Manufacturing Technology, 2008. **39**(11-12): p. 1180-1189.

27. F. Adamo, F. Attivissimo, and A. Di Nisio, *Calibration of an inspection system for online quality control of satin glass.* Instrumentation and Measurement, IEEE Transactions on, 2010. **59**(5): p. 1035-1046.

28. Jonathan D. Holmes, *Inspection of float glass using a novel retroreflective laser scanning system.* 1997: p. 180-190.

29. Joachim Bretschneider and Hubert Drexler, *Soda-lime-silicate glass composition.* United States Patent, 2001. **April 17, 2001**(US 6,218,323 B1).

30. Steven P Beckwith, William M Yankovich, and Bethel Park, *High visible, low UV and low IR transmittance green glass composition.* United States Patent, 1993. **May 25, 1993**(5,214,008).

31. Manoj K. Choudhary, *Recent advances in mathematical modeling of flow and heat transfer phenomena in glass furnaces.* Journal of the American Ceramic Society, 2002. **85**(5): p. 1030-1036.

32. A. Abbassi and Kh Khoshmanesh, *Numerical simulation and experimental analysis of an industrial glass melting furnace.* Applied Thermal Engineering, 2008. **28**(5–6): p. 450-459.

33. Zhijun Feng, Dongchun Li, Guoqiang Qin, and Shimin Liu, *A new method to optimize furnace designs using daily flow rates to maximize energy savings in the steady production.* Journal of the American Ceramic Society, 2009. **92**(10): p. 2459-2462.

34. Alexander V. Korjenevsky and Vladimir A. Cherepenin, *Progress in realization of magnetic induction tomography.* Annals of the New York Academy of Sciences, 1999. **873**(1): p. 346-352.

35. S. Aoki, S. Kawachi, and M. Sugeno, *Application of fuzzy control logic for dead-time processes in a glass melting furnace.* Fuzzy Sets and Systems, 1990. **38**(3): p. 251-265.

36. J. J. Keavney and E. C. Eberlin, *The determination of glass transition temperatures by differential thermal analysis.* Journal of Applied Polymer Science, 1960. **3**(7): p. 47-53.

37. S. B. Lisenenkova, N. A. Gusev, G. A. Kratko, and V. G. Vakulov, *A study using radioactive tracers of glass tube production.* Glass and Ceramics, 1973. **30**(9): p. 597-600.

38. J. St Michalik and K. G. Kruszewski, *Application of the radiotracer method of molten glass flow process identification for optimization of tank furnaces.* Isotopenpraxis Isotopes in Environmental and Health Studies, 1986. **22**(7): p. 232-235.

39. R. Van Laethem, L. Leger, M. BoffÉ, and E. Plumat, *Temperature measurement of glass by radiation analysis.* Journal of the American Ceramic Society, 1961. **44**(7): p. 321-332.

40. U. Mori and H. Hashima, *Development of a method for measuring molten glass flow.* XIX International Congress Glass, Edinburgh, 2002.

41. S. F. Collins, G. W. Baxter, S. A. Wade, T. Sun, K. T. V. Grattan, Z. Y. Zhang, and A. W. Palmer, *Comparison of fluorescence-based temperature sensor schemes: Theoretical analysis and experimental validation.* Journal of Applied Physics, 1998. **84**(9): p. 4649-4654.

42. Wegfrass André, Diethold Christian, Werner Michael, Resagk Christian, Fröhlich Thomas, Halbedel Bernd, and Thess André, *Flow rate measurement of weakly conducting fluids using Lorentz force velocimetry.* Measurement Science and Technology, 2012. **23**(10): p. 105307.

43. A. Thess, E. V. Votyakov, and Y. Kolesnikov, *Lorentz force velocimetry.* Physical Review Letters, 2006. **96**(16): p. 164501.

44. J. J. Borbas, R. C. Padfield, and E. Moscker, *Density determination of refractories by measurement of gamma-radiation absorption.* Journal of the American Ceramic Society, 1967. **50**(8): p. 421-424.

45. L. Staicu and R. Radu, *The use of the (γ, n) reaction to measure wear in blast furnaces and other industrial furnaces: comparison with present methods.* Journal of Physics D: Applied Physics, 1983. **16**(12): p. 2541.

46. N. Bolf, *Application of infrared thermography in chemical engineering.* Journal of Chemists and Chemical Engineers, 2004. **53**(12): p. 549-555.

47. X. Maldague, *Introduction to NDT by active infrared thermography.* Materials Evaluation, 2002. **6**(9): p. 1060-1073.

48. A. Sadri, G. Walters, and M. Lachemi, *Determination of refractory lining thickness and quality in operating industrial furnaces, using a stress wave reflection technique.* 1st CSCE Specialty Conference on Infrastructure Technologies, Management and Policy, Toronto, Canada, 2005.

49. P. Gebski A. Sadri, E. Shameli, *Refractory wear and lining profile determination in operating electric furnaces using stress wave non-destructive testing (NDT).* The Twelfth International Ferroalloys Congress, 2010: p. 881-890.

50. Jaejoon Kim, Guang Yang, Lalita Udpa, and Satish Udpa, *Classification of pulsed eddy current GMR data on aircraft structures.* NDT & E International, 2010. **43**(2): p. 141-144.

51. Barend van den Bos, Stefan Sahlen, and Joakim Andersson, *Automatic scanning with multi-frequency eddy current on multi-layered structures.* Aircraft Engineering and Aerospace Technology, 2003. **75**(5): p. 491-496.

52. Ali Sophian, Gui Yun Tian, David Taylor, and John Rudlin, *Design of a pulsed eddy current sensor for detection of defects in aircraft lap-joints.* Sensors and Actuators A: Physical, 2002. **101**(1–2): p. 92-98.

53. D. G. Park, C. S. Angani, G. D. Kim, and Y. M. Cheong, *Evaluation of pulsed eddy current response and detection of the thickness variation in the stainless steel.* Magnetics, IEEE Transactions on, 2009. **45**(10): p. 3893-3896.

54. C. S. Angani, D. G. Park, G. D. Kim, C. G. Kim, and Y. M. Cheong, *Differential pulsed eddy current sensor for the detection of wall thinning in an insulated stainless steel pipe.* Journal of Applied Physics, 2009. **107**(9).

55.   Ananth Sethuraman and James H Rose, *Rapid inversion of eddy current data for conductivity and thickness of metal coatings.* Journal of Nondestructive Evaluation, 1995. **14**(1): p. 39-46.

56.   D. Placko, H. Clergeot, and E. Santander, *Physical modeling of an eddy current sensor designed for real time distance and thickness measurement in galvanization industry.* Magnetics, IEEE Transactions on, 1989. **25**(4): p. 2861-2863.

57.   W. Yin and A. J. Peyton, *Thickness measurement of non-magnetic plates using multi-frequency eddy current sensors.* NDT & E International, 2007. **40**(1): p. 43-48.

58.   Cheng-Chi Tai, James-H. Rose, and John C. Moulder, *Thickness and conductivity of metallic layers from pulsed eddy-current measurements.* Review of Scientific Instruments, 1996. **67**(11): p. 3965-3972.

59.   W. Yin, P. J. Withers, U. Sharma, and A. J. Peyton. *Non-contact characterisation of carbon-fibre-reinforced plastics (CFRP) using multi-frequency eddy current sensors.* in *Instrumentation and Measurement Technology Conference Proceedings, 2007. IMTC 2007. IEEE.* 2007.

60.   L. Li and R. A. Kruger, *An electrodeless measuring technique for determining conductivity of biological tissues at radio frequencies.* Physics in Medicine and Biology, 1988. **33**(12): p. 1443.

61.   Peter P. Tarjan and Richard McFee, *Electrodeless measurements of the effective resistivity of the human torso and head by magnetic induction.* Biomedical Engineering, IEEE Transactions on, 1968. **BME-15**(4): p. 266-278.

62.   L. W. Hart, H. W. Ko, J. H. Meyer, D. P. Vasholz, and R. I. Joseph, *A noninvasive electromagnetic conductivity sensor for biomedical applications.* Biomedical Engineering, IEEE Transactions on, 1988. **35**(12): p. 1011-1022.

63.   R. Casañas, H. Scharfetter, A. Altes, A. Remacha, P. Sarda, J. Sierra, R. Merwa, K. Hollaus, and J. Rosell, *Measurement of liver iron overload by magnetic induction using a planar gradiometer: preliminary human results.* Physiological Measurement, 2004. **25**(1): p. 315.

64.   Robert Merwa, Karl Hollaus, Oszkar Biro, and Hermann Scharfetter, *Detection of brain oedema using magnetic induction tomography: a feasibility study of the likely sensitivity and detectability.* Physiological Measurement, 2004. **25**(1): p. 347.

65.   M. Zolgharni, P. D. Ledger, and H. Griffiths, *Forward modelling of magnetic induction tomography: a sensitivity study for detecting haemorrhagic cerebral stroke.* Medical & Biological Engineering & Computing, 2009. **47**(12): p. 1301-1313.

66.   Yinan Chen, Ming Yan, Dayu Chen, Matthias Hamsch, Hui Liu, Hua Jin, Marko Vauhkonen, Claudia H Igney, Joachim Kahlert, and Yuanyuan Wang, *Imaging hemorrhagic stroke with magnetic induction tomography: realistic simulation and evaluation.* Physiological Measurement, 2010. **31**(6): p. 809.

67.   M. Soleimani and W. R. B. Lionheart, *Image reconstruction in three-dimensional magnetostatic permeability tomography.* Magnetics, IEEE Transactions on, 2005. **41**(4): p. 1274-1279.

68.   Eric P. Berg, Amha Asfaw, and Mark R. Ellersieck, *Predicting pork carcass and primal lean content from electromagnetic scans.* Meat Science, 2002. **60**(2): p. 133-139.

69.   J. T. Akridge, B. W. Brorsen, L. D. Whipker, J. C. Forrest, C. J. Kuei, and A. P. Schinckel, *Evaluation of alternative techniques to determine pork carcass value.* Journal of Animal Science, 1992. **70**(1): p. 18-28.

70.   E. P. Berg, J. C. Forrest, and J. E. Fisher, *Electromagnetic scanning of pork carcasses in an on-line industrial configuration.* Journal of Animal Science, 1994. **72**(10): p. 2642-52.

71.   B. L. Gwartney, Chris R. Calkins, R. S. Lin, J. C. Forest, and Anne M. Parkhurst, *Electromagnetic scanning of beef quarters to predict carcass and primal lean content.* Journal of Animal Science, 1994. **72**(11): p. 7.

72.   W. Yin, A. J. Peyton, G. Zysko, and R. Denno. *Simultaneous non-contact measurement of water level and conductivity.* in *Instrumentation and Measurement Technology Conference, 2006. IMTC 2006. Proceedings of the IEEE*. 2006.

73.   H. Scharfetter, R. Casanas, and J. Rosell, *Biological tissue characterization by magnetic induction spectroscopy (MIS): requirements and limitations.* Biomedical Engineering, IEEE Transactions on, 2003. **50**(7): p. 870-880.

74.   Anthony Peyton, Zhi Zhong Yu, Said Al-Zeibak, Neville H. Saunders, and Anthonio Rui Borges, *Electromagnetic imaging using mutual inductance tomography: potential for process applications.* Particle & Particle Systems Characterization, 1995. **12**(2): p. 68-74.

75.   B.Dekdouk, Wuliang Yin, C. Ktistis, D. W. Armitage, and A. J. Peyton, *A method to solve the forward problem in magnetic induction tomography based on the weakly coupled field approximation.* Biomedical Engineering, IEEE Transactions on, 2010. **57**(4): p. 914-921.

76.   H. Griffiths, W. R. Stewart, and W. Gough, *Magnetic induction tomography: a measuring system for biological tissues.* Annals of the New York Academy of Sciences, 1999. **873**(1): p. 335-345.

77.   A. Morris, H. Griffiths, and W. Gough, *A numerical model for magnetic induction tomographic measurements in biological tissues.* Physiological Measurement, 2001. **22**(1): p. 113.

78.   A. Korjenevsky, V. Cherepenin, and S. Sapetsky, *Magnetic induction tomography: experimental realization.* Physiological Measurement, 2000. **21**(1): p. 89.

79.   Z. Z. Yu, A. Peyton, M. S. Beck, W. F. Conway, and L. A. Xu, *Imaging system based on electromagnetic tomography (EMT).* Electronics Letters, 1993. **29**(7): p. 625-626.

80.   Tomasz Chady, Masato Enokizono, Takashi Todaka, Yuji Tsuchida, and Tomoharu Yasutake, *Identification of three-dimensional distribution of metal particles using electromagnetic tomography system.* Journal of Materials Processing Technology, 2007. **181**(1–3): p. 177-181.

81.   H Griffiths, *Magnetic induction tomography.* Measurement Science and Technology, 2001. **12**(8): p. 1126.

82.   A. R. Borges, J. E. de Oliverira, J. Velez, C. Tavares, F. Linhares, and A. J. Peyton, *Development of electromagnetic tomography (EMT) for industrial aplications. Part 2: image reconstruction and software framework.* 1st World Congress on Industrial Process Tomography, 1999: p. 7.

83.   H. S. Tapp and A. J. Peyton, *A state of the art review of electromagnetic tomography.* Proceedings of the 3rd World Congress on Industrial Process Tomography, 2003: p. 340-346.

84.   C. V. Dodd and W. E. Deeds, *Analytical solutions to eddy‐current probe‐coil problems.* Journal of Applied Physics, 1968. **39**(6): p. 2829-2838.

85.   R. Ludwig and X. W. Dai, *Numerical and analytical modeling of pulsed eddy currents in a conducting half-space*, in *Magnetics, IEEE Transactions on*1990. p. 299-307.

86.   T. P. Theodoulidis, T. D. Tsiboukis, and E. E. Kriezis, *Analytical solutions in eddy current testing of layered metals with continuous conductivity profiles.* Magnetics, IEEE Transactions on, 1995. **31**(3): p. 2254-2260.

87.   Erol Uzal, John C. Moulder, Sreeparna Mitra, and James H. Rose, *Impedance of coils over layered metals with continuously variable conductivity and permeability: Theory and experiment.* Journal of Applied Physics, 1993. **74**(3): p. 2076-2089.

88.   Wuliang Yin, A. J. Peyton, and S. J. Dickinson, *Simultaneous measurement of distance and thickness of a thin metal plate with an electromagnetic sensor using a simplified model.* Instrumentation and Measurement, IEEE Transactions on, 2004. **53**(4): p. 1335-1338.

89.   C. C. Cheng, C. V. Dodd, and W. E. Dodds, *General analysis of probe coils near stratified conductors.* Int. J. Nondestr. Test., 1971. **3**: p. 109-130.

90.   E. Uzal and J. H. Rose, *The impedance of eddy current probes above layered metals whose conductivity and permeability vary continuously.* Magnetics, IEEE Transactions on, 1993. **29**(2): p. 1869-1873.

91.   Erol Uzal, John C. Moulder, Sreeparna Mitra, and James H. Rose, *Impedance of coils over layered metals with continuously variable conductivity and permeability: Theory and experiment.* Journal of Applied Physics, 1993. **74**(3): p. 2076-2089.

92.   Wuliang Yin and A. J. Peyton S. J. Dickinson, *Imaging the continuous conductivity profile within layered metal structures using inductance spectroscopy.* Sensors Journal, IEEE, 2005. **5**(2): p. 161-166.

93.   Y. M. Tan, W. Yin, and A. J. Peyton. *Non-contact measurement of water surface level from phase values of inductive measurements.* in *Instrumentation and Measurement Technology Conference (I2MTC), 2012 IEEE International.* 2012.

94.   Wuliang Yin, R. Binns, S. J. Dickinson, C. Davis, and A. J. Peyton, *Analysis of the liftoff effect of phase spectra for eddy current sensors.* Instrumentation and Measurement, IEEE Transactions on, 2007. **56**(6): p. 2775-2781.

95.   R. J. Haldane, W. Yin, M. Strangwood, A. J. Peyton, and C. L. Davis, *Multi-frequency electromagnetic sensor measurement of ferrite/austenite phase fraction— Experiment and theory.* Scripta Materialia, 2006. **54**(10): p. 1761-1765.

96.   M. Vauhkonen, M. Hamsch, and C. H. Igney, *A measurement system and image reconstruction in magnetic induction tomography.* Physiological Measurement, 2008. **29**(6): p. S445.

97.   D. Gursoy and H. Scharfetter, *Optimum receiver array design for magnetic induction tomography.* Biomedical Engineering, IEEE Transactions on, 2009. **56**(5): p. 1435-1441.

98.   S. Watson, C. H. Igney, O. Dössel, R. J. Williams, and H. Griffiths, *A comparison of sensors for minimizing the primary signal in planar-array magnetic induction tomography.* Physiological Measurement, 2005. **26**(2): p. S319.

99.   H. Scharfetter, M. Robert, and P. Karl, *A new type of gradiometer for the receiving circuit of magnetic induction tomography (MIT).* Physiological Measurement, 2005. **26**(2): p. S307.

100.   R. Merwa J. Rosell-Ferrer, P. Brunner, H. Scharfetter, *A multifrequency magnetic induction tomography system using planar gradiometers: data collection and calibration.* Physiological Measurement, 2006. **27**(5): p. S271.

101.   S. Watson, A. Morris, R. J. Williams, H. Griffiths, and W. Gough, *A primary field compensation scheme for planar array magnetic induction tomography.* Physiological Measurement, 2004. **25**(1): p. 271.

102.   C. H. Riedel, M. Keppelen, S. Nani, R. D. Merges, and O. Dössel, *Planar system for magnetic induction conductivity measurement using a sensor matrix.* Physiological Measurement, 2004. **25**(1): p. 403.

103.   W. Yin and A. J. Peyton, *A planar EMT system for the detection of faults on thin metallic plates.* Measurement Science and Technology, 2006. **17**(8): p. 2130.

104.	R. L. Stoll, *The Analysis of Eddy Current.* Clarendon Press, Oxford, England, 1974.

105.	T. Fawzi, M. Ahmed, and P. E. Burke, *On the use of the impedance boundary conditions in eddy current problems.* IEEE Transactions on Magnetics, 1985. **21**(5): p. 1835-1840.

106.	S. R. H. Hoole, *Experimental validation of the impedance boundary condition and a review of its limitations.* Magnetics, IEEE Transactions on, 1989. **25**(4): p. 3028-3030.

107.	S. R. H. Hoole and C. Carpenter, *Surface impedance models for corners and slots.* Magnetics, IEEE Transactions on, 1985. **21**(5): p. 1841-1843.

108.	S. Yuferev, L. Proekt, and N. Ida, *Surface impedance boundary conditions near corners and edges: rigorous consideration.* Magnetics, IEEE Transactions on, 2001. **37**(5): p. 3465-3468.

109.	E. M. Deeley, *Surface impedance near edges and corners in three-dimensional media.* Magnetics, IEEE Transactions on, 1990. **26**(2): p. 712-714.

110.	J. Sakellaris, G. Meunier, X. Brunotte, C. Guerin, and J. C. Sabonnadiere, *Application of the impedance boundary condition in a finite element environment using the reduced potential formulation.* Magnetics, IEEE Transactions on, 1991. **27**(6): p. 5022-5024.

111.	R. J. Ditchburn and S. K. Burke, *Planar rectangular spiral coils in eddy-current non-destructive inspection.* NDT & E International, 2005. **38**(8): p. 690-700.

112.	N. Ebine and K. Ara, *Magnetic measurement to evaluate material properties of ferromagnetic structural steels with planar coils.* Magnetics, IEEE Transactions on, 1999. **35**(5): p. 3928-3930.

113.	J. Fava and M. Ruch, *Design, construction and characterisation of ECT sensors with rectangular planar coils.* Insight, 2004. **46**(6): p. 268–74.

114.	Javier O. Fava, Liliana Lanzani, and Marta C. Ruch, *Multilayer planar rectangular coils for eddy current testing: Design considerations.* NDT & E International, 2009. **42**(8): p. 713-720.

115.	Z. Z. Yu, P. F. Worthington, S. Stone, and AJ Peyton, *Electromagnetic screening of inductive tomography sensors.* European Concerted Action on Process Tomography Conference, Bergen, Norway, 1995.

116.	D. Goss, R. O. Mackin, E. Crescenzo, H. S. Tapp, and A. J. Peyton, *Understanding the coupling mechanism in high frequency EMT.* Proceedings of the 3rd world congress on industrial process tomography, 2003: p. 364-369.

117.	H. Griffiths, W. Gough, S. Watson, and R. J. Williams, *Residual capacitive coupling and the measurement of permittivity in magnetic induction tomography.* Physiological Measurement, 2007. **28**(7): p. S301.

118.	L. B. Gravelle and P. F. Wilson., *EMI/EMC in printed circuit boards-a literature review.* Electromagnetic Compatibility, IEEE Transactions on, 1992. **34**(2): p. 109-116.

119.	Sreemala Pannala, A. Haridass, and M. Swaminathan, *Parameter extraction and electrical characterization of high density connector using time domain measurements.* Advanced Packaging, IEEE Transactions on, 1999. **22**(1): p. 32-39.

120.	Adnan Naji Jameel and Kawther Khalid Younus, *Buckling Analysis of Damaged Composite Plates Under Uniform Or Non-Uniform Compressive Load.* Journal of Engineering, 2012. **18**(8): p. 961-978.